NONADIABATIC QUANTUM DYNAMICS OF AROMATIC HYDROCARBON RADICALS AND RADICAL CATIONS

A Thesis

Submitted for the Degree of

DOCTOR OF PHILOSOPHY

By

VENNAPUSA SIVARANJANA REDDY

SCHOOL OF CHEMISTRY

PROF. C. R. RAO ROAD

UNIVERSITY OF HYDERABAD

HYDERABAD 500 046

INDIA

April 2010

STATEMENT

I hereby declare that the matter embodied in this thesis is the result of investigations carried out by me in the School of Chemistry, University of Hyderabad, Hyderabad, under the supervision of **Prof. Susanta Mahapatra**.

In keeping with the general practice of reporting scientific observations, due acknowledgment has been made wherever the work described is based on the findings of other investigators.

Hyderabad-46   (**V. Sivaranjana Reddy**)

April 2010

CERTIFICATE

Certified that the work contained in this thesis entitled "Nonadiabatic quantum dynamics of aromatic hydrocarbon radicals and radical cations" has been carried out by Mr. **V. Sivaranjana Reddy** under my supervision and the same has not been submitted elsewhere for a degree.

Hyderabad-46   (**Prof. Susanta Mahapatra**)

April 2010   **Thesis Supervisor**

Dean

School of Chemistry

University of Hyderabad

Hyderabad 500 046

INDIA

ACKNOWLEDGMENTS

I would like to voice my sincere gratitude to **Prof. Susanta Mahapatra** for his excellent guidence and constant encouragement throughout my research work. His determination and hard work are inspirational to my research career.

It was a great and exciting experience to study at School of Chemistry. My sincere thanks to the former and present Deans and all faculty members for their assistance during my Masters and Graduate years.

I am indebted to Prof. Horst Köppel for inviting me to the Theoretical Chemistry Group, University of Heidelberg, Germany, and for fruitful discussions on joint collaborative project.

I am very thankful to Council of Scientific and Industrial Research (CSIR), New Delhi, for the financial support and Centre for Modelling Simulation and Design (CMSD), University of Hyderabad, for computational facilities.

I am greatful to Jawahar Navodaya Vidyalaya (JNV), Lepakshi, Anatapur (Dist) for providing Gifted education. **"JNVL made me what I am today"**.

I am fortunate to have Dr. Padmanaban, Dr. Subhas, Dr. Venkatesan and Dr. Jayachander, Rajesh Kumar, Tanmoy Mondal and Susanta Ghanta as my lab mates. Their invaluable suggestions and discussions on various occasions contributed to the quality of my academic and non-academic life. The technical knowledge, creative ideas and software skills of Rajagopal Rao, Rajagopala Reddy, Susruta, Tanmoy Roy and Nagaprasad Reddy have made my research exciting and fun. Without the co-operation of these people, it would have been impossible to complete this work.

I thank Shirin, Susana, Günter and Obul Reddy who made my stay pleasant in Heidelberg.

Special thanks to Ravi, Sudeena, Suresh, B. Sekhar Reddy, G. V. Ramesh, K. Ramesh Reddy, G. Sekhar Reddy, A. Srinivas Reddy, Jagadeesh Babu, S. Venkat Reddy, Venu Srinivas, Phani Pavan and Vikrant for their help during the most

List of Abbreviations

BO	Born-Oppenheimer
cc-pVDZ	Correlation consistent polarized valence double - ζ
CIs	Conical intersections
CRDS	Cavity ringdown spectroscopy
DIBs	Diffuse interstellar bands
FC	Franck-Condon
FWHM	Full-width at half-maximum
MATI	Mass analysed threshold ionization
MCTDH	Multiconfiguration time-dependent Hartree
MIS	Matrix isolation spectroscopy
MP2	Second order Møller-Plesset perturbation theory
NP	Naphthalene
NP$^+$	Naphthalene radical cation
OVGF	Outer valence Green's function
PA	Phenylacetylene
PA$^+$	Phenylacetylene radical cation
PAHs	Polycyclic aromatic hydrocarbons
PES(s)	Potential energy surface(s)
PIRI	Photoinduced Rydberg ionization
SPFs	Single particle functions
UIR	Unidentified infrared emission
WP	Wave packet

Contents

Chapter 1

Introduction

1.1 Effects of vibronic interactions in the photoinduced dynamics of polyatomic molecules

The interactions between the nuclear and electronic motions are termed as vibronic interactions and their consideration is essential at the degeneracy and near degeneracy of molecular electronic states where the celebrated Born-Oppenheimer approximation of quantum mechanics [1] breaks down. In this approximation, the nuclear motion is confined to a single (scalar) 'adiabatic' electronic potential energy surface (PES). Such treatments of nuclear dynamics enriched our understanding of chemistry at a molecular level for a long time. However, when several electronic states exist energetically close, the nature of the nuclear motion becomes nonadiabatic, i.e. nuclei can move on multiple electronic states simultaneously [2–4].

While the crossings of electronic states of same symmetry is prohibited by the von Neumann and Wigner's non-crossing rule [5] in diatomic molecules, the same restriction does not apply to polyatomic molecules due to the availability of three or more degrees of freedom for the internal atomic motion. In this situation, the electronic states cross and exhibit a double cone type of topography in the

vicinity of the crossing - popularly known in the literature as *conical intersection* (CI) [2–4].

The CIs of electronic PESs can be grouped into few categories with the aid of symmetry rules [6]. Symmetry enforced (or required) electronic degeneracy is exhibited by the Jahn-Teller (JT) active molecules [2]. This degeneracy is split upon distortion along a suitable symmetry reducing nuclear coordinate. The resulting JT split component electronic states form CIs at the equilibrium geometry of the undistorted configuration. For example, the degenerate components of a E' electronic state in D_{3h} split into A_1 and B_2 when distorted to C_{2v}. The latter two electronic states form CIs in the D_{3h} configuration [7]. An analogous situation arises in the linear molecules which is termed as Renner-Teller (RT) effect [8]. In this case, a Π electronic state in the linear $C_{\infty v}$ configuration splits its degeneracy upon bending and transforms to A' and A'' component states in C_s. Symmetry allowed and accidental CIs are ubiquitous molecular systems [9]. In the former the two electronic states required to have distinct spatial symmetries. The $^2A_1$ and $^2B_2$ electronic states of NO_2 form symmetry allowed intersections in the C_{2v} symmetry configuration [10]. CIs of states of same spatial symmetry are very rare. It has been shown by Yarkony and coworkers that the excited electronic states of methyl mercaptan of $^1A''$ symmetry indeed possess such intersections [9].

CIs are considered as bottleneck in the chemistry and physics of excited states of a molecule and are termed as *photochemical funnels* [11–14]. Based on the topography of the intersecting PESs in the vicinity of a crossing, CIs are further classified as peaked and sloped [15–17]. In the latter type of CIs, both the PESs have downhill slope and touch each other at the crossing points in the branching space. The minimum energy point of the upper PES is always lower in energy than crossing point and the crossing appear as a seam of intersections. The sloped CIs are responsible for the unsuccessful chemical reactions and provide the decay channels of photophysical processes such as radiationless deactivation via internal conversion [16, 17]. In case of peaked CIs, both the PESs are ellip-

tical cones pointing against each other with a common tip. In this situation, the crossing point is the lowest energy point on the upper PES and the crossing appears as a double cone. The peaked CIs corresponds to the formation of photoproducts via excited-state reaction pathways. Ring-opening and ring-closure reactions, hydrogen transfer reactions and cis/trans isomerization reactions are the standard photochemical reactions mediated via peaked CIs [16,17]. The photochemical reaction or internal conversion processes occur on subpicosecond time scale competing with the radiative processes which generally occur in nanosecond time scale. The nuclear dynamics in the vicinity of CIs have major implications in chemical physics of molecules in the area of molecular/astrophysical spectroscopy, photochemistry, photobiology and reactive chemical dynamics [9,11–14,18–29].

Some consequences of vibronic interactions in molecular spectroscopy are (i) loss of mirror symmetry of absorption and emission bands, (ii) appearance of forbidden bands in absorption spectrum, (iii) odd quantum excitation of non-totally symmetric vibrational modes, (iv) irregular and complex vibronic structure, (v) broad and diffuse vibronic bands and (vi) low quantum yield or lack of fluorescence emission. As the absorption or photoelectron spectroscopy probes the excited state within the Franck-Condon (FC) region, these features become dominant when the CIs occur near or within the FC zone. These phenomena in a wide variety of molecular systems are successfully explained theoretically within a multi-state and multi-mode vibronic coupling approach [22].

The static and dynamical JT effects in electronic spectroscopy of polyatomic molecules, ranging from triatomics to medium-sized molecules, are treated with the pioneering linear vibronic coupling (LVC) model Hamiltonians and remarkable agreement has been achieved with the experimental observations [22]. The vibrational progressions, spectral intensity and broadening of vibronic bands are studied in grater details. In some cases, the LVC model found to be inadequate and quadratic coupling terms were required to reproduce the spectral features [30–33]. With the availability of better experimental measurements, recent

theoretical studies have shown the necessity of further higher order coupling terms for better comparison with the recorded data [34, 35].

The structure and dynamics at conically intersecting PESs in lower symmetry polyatomic molecules are also investigated [22]. The quantum dynamical calculations including multimodes and multielectronic states are carried out within a time-independent approach to unravel the nonadiabatic effects such as irregular and complex vibronic spectra. The broadening of vibronic bands and nonradiative decay of electronic states are examined within a time-dependent approach by propagating wave packets. The underlying mechanistic details of the ultrafast processes in low-lying electronic states of molecules are established. A molecule excited by UV photon to its excited electronic states can return to its ground electronic state either by a emissive or a non-emissive path. Fluorescence and phosphorescence are the radiative channels depending on the spin multiplicity of the involved electronic states. The other channel is the rapid radiationless relaxation which occurs via internal conversion through conical intersections and is described as photostability of molecule against UV radiation. This mechanism prevents the initiation of hazardous and dangerous photoreactions in biologically important molecules and greatly contributes to the life on the earth [36–40].

The vibronic interactions in degenerate Π electronic states of linear molecules are of special interest. The topography of intersections of states in this molecules is of glancing type. The spectroscopic effects and reaction dynamics of linear triatomic molecules in relativistic and non-relativistic situation are addressed both theoretically and experimentally over the past few decades [8, 41–45].

1.2 A brief overview of photophysics and photochemistry of interstellar molecules

Important astronomical observations such as the enigmatic diffuse interstellar bands (DIBs)and mid-infrared emission features, over galactic and extragalactic regions are attributed to the ramifications of photophysics of polycyclic aromatic hydrocarbons (PAHs) [46–48]. Identification of carriers of DIBs represents a long standing and unresolved issue in the astrophysical spectroscopy. The diffuse structure of these bands is attributed to the very short life times of the excited electronic states of the carrier molecule [49]. It is now well accepted that these bands originate from the ultrafast nonradiative decay of excited electronic states of PAH cations. These cations are most abundant and highly photostable than their neutral and anionic counterparts in the interstellar space. The mid-infrared emissions, also known as unidentified infrared (UIR) bands, are characteristic of IR spectrum of PAH cations.

The absorption/emission features of the family of PAH cations has been explored in the range of near-infrared to UV region in the laboratory as the astronomical observations reveal direct connection to their photophysics. The spectral intensities, broadening and cross sections are the cynosure of the gas-phase spectroscopic investigations in laboratory. The measurements on the intrinsic spectral features poses greater challenges as these molecules possess low vapor pressures and high reactivity. In this regard, novel experimental spectroscopic techniques with high sensitivity and high resolution are developed such as matrix isolation spectroscopy (MIS), cavity ring down spectroscopy (CRDS), resonance-enhanced multiphoton ionization (REMPI) and photodissociation of van der Waals complexes. The electronic spectra of naphthalene radical cation, the smallest molecule in PAH family, was extensively studied with these techniques [54–58]. These experiments revealed diffuse vibronic bands and subpicosecond dynamics of their low-lying electronic states. Very recently, spectroscopic measurements of moder-

ately reddened star Cernis 52 located in the Perseus molecular cloud lead to the discovery of three new DIBs [59]. Aided by the laboratory measurements these are assigned to the electronic transitions in the naphthalene radical cation.

The origin and evolution of PAHs and their role in the molecular universe has profound implications in astrochemistry and astrobiology. Their formation, fragmentation and reactions with the small molecules are studied in greater details both theoretically and experimentally [60–69]. As these processes occur in the presence of UV radiation, the knowledge on the mechanistic details of photoinduced dynamics of excited electronic states enriches the understanding on the existence of complex molecular species such as prebiotic molecules.

Phenyl radical plays a crucial role in the formation of PAHs in astrophysical conditions. The reaction dynamics and kinetics of elementary gas-phase reactions of unsaturated hydrocarbons with the phenyl radical in its ground electronic state are studied with molecular beam experiments [70–72]. The reaction with the acetylene molecule results in the formation of phenylacetylene, which acts as an intermediate in the synthesis of naphthalene [71]. The benzene molecule was discovered from circumstellar medium in 2001 by Cernicharo *et al.* [73] and the presence of phenyl radical and phenylacetylene is more likely expected.

Photodestruction channels such as loss of hydrogen or acetylene from PAHs are studied with theoretical models and are verified by experiments [62–66,75–78]. Phenylacetylene radical cation is one of the isomers formed during the loss of acetylene from the naphthalene radical cation. The photophysics of phenylacetylene radical has been studied in greater detail in connection with DIBs. The experimental investigations have shown that the excited state dynamics is dominated by the ultrafast nonradiative decay through internal conversion process [79–81].

The reactions of ions/molecules with PAHs are of fundamental importance in the interstellar chemistry [67]. The laboratory experiments revealed the formation of aromatic alcohols and ketones by irradiation of UV photons on naphthalene

and H_2O ice mixture under astrophysical conditions [68]. The building blocks of life i.e amino acids are produced by reaction of naphthalene and NH_3+H_2O ice mixture [69]. Naphthaquinones and aminoacids were identified in meteorites [82–86]. The available UV light ejects an electron from naphthalene to give naphthalene radical cation. As this cation is already identified in the universe, it may play key role in the chemical and biological reactions leading to the origin of life.

The interaction of UV radiation with the interstellar aromatic molecules prepares them to the excited electronic states is the first step in their photophysics or photochemistry. The lack of fluorescence emission, broadening of vibronic bands and photostability are indicative of complex vibronic coupling in the electronic excited states of these systems. The knowledge of the fate of low-lying excited electronic states of these species is the major goal in the process of understanding of the molecular universe.

1.3 Outline of the thesis

Chapter 2 deals with the theoretical background of vibronic interactions in polyatomic molecules. Adiabatic and diabatic basis, construction of model diabatic vibronic hamiltonians utilizing elementary symmetry selection rules, electronic structure calculations to extract parameters of Hamiltonian follow. The time-independent and time-dependent approaches for solving quantum eigenvalue equation to calculate vibronic spectra are also discussed.

In Chapter 3, a detailed theoretical account of the photodetachment spectroscopy of phenide anion is presented. The structure and dynamics of ground and two low-lying excited electronic states of phenyl radical are studied with a model diabatic vibronic Hamiltonian. As the ground electronic state is well separated from the rest, the dynamics is treated adiabatically on this state. On the other hand, the two excited states are coupled to each other and the associated

nonadiabatic effects are discussed.

Chapter 4 presents a study on the quantum chemistry and dynamics of four low-lying electronic states of phenylacetylene radical cation. A model diabatic Hamiltonian is constructed from *ab initio* electronic structure calculations. The nonadiabatic dynamics are treated by wave packet propagation method to simulate the complex vibronic spectra. The estimated decay rates of the electronic states are compared with the charge exchange ionization and absorption spectroscopy results. The reduced dimensional calculations are also performed to unravel the resolved vibrational level structures of mass analyzed threshold ionization (MATI) and photoinduced Rydberg ionization (PIRI) spectroscopy and the agreements and discrepancies are also discussed.

A benchmark *ab initio* quantum dynamical study on photoinduced dynamics of six low-lying electronic states of naphthalene radical cation is presented in Chapter 5. The photoelectron spectra and decay rates of electronic states are calculated by developing a model vibronic Hamiltonian consisting of 6 electronic states and 29 vibrational degrees of freedom and solving the eigenvalue equation. The theoretical results are compared with the recent experimental results. The fundamental issues such as broadening of vibronic bands, lack of fluorescence emission and photostability are discussed in detail in connection to the astrophysical observations.

Final conclusions and future directions are presented in Chapter 6.

Chapter 2

Theoretical Methodology

2.1 Vibronic dynamics in polyatomic molecules

2.1.1 The Born-Oppenheimer Adiabatic approximation

The general molecular Hamiltonian in terms of the set of electronic ($\mathbf{q}$) and nuclear ($\mathbf{Q}$) coordinates can be expressed as

$$\mathcal{H}(\mathbf{q},\mathbf{Q}) = T_e(\mathbf{q}) + T_N(\mathbf{Q}) + U(\mathbf{q},\mathbf{Q}), \tag{2.1}$$

where $T_e(\mathbf{q})$ and $T_N(\mathbf{Q})$ are the kinetic energy operators of the electrons and nuclei, respectively. The total potential energy term, $U(\mathbf{q},\mathbf{Q})$, consists the potential energies of electron-electron, electron-nuclear and nuclear-nuclear interactions. The BO adiabatic electronic states are obtained by fixing $T_N(\mathbf{Q}) = 0$ and solving the resulting electronic eigenvalue equation for fixed nuclear configuration [1,87]

$$[T_e(\mathbf{q}) + U(\mathbf{q},\mathbf{Q})]\ \mathbf{\Phi}_n(\mathbf{q};\mathbf{Q}) = \mathbf{V}_n(\mathbf{Q})\ \mathbf{\Phi}_n(\mathbf{q};\mathbf{Q}), \tag{2.2}$$

where $\mathbf{\Phi}_n(\mathbf{q};\mathbf{Q})$ and $\mathbf{V}_n(\mathbf{Q})$ are the BO adiabatic electronic wavefunction parametrically depending on the set of nuclear coordinates $\mathbf{Q}$ and the adiabatic electronic PES, respectively. The full molecular wavefunction $\mathbf{\Psi}(\mathbf{q},\mathbf{Q})$ can now be

expressed in terms of the above adiabatic electronic functions as

$$\mathbf{\Psi}(\mathbf{q}, \mathbf{Q}) = \sum_n \chi_n(\mathbf{Q}) \, \mathbf{\Phi}_n(\mathbf{q}; \mathbf{Q}). \tag{2.3}$$

In the above expression the coefficients $\chi_n(\mathbf{Q})$ contains the nuclear coordinate dependence. Insertion of $\mathbf{\Psi}(\mathbf{q}, \mathbf{Q})$ in Eq. (2.1) gives the following coupled differential equations for the expansion coefficients $\chi_n(\mathbf{Q})$ [87]

$$\{T_N(\mathbf{Q}) + \mathbf{V}_n(\mathbf{Q}) - E\} \, \chi_n(\mathbf{Q}) = \sum_m \mathbf{\Lambda}_{nm}(\mathbf{Q}) \chi_m(\mathbf{Q}), \tag{2.4}$$

where

$$\mathbf{\Lambda}_{nm}(\mathbf{Q}) = - \int d\mathbf{q} \mathbf{\Phi}_n^*(\mathbf{q}; \mathbf{Q}) \left[T_N(\mathbf{Q}), \mathbf{\Phi}_m(\mathbf{q}; \mathbf{Q}) \right], \tag{2.5}$$

defines the coupling of electronic states n and m through the nuclear kinetic energy operator and is termed as the nonadiabatic coupling matrix of the adiabatic electronic representation. The nuclear kinetic energy operator takes non-diagonal form in this representation. The quantity $\mathbf{\Lambda}_{nm}(\mathbf{Q})$ can be expressed as [22,88]

$$\mathbf{\Lambda}_{nm}(\mathbf{Q}) = - \sum_i \frac{\hbar^2}{M_i} A_{nm}^{(i)}(\mathbf{Q}) \frac{\partial}{\partial Q_i} - \sum_i \frac{\hbar^2}{2M_i} B_{nm}^{(i)}(\mathbf{Q}), \tag{2.6}$$

where M_i are nuclear masses and

$$A_{nm}^{(i)}(\mathbf{Q}) = \langle \mathbf{\Phi}_n(\mathbf{q}; \mathbf{Q}) | \nabla_i | \mathbf{\Phi}_m(\mathbf{q}; \mathbf{Q}) \rangle, \tag{2.7}$$

and

$$B_{nm}^{(i)}(\mathbf{Q}) = \langle \mathbf{\Phi}_n(\mathbf{q}; \mathbf{Q}) | \nabla_i^2 | \mathbf{\Phi}_m(\mathbf{q}; \mathbf{Q}) \rangle, \tag{2.8}$$

represents the derivative coupling vector and scalar coupling, respectively.

In the BO approximation $\mathbf{\Lambda}_{nm}(\mathbf{Q})$ is set to zero which holds for widely separated electronic PESs. Using the Hellmann-Feynman theorem $A_{nm}(\mathbf{Q})$ can be

expressed as [22]

$$A_{nm}^{(i)}(\mathbf{Q}) = \frac{\langle \boldsymbol{\Phi}_n(\mathbf{q};\mathbf{Q})|\nabla_i \mathcal{H}_{el}(\mathbf{q};\mathbf{Q})|\boldsymbol{\Phi}_m(\mathbf{q};\mathbf{Q})\rangle}{V_n(\mathbf{Q}) - V_m(\mathbf{Q})}, \qquad (2.9)$$

where $\mathcal{H}_{el}$ represents the electronic Hamiltonian for fixed nuclear configuration. When the two surfaces $V_n(\mathbf{Q})$ and $V_m(\mathbf{Q})$ become degenerate, the derivative coupling elements of Eq. (2.9) exhibit a singularity. This results discontinuity in both the electronic wavefunction and the derivative of energy at the point of degeneracy and making the adiabatic representation unsuitable for the computational study of the nuclear dynamics. The derivative coupling, $A_{nm}(\mathbf{Q})$, becomes extremely large at near-degeneracy or at degeneracy of different electronic PESs eventually breaking down the BO approximation.

2.1.2 Adiabatic to diabatic transformation

The concept of diabatic electronic representation was introduced to overcome the singularity problem of the adiabatic electronic representation [89–91]. By a suitable unitary transformation the diverging kinetic energy couplings of the adiabatic representation transform to smooth potential energy couplings in a diabatic representation. This results into a diagonal form for nuclear kinetic energy operator and the coupling between the electronic states is described by the off-diagonal elements of the potential energy operator. In this representation the coupled equations of motion (as compared to Eq. (2.4)) read [92,93]

$$\{T_N(\mathbf{Q}) + \mathbf{U}_{nn}(\mathbf{Q}) - E\}\chi_n(\mathbf{Q}) = \sum_{m \neq n} \mathbf{U}_{nm}(\mathbf{Q})\chi_m(\mathbf{Q}), \qquad (2.10)$$

where $\mathbf{U}_{nn}(\mathbf{Q})$ are the diabatic PESs and $\mathbf{U}_{nm}(\mathbf{Q})$ are their coupling elements. The latter are give by

$$\mathbf{U}_{nm}(\mathbf{Q}) = \int d\mathbf{q}\, \psi_n^*(\mathbf{q},\mathbf{Q})\left[T_e + \mathbf{V}(\mathbf{q},\mathbf{Q})\right]\psi_m(\mathbf{q},\mathbf{Q}), \qquad (2.11)$$

where ψ represents the diabatic electronic wavefunction obtained from the corresponding adiabatic $\boldsymbol{\Phi}(\mathbf{q};\mathbf{Q})$ ones via a unitary transformation

$$\psi(q;Q) = \mathbf{S}\ \boldsymbol{\Phi}(\mathbf{q};\mathbf{Q}), \tag{2.12}$$

with the aid of a orthogonal transformation matrix

$$\mathbf{S}(\mathbf{Q}) = \begin{pmatrix} \cos\theta(\mathbf{Q}) & \sin\theta(\mathbf{Q}) \\ -\sin\theta(\mathbf{Q}) & \cos\theta(\mathbf{Q}) \end{pmatrix} \tag{2.13}$$

The matrix $\mathbf{S}(\mathbf{Q})$ is called the adiabatic-to-diabatic transformation (ADT) matrix and $\theta(\mathbf{Q})$ defines the transformation angle. The required condition for such transformation is the first-order derivative couplings of Eq. (2.7) vanishes in the new representation for all nuclear coordinates [94, 95] i.e.,

$$\int d\mathbf{q}\psi_n^*(\mathbf{q},\mathbf{Q})\frac{\partial}{\partial Q_i}\psi_m(\mathbf{q},\mathbf{Q}) = 0. \tag{2.14}$$

This requirement yields the following differential equations for the transformation matrix [94, 96, 97]

$$\frac{\partial \mathbf{S}}{\partial Q_i} + \mathbf{A^{(i)}}\mathbf{S} = 0, \tag{2.15}$$

where the elements of the first-order derivative coupling matrix $\mathbf{A^{(i)}}$ are given by Eq. (2.7). A unique solution of the above equation can be obtained only when starting from a finite subspace of electronic states [95]. Therefore, for polyatomic molecular systems rigorous diabatic electronic states do not exist [95]. Approximate schemes are therefore developed to construct diabatic electronic states [97–99].

A brief review on the basic aspects of PES crossings is discussed here by

considering a two-state electronic Hamiltonian in a diabatic representation

$$\mathcal{H}_{el}(\mathbf{Q}) = \begin{pmatrix} H_{11}(\mathbf{Q}) & H_{12}(\mathbf{Q}) \\ H_{21}(\mathbf{Q}) & H_{22}(\mathbf{Q}) \end{pmatrix} \tag{2.16}$$

where H_{11} and H_{22} represent the potential energies of the two diabatic electronic states and, $H_{12} = H_{21}$, describes their coupling potential. We also assume that all the elements of Eq. (2.16) are real. On diagonalization using the ADT matrix $\mathbf{S}$, the electronic Hamiltonian of Eq. 2.16 yields the adiabatic potential energies

$$V_{1,2}(\mathbf{Q}) = \Sigma \pm \sqrt{\Delta^2 + H_{12}^2} \;\;, \tag{2.17}$$

where $\Sigma = (H_{11} + H_{22})/2$ and $\Delta = (H_{11} - H_{22})/2$. The transformation angle $\theta(\mathbf{Q})$ of the ADT matrix depends on the set of nuclear coordinates and can be obtained from

$$\theta(\mathbf{R}) = \frac{1}{2} \arctan\left[2H_{12}(\mathbf{Q})/(H_{22}(\mathbf{Q}) - H_{11}(\mathbf{Q}))\right]. \tag{2.18}$$

It can be seen from Eq. (2.17) that the two adiabatic surfaces, $V_1(\mathbf{Q})$ and $V_2(\mathbf{Q})$ exhibit a degeneracy when, $\Delta = 0$ and $H_{12} = 0$. The latter quantities depend on two independent set of nuclear coordinates, not available for a diatomic molecule leading to the non crossing rule [5] unless H_{12} vanishes on symmetry ground. On the other hand, due to the availability of more than one nuclear degrees of freedom, the PESs of polyatomic molecules generally cross. It can be seen that $V_{1,2}(\mathbf{Q})$ resembles the equation of a double cone intersecting at their vertex. This topography of intersecting PESs is popularly known as *conical intersections* (CIs) [2–4, 11–14, 18–25]. By expanding H_{11}, H_{22} and H_{12} in a first-order Taylor series, the quantities Δ and H_{12} can be equated to a gradient difference and nonadiabatic coupling vectors, respectively [15]. The space spanned by these vectors defines the two-dimensional branching space in which the degeneracy of

the two surfaces is lifted except at the origin. Whereas, the surfaces remain degenerate in the remaining $N-2$ dimensional space (when spin is not included, N is the number of nuclear degrees of freedom). The locus of the degeneracy of the two surfaces defines the seam of the CIs. The estimation of energetic minimum of adiabatic PESs and minimum of seam of CIs of PESs of a multidimensional system are discussed in detail in Appendix A.

2.1.3   The model diabatic vibronic Hamiltonian

The vibronic coupling in the radical and radical cations of aromatic hydrocarbons is studied by photoionizing the corresponding anion and neutral molecules, respectively. The vibronic Hamiltonian of the final states of the ionized species is constructed in terms of the dimensionless normal coordinates of the electronic ground state of the corresponding (reference) anion or neutral species. The mass-weighted normal coordinates (q_i) are obtained by diagonalizing the force field and are converted into the dimensionless form by

$$Q_i = (\omega_i/\hbar)^{\frac{1}{2}} q_i, \tag{2.19}$$

where ω_i is the harmonic frequency of the ith vibrational mode. These actually describes the normal displacement coordinates from the equilibrium configuration, $\mathbf{Q} = 0$, of the reference state. The vibronic Hamiltonian describing the photoinduced molecular process is then given by [22]

$$\mathcal{H} = (\mathcal{T}_{\mathcal{N}} + \mathcal{V}_0)\mathbf{1}_n + \Delta\mathcal{H}. \tag{2.20}$$

In the above equation $(\mathcal{T}_{\mathcal{N}} + \mathcal{V}_0)$ defines the Hamiltonian for the unperturbed reference ground electronic state, with

$$\mathcal{T}_{\mathcal{N}} = -\frac{1}{2}\sum_i \omega_i \left[\frac{\partial^2}{\partial Q_i^2}\right], \tag{2.21}$$

and

$$\mathcal{V}_0 = \frac{1}{2} \sum_i \omega_i Q_i^2, \tag{2.22}$$

describing the kinetic and potential energy operators, respectively. All vibrational motions in this reference electronic state are generally, to a good approximation, assumed to be harmonic. The quantity $\mathbf{1}_n$ is a $(n \times n)$ (where n is the number of final electronic states) unit matrix and $\Delta\mathcal{H}$ in Eq. (2.20) describes the change in the electronic energy upon ionization. This is a $(n \times n)$ non-diagonal matrix. A diabatic electronic basis is utilized in order to construct the above Hamiltonian. This is to circumvent the stated shortcomings of the adiabatic electronic basis in the numerical application. The diagonal elements of the electronic Hamiltonian, $\Delta\mathcal{H}$, describe the diabatic potential energy surfaces of the electronic states and the off-diagonal elements describe their coupling surfaces and are expressed in terms of normal coordinates as [22]

$$W_{nn}(\mathbf{Q}) = W_0(\mathbf{Q}) + E_n + \Sigma_i \kappa_i^{(n)} Q_i + \Sigma_{ij} \gamma_{ij}^{(n)} Q_i Q_j + ... \tag{2.23}$$

and

$$W_{nn'}(\mathbf{Q}) = W_{nn'}(0) + \Sigma_i \lambda_i^{(nn')} Q_i + ..., \tag{2.24}$$

respectively. The intrastate (κ and γ) and the interstate (λ) coupling parameters are given by

$$\kappa_i^{(n)} = (\partial W_{nn}/\partial Q_i)_0 \tag{2.25}$$

$$\lambda_i^{(nn')} = (\partial W_{nn'}/\partial Q_i)_0 \tag{2.26}$$

$$\gamma_{ij}^{(n)} = \frac{1}{2}[(\partial^2 W_{nn}/\partial Q_i Q_j)_0] \tag{2.27}$$

Here E_n denotes the vertical ionization energy of the nth excited electronic state from the reference state. Possible coupling between the states is assessed by employing the symmetry selection rule

$$\Gamma_m \times \Gamma_{Q_i} \times \Gamma_n \supset \Gamma_A, \qquad (2.28)$$

where Γ_m, Γ_n and Γ_{Q_i} refer to the irreducible representations (IREPs) of the electronic states m, n and the ith vibrational mode, respectively. Γ_A denotes the totally symmetric representation. According to this prescription, the totally symmetric vibrational modes are always active within a given electronic state. A truncation of the Taylor series in Equations 2.23 and 2.24 at the first-order term leads to the pioneering linear vibronic coupling (LVC) model [22].

2.1.4   Electronic structure calculations

The coupling parameters of the vibronic Hamiltonian are determined by calculating the adiabatic potential energies as a function of the dimensionless normal coordinates by a suitable *ab initio* method. For the reference molecule, the equilibrium geometry and the harmonic force field of the ground electronic state are routinely calculated by electronic structure methods in which the analytic gradients of energy are available. The geometry optimization and the calculation of harmonic vibrational frequencies of the reference molecule in its electronic ground state are carried out at the Møller-Plesset perturbation theory (MP2) level employing the correlation-consistent polarized valence double - ζ (cc-pVDZ) Gaussian basis set of Dunning [100]. Using the Gaussian-03 program package [101], the electronic structure calculations were performed. For molecules which possess a closed-shell ground electronic state, the outer valence Green's function (OVGF) method has been found to be very successful in estimating the energies of their ionized states [102,103]. In this method the vertical ionization energies (VIEs) are calculated along the normal coordinates of a given vibrational mode. These VIEs

plus the harmonic potential of the reference state are equated with the adiabatic potential energies ($\mathbf{V}$) of the final electronic state. The latter are then fitted to the adiabatic form of the diabatic electronic Hamiltonian of Eq. (2.20)

$$\mathbf{S}^{\dagger}(\mathcal{H} - T_N 1_n)\mathbf{S} \;=\; \mathbf{V} \tag{2.29}$$

2.2 Simulation of Eigenvalue spectrum

The excitation strength in the spectral transition to the coupled electronic states is described by the Fermi's golden rule and is given by

$$P(E) \;=\; \sum_v \left| \langle \Psi_v^f | \hat{T} | \Psi_0^i \rangle \right|^2 \delta(E - E_v^f + E_0^i), \tag{2.30}$$

where $|\Psi_0^i\rangle$ is the initial vibronic ground state (reference state) with energy E_0^i and $|\Psi_v^f\rangle$ corresponds to the (final) vibronic state of the photoionized molecule with energy E_v^f. The reference ground electronic state is approximated to be vibronically decoupled from the other states and it is given by

$$|\Psi_0^i\rangle \;=\; |\Phi_0^0\rangle|\mathbf{0}\rangle, \tag{2.31}$$

where $|\Phi_0^0\rangle$ and $|\mathbf{0}\rangle$ represent the diabatic electronic and vibrational part of the wavefunction, respectively. The quantity $\hat{T}$ represents the transition dipole operator that describes the interaction of the electron with the external radiation of energy E during the photoionization process.

2.2.1 Time-Independent Approach

The time-independent vibronic Schrödinger equation

$$\mathcal{H}|\Psi_n^f\rangle = E_n|\Psi_n^f\rangle, \tag{2.32}$$

is solved by expanding the vibronic eigenstates $\{|\Psi_n^f\rangle\}$ in the direct product harmonic oscillator basis of the electronic ground state [22]

$$|\Psi_n^f\rangle = \sum_{\{|K_i\rangle\},m} a_{K_1,...,K_l}^m |K_1\rangle...|K_l\rangle|\phi_m\rangle. \tag{2.33}$$

Here K^{th} level of ith vibrational mode is denoted by $|K_i\rangle$ and $|\phi_m\rangle$ denotes the mth electronic state of the photoionized molecule. For each vibrational mode, the oscillator basis is suitably truncated in the numerical calculations. In practice, the maximum level of excitation for each mode is estimated from the convergence behavior of the spectral envelope. The Hamiltonian matrix expressed in a direct product Harmonic oscillator basis is highly sparse and is tri-diagonalized by the Lanczos algorithm [104]. The diagonal elements of the resulting eigenvalue matrix give the position of the vibronic lines and the relative intensities are obtained from the squared first components of the Lanczos eigenvectors [22, 93]. These calculations are simplified by employing the generalized Condon approximation in a diabatic electronic basis [105], that is, the matrix elements of $\hat{T}$ in the diabatic electronic basis are treated to be independent of nuclear coordinates and have the equal modulus.

To reflect the inherent broadening of the experimental vibronic spectrum, the stick vibronic lines obtained from the matrix diagonalization calculations are usually convoluted [22] with a Lorentzian line shape function

$$L(E) = \frac{1}{\pi} \frac{\frac{\Gamma}{2}}{E^2 + (\frac{\Gamma}{2})^2}, \tag{2.34}$$

with a full width at the half maximum (FWHM) Γ.

2.2.2 Time-Dependent Approach

Use of Fourier representation of the Dirac delta function, $\delta(x) = \frac{1}{2\pi} \int_{-\infty}^{+\infty} e^{ixt/\hbar}$, in the golden rule equation transforms Eq. (2.30) into the following useful form, readily utilized in a time-dependent picture

$$P(E) \approx 2Re \int_0^\infty e^{iEt/\hbar} \langle \Psi_f(0)|\boldsymbol{\tau}^\dagger e^{-i\mathcal{H}t/\hbar} \boldsymbol{\tau}|\Psi_f(0)\rangle dt, \tag{2.35}$$

$$\approx 2Re \int_0^\infty e^{iEt/\hbar} C_f(t) \, dt. \tag{2.36}$$

In Eq. (2.35) the elements of the transition dipole matrix $\boldsymbol{\tau}^\dagger$ is given by, $\boldsymbol{\tau}^f = \langle \Phi^f|\hat{T}|\Phi^i\rangle$. These elements are slowly varying function of nuclear coordinates and generally treated as constants in accordance with the applicability of the Condon approximation in a diabatic electronic basis [22, 105]. The quantity $C_f(t) = \langle \Psi_f(0)|\Psi_f(t)\rangle$, is the time autocorrelation function of the wave packet (WP) initially prepared on the fth electronic state and, $\Psi_f(t) = e^{-i\mathcal{H}t/\hbar} \Psi_f(0)$.

In the time-dependent calculations, the time autocorrelation function is damped with a suitable time-dependent function before Fourier transformation. The usual choice has been a function of type

$$f(t) = exp[-t/\tau_r] \, , \tag{2.37}$$

where τ_r represents the relaxation time. Multiplying $C(t)$ with $f(t)$ and then Fourier transforming it is equivalent to convoluting the spectrum with a Lorentzian line shape function (cf., Eq. (2.34)) of FWHM, $\Gamma = 2/\tau_r$.

2.2.3 Propagation of wave packet by MCTDH algorithm

The matrix diagonalization approach becomes computationally impracticable with increase in the electronic and nuclear degrees of freedom. Therefore, for large molecules and with complex vibronic coupling mechanism this method often becomes unreliable. The WP propagation approach within the multi-configuration time-dependent Hartree (MCTDH) scheme has emerged as a very promising alternative tool for such situation [107–109]. This is a grid based method which utilizes discrete variable representation (DVR) combined with fast Fourier transformation and powerful integration schemes. The efficient multiset ansatz of this scheme allows for an effective combination of vibrational degrees of freedom and thereby reduces the dimensionality problem. In this ansatz the wavefunction for a nonadiabatic system is expressed as [106–108]

$$
\begin{aligned}
\Psi(Q_1, ..., Q_f, t) &= \Psi(R_1, ..., R_p, t) &&(2.38) \\
&= \sum_{\alpha=1}^{\sigma} \sum_{j_1=1}^{n_1^{(\alpha)}} ... \sum_{j_p=1}^{n_p^{(\alpha)}} A_{j_1,...,j_p}^{(\alpha)}(t) \prod_{k=1}^{p} \varphi_{jk}^{(\alpha,k)}(R_k, t)|\alpha\rangle, &&(2.39)
\end{aligned}
$$

Where, $R_1,..., R_p$ are the coordinates of p particles formed by combining vibrational degrees of freedom, α is the electronic state index and $\varphi_{jk}^{(\alpha,k)}$ are the n_k single-particle functions (SPFs) for each degree of freedom k associated with the electronic state α. Employing a variational principle, the solution of the time-dependent Schrödinger equation is described by the time-evolution of the expansion coefficients $A_{j_1,...,j_p}^{(\alpha)}$. In this scheme all multi-dimensional quantities are expressed in terms of one-dimensional ones employing the idea of mean-field or Hartree approach. This provides the efficiency of the method by keeping the size of the basis optimally small. Furthermore, multi-dimensional single-particle functions are designed by appropriately choosing the set of system coordinates so as to reduce the number of particles and hence the computational overheads. The

operational principles, successes and shortcomings of this schemes are detailed in the literature [106–108]. The Heidelberg MCTDH package [109] is employed to propagate WPs in the numerical simulations for present molecules. The spectral intensity is finally calculated using Eq. (2.35) from the time-evolved WP.

Here we provide a brief overview on the computer hardware requirement for the MCTDH method. The memory required by standard propagation method is proportional to N^f, where N is the total number of grid points or primitive basis functions and f is the total number of degrees of freedom. In contrast, memory needed by the MCTDH method scales as

$$memory \quad \sim \quad fnN + n^f \qquad (2.40)$$

where, n represent the number of SPFs. The memory requirements can however be reduced if SPFs are used that describe a set of degrees of freedom, termed as *multimode* SPFs. By combining d degrees of freedom together to form a set of $p=f/d$ particles, the memory requirement changes to

$$memory \quad \sim \quad f\tilde{n}N^d + \tilde{n}^f \qquad (2.41)$$

where $\tilde{n}$ is the number of multimode functions needed for the new particles. If only single-mode functions are used i.e. $d=1$, the memory requirement, Eq. 2.41, is dominated by n^f. By combining degrees of freedom together this number can be reduced, but at the expense of longer product grids required to describe the multimode SPFs.

Chapter 3

Vibronic interactions in the photodetachment spectroscopy of phenide anion

3.1 Introduction

This chapter deals with the detailed analysis of vibronic level structures of ground and two low-lying excited electronic states of phenyl radical ($C_6H_5^\bullet$). Phenide anion, the conjugate base of $C_6H_5^\bullet$, belong to C_{2v} symmetry point group at its equilibrium configuration in its ground electronic state ($\widetilde{X}^1A_1$) with the following molecular orbital sequence,

$$(1a_1)^2(2a_1)^2(1b_2)^2(3a_1)^2(2b_2)^2.....(1b_1)^2(7b_2)^2(1a_2)^2(2b_1)^2(11a_1)^2.$$

The SCF canonical molecular orbitals (MOs); the highest occupied molecular orbital HOMO; $11a_1$, HOMO-1; $2b_1$ and HOMO-2; $1a_2$ are shown in Fig. 3.1. The HOMO is of nonbonding type of orbital and the other two orbitals are of π-type. Photodetachment of an electron from $11a_1, 2b_1$ and $1a_2$ molecular orbitals of phenide anion yields phenyl radical in its ground $\widetilde{X}^2A_1$, and excited

HOMO (a_1)   HOMO -1 (b_1)   HOMO - 2 (a_2)
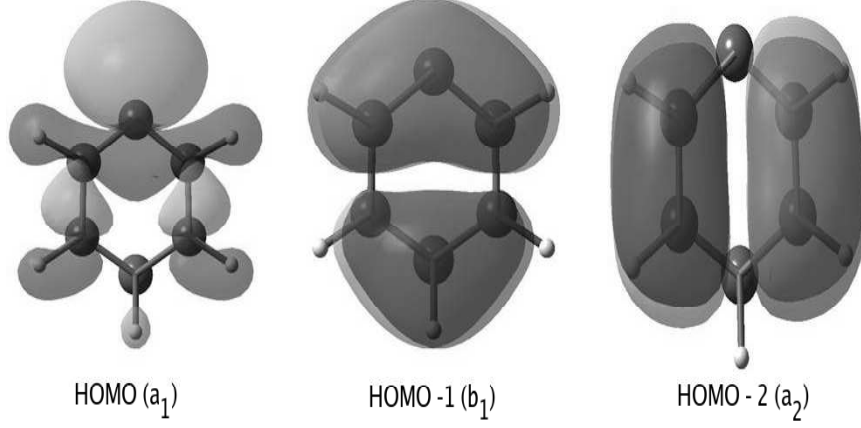
Figure 3.1: The canonical molecular orbitals of the phenide anion.

$\widetilde{A}^2B_1$ and $\widetilde{B}^2A_2$ electronic states, respectively. The detachment energies of $\sim$ 1.007 eV, 2.862 eV and 3.433 eV are obtained for these electronic states, respectively. The 27 vibrational degrees of freedom of the phenide anion (shown in Table 3.1) belongs to the following irreducible representations of the C_{2v} symmetry point group

$$\Gamma_{vib} = 10a_1 + 3a_2 + 5b_1 + 9b_2$$

According to the symmetry selection rules described in Chapter 2, the totally symmetric vibrational modes are always active within each electronic state [22] and the interstate couplings (in first-order) between the $\widetilde{X}$, $\widetilde{A}$ and $\widetilde{B}$ electronic states are given by

$$^2A_1 \otimes \Gamma_Q \otimes {}^2B_1 \supset A_1 \; ; \quad \Gamma_Q \in b_1$$
$$^2A_1 \otimes \Gamma_Q \otimes {}^2A_2 \supset A_1 \; ; \quad \Gamma_Q \in a_2$$
$$^2B_1 \otimes \Gamma_Q \otimes {}^2A_2 \supset A_1 \; ; \quad \Gamma_Q \in b_2$$

Therefore, only non-totally symmetric vibrational modes give rise to non-zero

Table 3.1: Symmetry, frequency and description of the 27 vibrational modes of the phenide anion in its electronic ground state.

Symmetry	Mode	Vibrational Frequency (ω_i)/eV MP2/cc-pVDZ	Description
a_1	ν_1	0.0727	Ring deformation
	ν_2	0.1196	Ring deformation
	ν_3	0.1248	Ring deformation
	ν_4	0.1316	C-H in-plane rocking
	ν_5	0.1479	C-H in-plane scissoring
	ν_6	0.1802	C=C Stretching
	ν_7	0.1965	C=C Stretching
	ν_8	0.3772	C-H Symmetrical stretching
	ν_9	0.3861	C-H Symmetrical stretching
	ν_{10}	0.3931	C-C Symmetrical stretching
b_1	ν_{11}	0.0487	C=C Out-of-plane bending
	ν_{12}	0.0832	C-H Out-of-plane wagging
	ν_{13}	0.0851	C-H Out-of-plane wagging
	ν_{14}	0.1063	C-H Out-of-plane twisting
	ν_{15}	0.1160	C-H Out-of-plane twisting
b_2	ν_{16}	0.0769	Ring deformation
	ν_{17}	0.1288	C-H In-plane rocking
	ν_{18}	0.1414	C-H In-plane scissoring
	ν_{19}	0.1606	C-H In-plane rocking
	ν_{20}	0.1705	C-H In-plane rocking
	ν_{21}	0.1791	C=C Stretching
	ν_{22}	0.1976	C-H Bending
	ν_{23}	0.3771	C-H Asymmetric stretching
	ν_{24}	0.3869	C-H Asymmetric stretching
a_2	ν_{25}	0.0433	C=C Out-of-plane bending
	ν_{26}	0.1041	C-H Out-of-plane twisting
	ν_{27}	0.1173	C-H Out-of-plane twisting

interstate coupling. There are five b_1 and three a_2 vibrational modes which can cause coupling of the ground $\widetilde{X}^2A_1$ with the excited $\widetilde{A}^2B_1$ and $\widetilde{B}^2A_2$ states, respectively.

The photodetachment spectrum of the phenide anion has been recorded by Gunion *et al.* using 351 nm photon energy and it revealed well resolved vibronic structure of the $\widetilde{X}^2A_1$ electronic ground state of phenyl radical and a broad (unresolved) and diffuse hump at high energies [110]. The observed progressions in the $\widetilde{X}^2A_1$ photoelectron band are attributed to the two totally symmetric vibrational modes at $\sim 600 \ cm^{-1}$ and $\sim 968 \ cm^{-1}$. The weak and diffuse signal at high energies is attributed to an excited $\widetilde{A}$ electronic state of the phenyl radical. Despite a very high resolution, the $\widetilde{X}^2A_1$ band appears to be very complex and a satisfying interpretation of the observed vibrational structures of this band is still missing. This band revealed anomalous intensity distributions and the progression due to the high frequency vibrational mode at $\sim 968 \ cm^{-1}$ still remains ambiguous as there are three vibrational modes of approximately the same frequency in phenide anion.

The electronic absorption spectra of phenyl radical have been recorded by different experimental groups in the gas phase and in matrices and also in aqueous solution [111–118]. In particular, the electron absorption spectrum recorded by Radziszewski revealed well resolved vibronic structures of the $\widetilde{A}^2B_1$ and higher electronic states ($^2A_1$ and $^2B_1$) [117]. While the vibronic structure of the $\widetilde{A}^2B_1$ electronic state is obtained from the electronic absorption measurements, the optically dark $\widetilde{B}^2A_2$ electronic state has no clear signature in the literature. The electronic excitation energies for the low-lying excited electronic states of phenyl radical have also been theoretically calculated by different groups [119–122]. Most recently, Kim *et al* [122] have performed *ab initio* calculations at the CASSCF/MRCI level of theory for seven excited electronic states of the phenyl radical in an attempt to assign the electronic absorption spectrum recorded by Radziszewski [117]. Their analysis revealed the $^2B_1$ and $^2A_2$ electronic states as

the first and second excited electronic states of the phenyl radical, respectively. While the experimental $^2B_1$ vibronic spectrum revealed a long vibrational progression, the theoretical calculations of Kim *et al* [122] did not reproduce the rich vibronic structure observed in the experiment [117]. The latter authors [122] however, have pointed out that consideration of $^2B_1$ - $^2A_2$ vibronic coupling may be important to overcome the observed disagreement between theory and experiment.

In this chapter we set out to resolve the ambiguity in the assignment of the vibronic structure of the $\widetilde{X}^2A_1$ electronic state of the phenyl radical and also attempt to develop a model to describe the $\widetilde{A}^2B_1$ - $\widetilde{B}^2A_2$ vibronic coupling and discuss its possible impact on the vibronic structure of the mentioned experimental bands.

3.2 The Vibronic Hamiltonian

As mentioned before, the $\widetilde{X}$ state of $C_6H_5^\bullet$ is well separated from $\widetilde{A}$ and $\widetilde{B}$ states. However, the $\widetilde{A}$ and $\widetilde{B}$ states are energetically close and the coupling between them is important to consider in order to elucidate the vibronic structure of these electronic states. Therefore, the nuclear motion in the $\widetilde{X}$ state treated adiabatically and the nonadiabatic interactions are considered in the coupled $\widetilde{A}$ and $\widetilde{B}$ electronic states.

The vibronic Hamiltonian in terms of the dimensionless normal coordinates Q_i of the vibrational mode ν_i of the electronic ground state of phenide anion in a diabatic electronic basis [89–91] can be written as

$$\mathcal{H} = (\mathcal{T}_N + \mathcal{V}_0)\mathbf{1} + \begin{pmatrix} u_{11} & 0 & 0 \\ 0 & u_{22} & u_{23} \\ 0 & u_{23}^\star & u_{33} \end{pmatrix}, \tag{3.1a}$$

Where

$$\mathcal{T}_N \;=\; -\frac{1}{2}\sum_{i=1}^{27}\omega_i\left(\frac{\partial^2}{\partial Q_i^2}\right), \tag{3.1b}$$

is the nuclear kinetic energy operator and

$$\mathcal{V}_0 \;=\; \frac{1}{2}\sum_{i=1}^{27}\omega_i Q_i^2, \tag{3.1c}$$

is the harmonic ground state potential of the phenide anion. **1** represents a 3×3 unit matrix. The 27 nondegenerate vibrational modes (cf., Table 3.1) are designated by the index i, and are defined in the following way: $i = 1-10$ ($\nu_1 - \nu_{10}$) belong to the a_1 representation, $i = 11-15$ (ν_{11}-ν_{15}) belong to the b_1 representation, $i = 16-24$ (ν_{16} -ν_{24}) belong to the b_2 representation and $i = 25-27$ (ν_{25}-ν_{27}) belong to the a_2 representation. The quantity ω_i represents the harmonic frequency of these vibrational modes. The elements of the electronic Hamiltonian (the second matrix in Eq.(3.1a)) represent the potential energies of the neutral electronic states (u_{11},u_{22} and u_{33}) and their coupling potentials (u_{23}). These elements are expanded in a Taylor series around the reference equilibrium geometry of the electronic ground state of the phenide anion (occurring at $\mathbf{Q}=0$) as follows [22]

$$u_{11} \;=\; E_0^{(X)} + \sum_{i=1}^{10}\kappa_i^{(X)}Q_i + \frac{1}{2}\sum_{i=1}^{27}\gamma_i^{(X)}Q_i^2 + \frac{1}{2}\sum_{i=1}^{10}\sum_{i\neq j,j=1}^{10}\gamma_{ij}^{(X)}Q_iQ_j, \tag{3.1d}$$

$$u_{22} \;=\; E_0^{(A)} + \sum_{i=1}^{10}\kappa_i^{(A)}Q_i + \frac{1}{2}\sum_{i=1}^{27}\gamma_i^{(A)}Q_i^2 + \frac{1}{2}\sum_{i=1}^{10}\sum_{i\neq j,j=1}^{10}\gamma_{ij}^{(A)}Q_iQ_j \tag{3.1e}$$

$$u_{33} = E_0^{(B)} + \sum_{i=1}^{10} \kappa_i^{(B)} Q_i + \frac{1}{2} \sum_{i=1}^{27} \gamma_i^{(B)} Q_i^2 + \frac{1}{2} \sum_{i=1}^{10} \sum_{i \neq j, j=1}^{10} \gamma_{ij}^{(B)} Q_i Q_j \quad (3.1f)$$

$$u_{23} = u_{23}^{\star} = \sum_{i=16}^{24} \lambda_i^{(A,B)} Q_i. \quad (3.1g)$$

In the above equations the quantity $E_0^{(k)}$ ($k \in \widetilde{X}/\widetilde{A}/\widetilde{B}$) represents the vertical ionization energy of the kth electronic state. $\kappa_i^{(k)}$, $\gamma_i^{(k)}$ and $\gamma_{ij}^{(k)}$ are the linear, second-order and intermode bilinear coupling parameters of the ith vibrational mode (bilinear between vibrational modes i and j) in the kth electronic state. The quantity $\lambda_i^{(A,B)}$ is the linear vibronic coupling parameter between the $\widetilde{A}^2 B_1$ and $\widetilde{B}^2 A_2$ electronic states of $C_6H_5^{\bullet}$. All these coupling parameters are derived by performing extensive *ab initio* calculations as mentioned in Chapter 2.

In Fig. 3.2, the non-linear least square fittings of adiabatic potential energies of the $\widetilde{X}^2 A_1$ state of $C_6H_5^{\bullet}$ measured relative to the $\widetilde{X}^1 A_1$ electronic state of phenide along 10 totally symmetric vibrational modes (a_1) are shown. The complete set of coupling parameters derived for the $\widetilde{X}$, $\widetilde{A}$ and $\widetilde{B}$ electronic states of the phenyl radical are given in Tables 3.2-3.3.
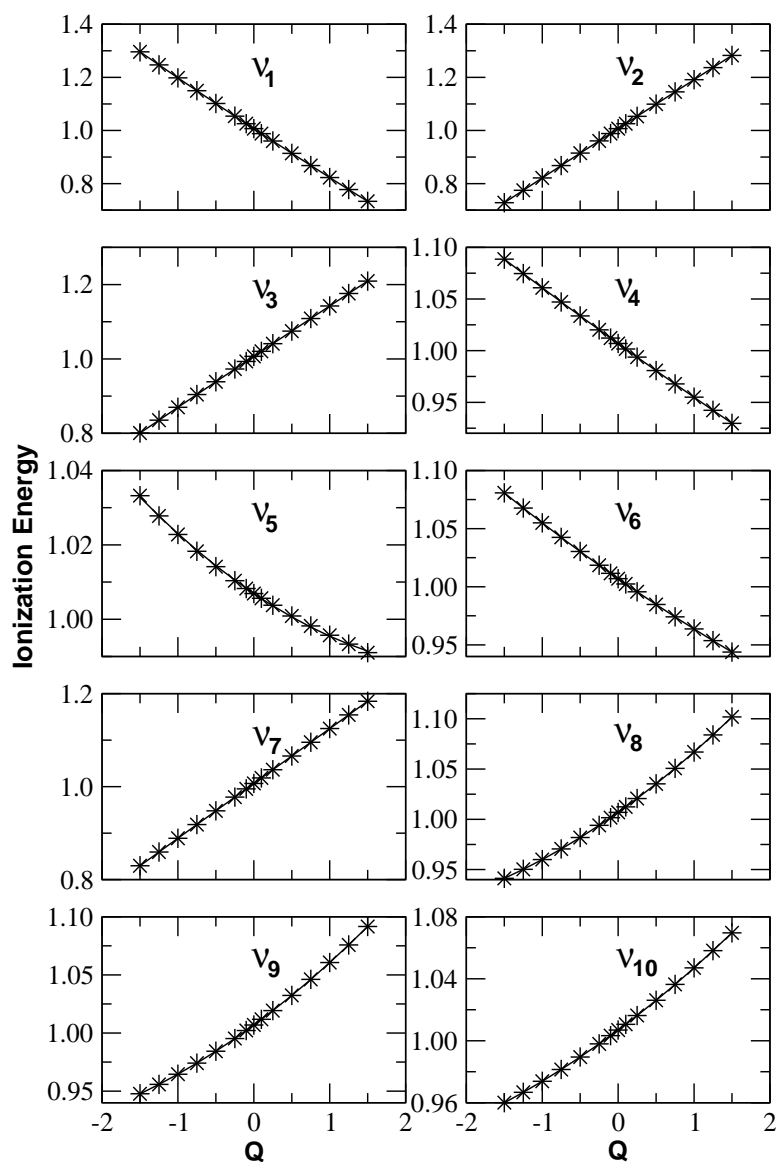
Figure 3.2: Adiabatic potential energies of the $\widetilde{X}^2 A_1$ electronic states of $C_6H_5^\bullet$ measured relative to the electronic ground state of phenide anion along the dimensionless normal coordinates of the totally symmetric vibrational modes (ν_1-ν_{10}). The asterisks represent the computed data for the $\widetilde{X}^2 A_1$ electronic state and a quadratic fit to these data is shown by the solid line in each panel. The linear (κ_j) and diagonal quadratic coupling (γ_j) parameters listed in Table 3.2 are obtained from the above fits.

Table 3.2: Coupling parameters for the $\widetilde{X}^2A_1$, $\widetilde{A}^2B_1$ and $\widetilde{B}^2A_2$ electronic states of the phenyl radical derived from the OVGF data. The dimensionless coupling strengths, $\kappa^2/2\omega^2$, $\kappa'^2/2\omega^2$ and $\kappa''^2/2\omega^2$ are shown in parentheses. All quantities are given in eV.

modes (symmetry)	κ $\widetilde{X}^2A_1$	γ $\widetilde{X}^2A_1$	κ' $\widetilde{A}^2B_1$	γ' $\widetilde{A}^2B_1$	κ'' $\widetilde{B}^2A_2$	γ'' $\widetilde{B}^2A_2$
$\nu_1(a_1)$	-0.1876 (3.327)	0.0069	-0.0814 (0.627)	-0.0036	0.0690 (0.4502)	-0.0060
$\nu_2(a_1)$	0.1848 (1.194)	-0.0014	-0.0727 (0.185)	0.0027	-0.0507 (0.0898)	0.0011
$\nu_3(a_1)$	0.1362 (0.595)	-0.0017	0.0277 (0.025)	0.0006	0.0437 (0.0613)	-0.0001
$\nu_4(a_1)$	-0.0529 (0.081)	0.0019	0.0115 (0.004)	0.0036	-0.0147 (0.0062)	0.0001
$\nu_5(a_1)$	-0.0138 (0.004)	0.0046	0.0822 (0.154)	0.0011	-0.0835 (0.1594)	0.0950
$\nu_6(a_1)$	-0.0457 (0.032)	0.0048	0.1001 (0.154)	0.0071	-0.0564 (0.0489)	0.0052
$\nu_7(a_1)$	0.1180 (0.180)	0.0001	-0.1277 (0.211)	-0.0028	0.1603 (0.3327)	0.0112
$\nu_8(a_1)$	0.0535 (0.010)	0.0130	0.0424 (0.006)	0.0120	0.3840 (0.5181)	0.0113
$\nu_9(a_1)$	0.0480 (0.007)	0.0152	0.0409 (0.006)	0.0094	0.0292 (0.0028)	0.0940
$\nu_{10}(a_1)$	0.0366 (0.004)	0.0071	0.0339 (0.004)	0.0071	0.0409 (0.0054)	0.0065
$\nu_{11}(b_1)$	-	0.1561	-	-0.1688	-	-0.0152
$\nu_{12}(b_1)$	-	0.1345	-	-0.1595	-	-0.0250
$\nu_{13}(b_1)$	-	0.0624	-	-0.0549	-	0.0072
$\nu_{14}(b_1)$	-	0.0519	-	0.0016	-	0.0123
$\nu_{15}(b_1)$	-	0.0457	-	-0.0198	-	-0.0305
$\nu_{16}(b_2)$	-	-0.0071	-	-0.0214	-	0.0153
$\nu_{17}(b_2)$	-	0.0088	-	0.0007	-	0.0020
$\nu_{18}(b_2)$	-	0.0086	-	0.0003	-	0.0226
$\nu_{19}(b_2)$	-	-0.0044	-	0.0124	-	0.0157
$\nu_{20}(b_2)$	-	-0.0041	-	0.0266	-	0.0189
$\nu_{21}(b_2)$	-	-0.0086	-	-0.0066	-	0.0484
$\nu_{22}(b_2)$	-	-0.0046	-	-0.0612	-	0.0748
$\nu_{23}(b_2)$	-	0.0136	-	0.0125	-	0.0116
$\nu_{24}(b_2)$	-	0.0106	-	0.0086	-	0.0088
$\nu_{25}(a_2)$	-	0.0218	-	-0.0110	-	-0.0524
$\nu_{26}(a_2)$	-	0.0176	-	0.0044	-	0.0220
$\nu_{27}(a_2)$	-	0.0188	-	0.0018	-	0.0074

3.3 Results and Discussion

3.3.1 Adiabatic potential energy surfaces and conical intersections

The adiabatic potential energy surfaces of the $\widetilde{X}$, $\widetilde{A}$ and $\widetilde{B}$ electronic states of the phenyl radical are obtained by diagonalizing the diabatic electronic Hamiltonian introduced in Eq.(3.1) (see Appendix A for details) [22]. One dimensional cuts of the multidimensional potential energy hypersurface of the phenyl radical along

Table 3.3: The linear vibronic coupling parameters (λ_i) for the $\widetilde{A}^2B_1$ - $\widetilde{B}^2A_2$ electronic states of the phenyl radical derived from the OVGF data. The dimensionless coupling strengths $\lambda^2/2\omega^2$ are given in parentheses. The vertical ionization energies of the ground and two excited states of the phenyl radical are also given. All quantities are given in eV.

modes		λ
(symmetry)		$\widetilde{A}^2B_1$ - $\widetilde{B}^2A_2$
$\nu_{16}(b_2)$		0.074 (0.459)
$\nu_{17}(b_2)$		0.013 (0.005)
$\nu_{18}(b_2)$		0.057 (0.081)
$\nu_{19}(b_2)$		0.022 (0.009)
$\nu_{20}(b_2)$		-
$\nu_{21}(b_2)$		0.092 (0.131)
$\nu_{22}(b_2)$		0.147 (0.277)
$\nu_{23}(b_2)$		-
$\nu_{24}(b_2)$		0.007 (0.0001)
$E^0_{A_1}$	1.007	
$E^0_{B_1}$	2.862	
$E^0_{A_2}$	3.433	

the dimensionless normal coordinates of the totally symmetric vibrational modes ν_1 - ν_{10} are shown in Fig. 3.3. The potential energies of the $\widetilde{X}$, $\widetilde{A}$ and $\widetilde{B}$ states of the phenyl radical obtained from the model are shown by the solid, dashed and dotted lines, respectively. The points superimposed on them represent the computed *ab initio* energies. It can be seen that the latter are well reproduced by the quadratic vibronic model. A few relevant details are immediately revealed by the potential energy curves of Fig. 3.3. At the vertical configuration ($\mathbf{Q} = 0$), the $\widetilde{X}$ state is well separated from the $\widetilde{A}$ and $\widetilde{B}$ states. The crossing of the $\widetilde{X}$ state with the $\widetilde{A}$ state (for example, along ν_1, ν_2 and ν_7 vibrational modes) occurs at much higher energies (> 5 eV) which is not relevant for the energy range of the photoelectron bands considered here. Moreover, these crossings occur at much larger values of the dimensionless normal coordinate of these vibrational modes, and it is very unlikely for such large amplitude nuclear vibrations to be relevant for the photodetachment process treated here.
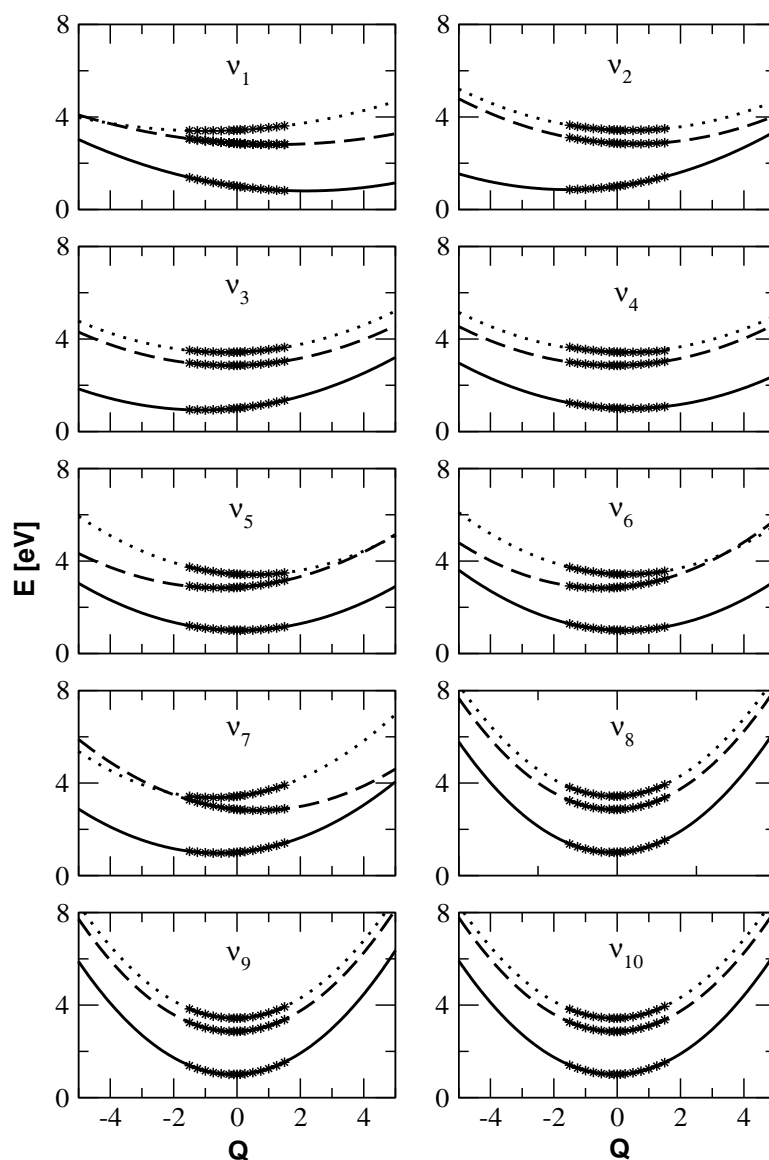
Figure 3.3: One-dimensional cuts of the $\widetilde{X}^2A_1$ (solid line), $\widetilde{A}^2B_1$ (dashed line) and $\widetilde{B}^2A_2$ (dotted line) electronic states of $C_6H_5^\bullet$ as a function of the dimensionless normal coordinates of the totally symmetric (a_1) vibrational modes, ν_1-ν_{10}. The potential energy surfaces are obtained with the quadratic vibronic coupling scheme. The computed *ab initio* potential energies of these states are superimposed and shown by the asterisks on each curve. The equilibrium geometry of $C_6H_5^-$ in its electronic ground state $(\widetilde{X}^1A_1)$ corresponds to $\mathbf{Q} = 0$.

The crossings of $\widetilde{A}$ and $\widetilde{B}$ electronic states, on the other hand, occur in the accessible energy region of the second and third photoelectron bands. For example, the crossings of these two electronic states (above 3.0 eV) are immediately seen from Fig. 3.3 along the ν_1, ν_5, ν_6 and ν_7 vibrational modes. These lead to the formation of multidimensional CIs between these two states. Within the linear coupling scheme the global energetic minimum [22] of the seam of the CIs is estimated to occur at $\approx$ 3.28 eV. For illustration, the seam of CIs in the space of the Q_1 and Q_7 vibrational modes is schematically shown in Fig. 3.4(a). The energetic minimum on this seam occurs at $\approx$ 3.4 eV, for $Q_1 \approx 2.55$ and $Q_7 \approx$ -0.65. A three dimensional perspective view of the $\widetilde{A}$ - $\widetilde{B}$ CIs is shown in Fig. 3.4(b). The adiabatic potential energies of the $\widetilde{A}$ and $\widetilde{B}$ electronic states of the phenyl radical are plotted along the dimensionless normal coordinates of Q_7 and Q_{16} vibrational modes. It can be seen from the perspective plot that the intersection of the two surfaces occurs quite near to the minimum of the $\widetilde{B}$ electronic state. Therefore, the vibrational structure of the high-energy wing of the second ($\widetilde{A}$) and that of the entire third ($\widetilde{B}$) band is expected to be strongly perturbed by the associated nonadiabatic coupling.

3.3.2 Photodetachment spectra

3.3.2.1 The first photoelectron band

The first photoelectron band is calculated by the matrix diagonalization approach using the Lanczos algorithm. It is discussed above, that the coupling between the $\widetilde{X}$ state with the $\widetilde{A}$ and $\widetilde{B}$ electronic states occurs much beyond the energy range of the first photoelectron band and the coupling strength is also very weak, therefore, the nuclear motion in the $\widetilde{X}$ state is considered to remain insensitive to this coupling, and treated to proceed adiabatically on this electronic state. According to the symmetry selection rule stated above, only the totally symmetric vibrational modes can have non-zero first-order (intrastate) coupling in the $\widetilde{X}$
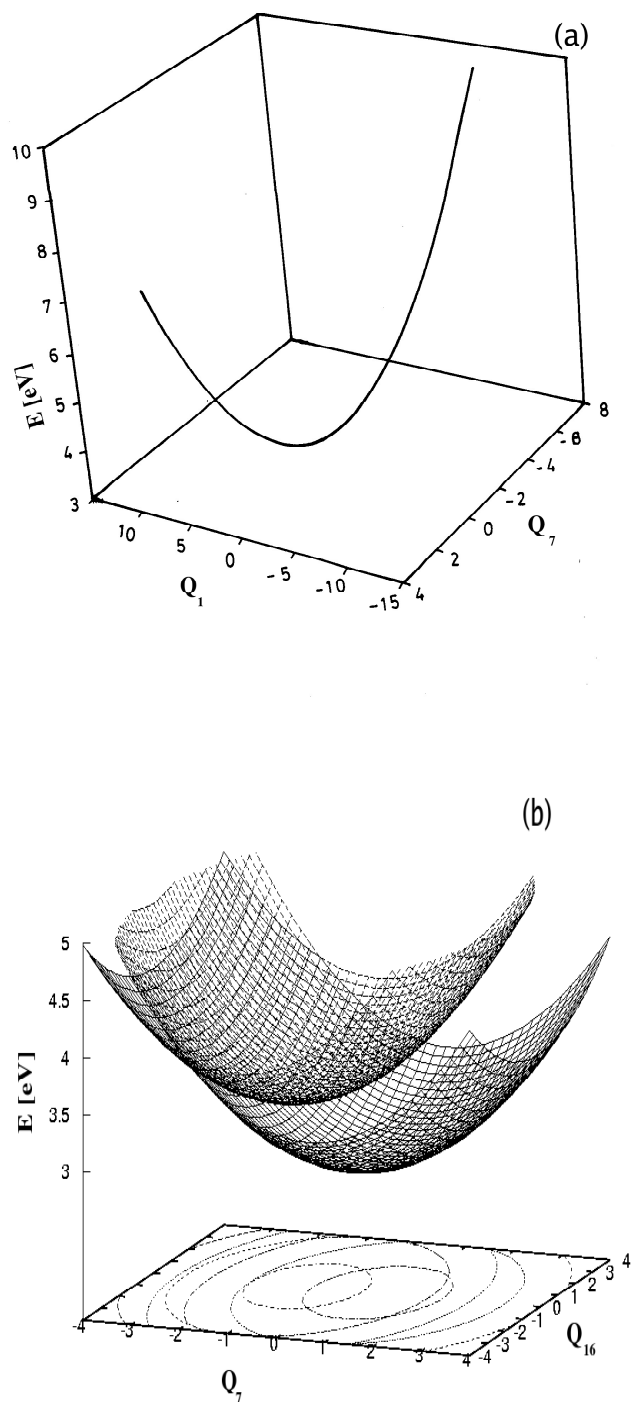
Figure 3.4: (a) The seam of CIs between $\widetilde{A}^2B_1$ and $\widetilde{B}^2A_2$ electronic states of the phenyl radical, calculated along the normal coordinates of the ν_1 and ν_7 vibrational modes. (b) Three dimensional perspective view of the $\widetilde{A}$ - $\widetilde{B}$ CIs in the subspace of ν_7 (a_1) and ν_{16} (b_2) vibrational modes.

state [see the Hamiltonian Eq. 3.1(d)]. Out of the ten, only three (ν_1, ν_2 and ν_3) totally symmetric modes exhibit large first-order coupling, (cf., Table 3.2). In the quadratic vibronic model employed here, the second-order terms due to all vibrational modes can have non-zero contribution to the Hamiltonian. A careful examination of the coupling strengths (cf., Table. 3.2) of all the vibrational modes reveals that not all of them are significant for the nuclear dynamics and therefore, a selection has been made based on extensive trial calculations. The final theoretical results are presented in the lower panel of Fig. 3.5 along with the experimental results of Ref [110], in the upper panel. The theoretical stick spectrum in Fig. 3.5 is obtained by considering four a_1 (ν_1, ν_2, ν_3 and ν_7), five b_1 (ν_{11}, ν_{12}, ν_{13}, ν_{14} and ν_{15}) and three a_2 (ν_{25}, ν_{26} and ν_{27}) vibrational modes. A vibrational basis consisting of 30, 12, 6, 3, 5, 5, 3, 3, 3, 3, 2 and 2 harmonic oscillator functions (in that order) is employed.

This leads to a secular matrix of dimension 5,24,88,000 which is diagonalized using 5000 Lanczos iterations. The second-order coupling parameters due to the b_2 vibrational modes are very small (cf., Table 3.2) and therefore are not included in the calculations. Also the bilinear a_1-a_1, a_1-b_1 and b_1-b_1 coupling parameters are not significant ($< 10^{-2}$ and inclusion of them in them in the simulations does not cause any noticeable change in the spectrum). The stick theoretical spectrum of Fig. 4 is convoluted with a Lorentzian line shape function of 20 meV full width at the half maximum (FWHM), to generate the spectral envelope. A similar convolution procedure is applied to all later stick spectra shown in this chapter. It can be seen from Fig. 3.5 that the theoretical results compare well with the experiment despite a few minor discrepancies. We note that anomalous intensity distributions were observed in the experimental measurements [110] because of possible contamination from the overlapping benzyne anion spectrum. A further improvement of the energy resolution in the experimental recording may also reveal the additional splitting of lines obtained in the theoretical envelope.

The first peak in the experimental envelope is attributed to a hot band con-
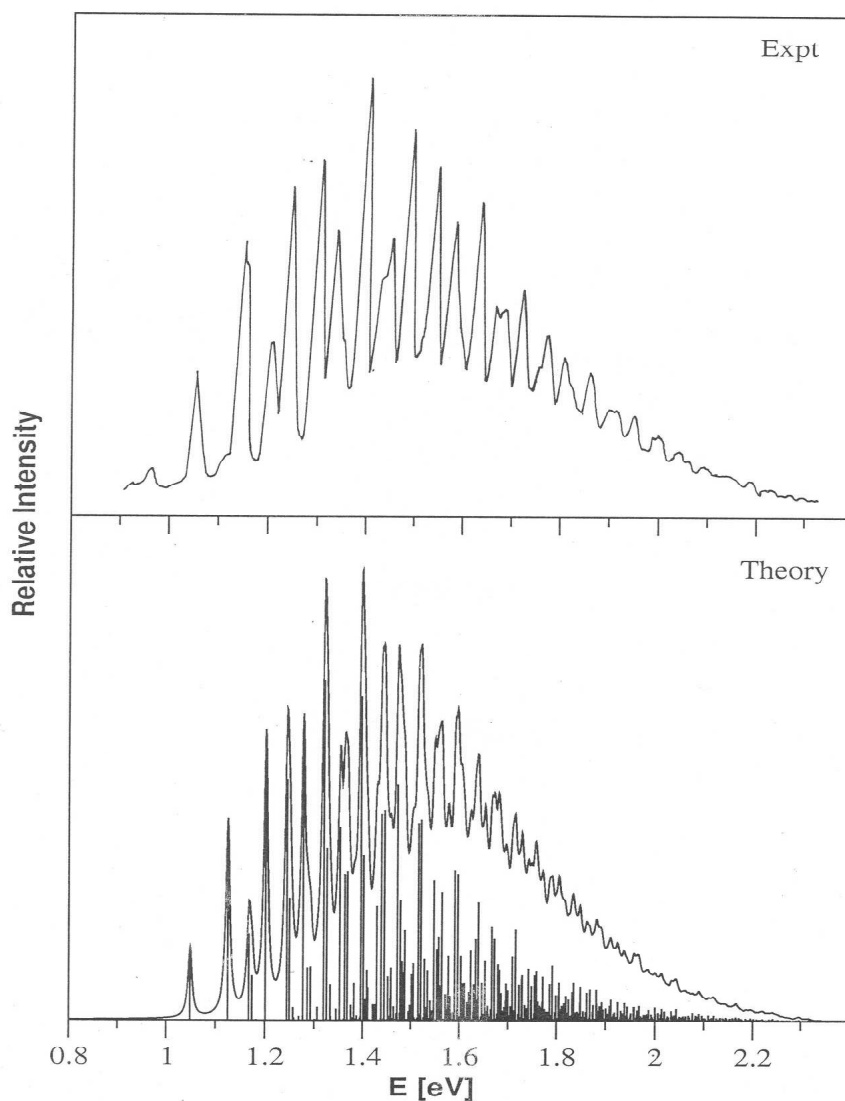
Figure 3.5: The first photoelectron band of the $\widetilde{X}^2 A_1$ electronic state of $C_6H_5^{\bullet}$ computed with 12 [four a_1 (ν_1, ν_2, ν_3, and ν_7), five b_1 (ν_{11}, ν_{12}, ν_{13}, ν_{14} and ν_{15}), and three a_2 (ν_{25}, ν_{26} and ν_{27})] modes and the quadratic vibronic Hamiltonian [Eq. (3.1d)]. The experimental (reproduced from [110]) and theoretical results are shown in the upper and lower panels, respectively. The theoretical stick spectrum is convoluted with a Lorentzian function of 20 meV FWHM to calculate the spectral envelope. The theoretical spectrum is shifted by 0.4 eV to the higher energy along the abscissa to reproduce the adiabatic ionization position of the band at its experimental value.

tribution which has no counterpart in the theoretical envelope. This is because our theoretical results correspond to zero temperature simulations. The dominant progressions in the theoretical band are formed by the ν_1 and ν_2 vibrational modes. The peaks are ~ 0.0727 eV and ~ 0.1196 eV spaced in energy and correspond to the vibrational frequencies of these modes. The vibrational mode ν_3 is only weakly excited. In order to establish this assignment unambiguously we performed two modes calculations also. The results obtained with $\nu_1\nu_2$, $\nu_1\nu_3$, and $\nu_2\nu_3$ combinations are shown in Figs. 3.6(a-c). It can be seen from these plots that the $\nu_1\nu_2$ combination reproduces the envelope quite closer to the experiment [110]. Therefore, ν_1 and ν_2 vibrational modes are the crucial ones (also revealed by their excitation strengths; cf., Table 3.2) and form most of the progressions observed in the experiment. Finally the spectrum obtained by including all ten a_1 vibrational modes is also shown Fig. 3.6(d). It can be seen that the dominant structures in the latter spectrum are much similar to the spectrum in Fig. 3.6(a). Inclusion of additional modes increases the line density in the spectrum due to the multimode effect [22]. Since, apart from ν_1 and ν_2 all other vibrational modes have very weak excitation strengths (cf., Table 3.2), the dominant spacings of the cluster of lines correspond nearly to the frequencies of ν_1 and ν_2 vibrational modes only. These two vibrational modes are schematically shown Fig. 3.7, they describe deformations of the benzene ring.

3.3.2.2 The overlapping second and third photoelectron bands

The second and third photoelectron bands of the phenide anion are found to be highly overlapping. These two bands represent to the vibronic structures of the $\widetilde{A}$ and $\widetilde{B}$ electronic states of the phenyl radical, respectively. It is already stated above that these two electronic states are ~ 0.57 eV spaced in energy at the vertical configuration and low-energy CIs with an energetic minimum at ~ 3.3 eV are discovered between these two electronic states [for example, see, Figs. 3.4(a-b) and the related discussions]. Therefore, nonadiabatic effects due
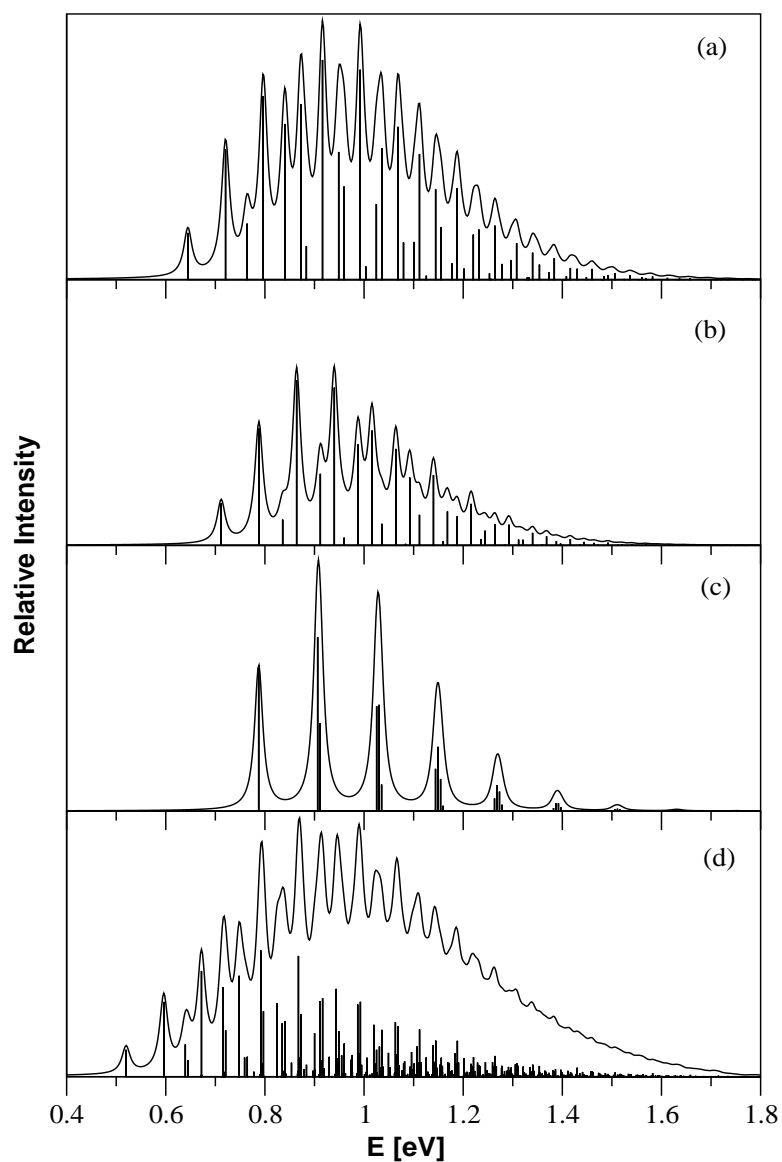
Figure 3.6: The theoretical first photoelectron band of the phenyl radical obtained with (a) ν_1 and ν_2, (b) ν_1 and ν_3, (c) ν_2 and ν_3 and (d) all ten ν_1- ν_{10} totally symmetric vibrational modes. Each theoretical stick spectrum is convoluted with the Lorentzian function of 20 meV FWHM to calculate the spectral envelope.
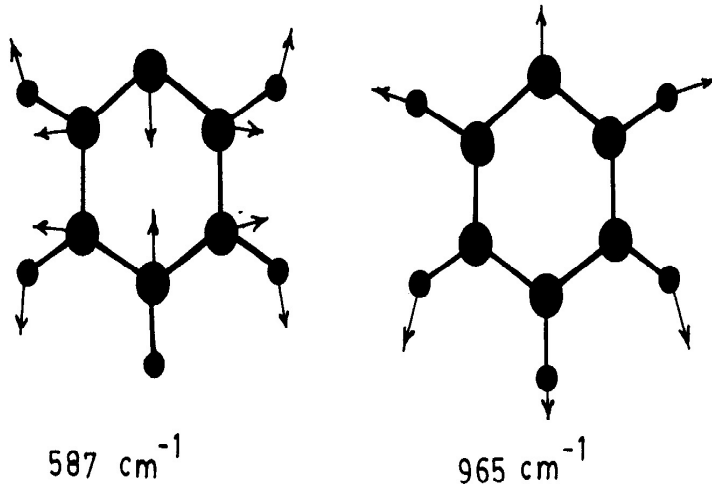
Figure 3.7: The two totally symmetric vibrational modes (ν_1 and ν_2) of the ring deformation type which show the most dominant progressions in the first photoelectron band.

to these energetically relevant CIs are expected to play the most crucial role on the vibronic dynamics in the coupled $\widetilde{A}$ - $\widetilde{B}$ electronic states of phenyl radical. In the following, we first discuss the photoelectron bands of the uncoupled $\widetilde{A}$ and $\widetilde{B}$ electronic states of the phenyl radical obtained by the time-independent matrix diagonalization approach. Subsequently, the nuclear dynamics in the coupled $\widetilde{A}$ - $\widetilde{B}$ electronic states is considered, and a simulation of this including all relevant vibrational degrees of freedom was found to be computationally impracticable by the usual Hamiltonian matrix diagonalization scheme. This task is therefore accomplished by the wave packet propagation method using the efficient MCTDH algorithm [109]. In addition to the coupled states vibronic spectrum, this also yields the time dependence of electronic populations and hence provides valuable information on the nonradiative decay of the excited electronic states of the phenyl radical.

In Fig. 3.8, we show the second photoelectron band pertinent to the uncoupled $\widetilde{A}$ state of the phenyl radical along with the experimental optical absorption
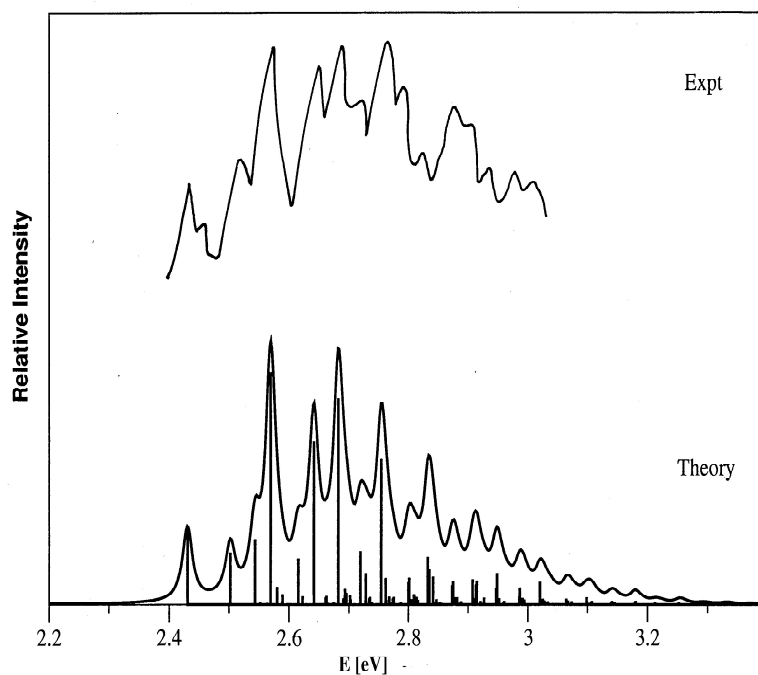
Figure 3.8: The second photoelectron band revealing the vibronic level spectrum of $\widetilde{A}^2 B_1$ electronic state of the phenyl radical. The experimental UV absorption spectrum for this electronic state reproduced from Ref. [117] and included in the panel. The relative intensity (in arbitrary units) is plotted as a function of the energy of the levels of the final vibronic state. The theoretical stick spectrum calculated with 15 [six a_1 (ν_1, ν_2, ν_3, ν_5, ν_6 and ν_7), four b_1 (ν_{11}, ν_{12}, ν_{13} and ν_{15}), four b_2 (ν_{16}, ν_{18}, ν_{21} and ν_{22}), and one a_2 (ν_{25})] vibrational modes and the quadratic vibronic Hamiltonian [Eq. (3.1e)] with out considering the coupling with the $\widetilde{B}^2 A_2$ electronic state. The theoretical stick spectrum is convoluted with a Lorentzian function of 20 meV FWHM to calculate the spectral envelope.

spectrum of this state [117] . The stick spectrum is obtained by including six a_1 (ν_1, ν_2, ν_3, ν_5, ν_6, and ν_7), four b_1 (ν_{11}, ν_{12}, ν_{13} and ν_{15}), five b_2 (ν_{16}, ν_{19}, ν_{20}, ν_{22} and ν_{23}) and one a_2 (ν_{25}) vibrational modes in the dynamical simulation. A secular matrix of dimension 79,626,24 obtained by using 6, 2, 2, 2, 2, 2, 4, 4, 3, 2, 3, 2, 3, 4, 2 and 3 harmonic oscillator basis functions (in that order) is diagonalized employing 5000 Lanczos iterations. The spectral envelope is calculated by convoluting the stick spectrum by a Lorentzian function of 20 meV FWHM. The major progressions in the spectrum of Fig. 3.8 are formed by ν_1, ν_2, ν_3 and ν_5 vibrational modes. The dominant lines are $\sim$ 0.072 eV, $\sim$ 0.113 eV, $\sim$ 0.12 eV and $\sim$ 0.14 eV spaced in energy corresponding to the frequencies of these vibrational modes, respectively. It can be seen from Fig. 3.8 that the rich vibronic structure of the experimental band is very well reproduced by the theoretical results particularly at low energies. We note that Kim *et al.* have performed multireference *ab initio* calculations in order to assign the observed vibronic transitions in this band [122]. However the spectrum calculated by them was found to contain significantly less lines than observed [122]. The present theoretical simulation considers a photodetachment process rather than the electronic absorption recording. Therefore, the apparent disagreement in the intensity of the peaks between the theoretical and experimental results of Fig. 3.8 is obtained. Despite a good match between the theory and experiment, the theoretical band seems to have too much structures in the high-energy wing (beyond $\sim$ 2.9 eV) of the spectrum.

There is no clear experimental evidence so far in the literature supporting the existence of $\widetilde{B}^2A_2$ electronic state of the phenyl radical. This is partly because the photodetachment experiments were not carried out at such high energy of photon and partly due to the fact that this state is optically dark and could not be probed by the optical absorption spectroscopy. There is however a broad and poor signal observed in the photodetachment recording in the energy range of $\widetilde{B}$ electronic state [110]. This is attributed to an excited electronic state of the
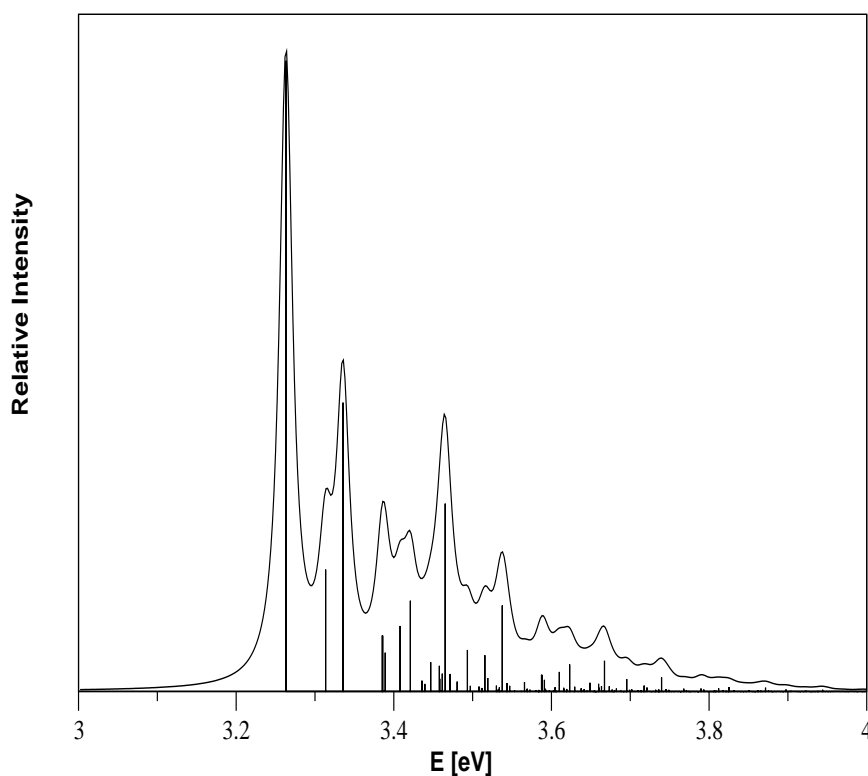
Figure 3.9: The third photoelectron band of revealing the vibronic level spectrum of the $\widetilde{B}^2A_2$ electronic state of the phenyl radical. The theoretical stick spectrum is calculated with 15 [six a_1 (ν_1, ν_2, ν_3, ν_5, ν_6 and ν_7), four b_1 (ν_{11}, ν_{12}, ν_{13} and ν_{15}), four b_2 (ν_{16}, ν_{18}, ν_{21} and ν_{22}), and one a_2 (ν_{25})] vibrational modes and the quadratic vibronic Hamiltonian [Eq. (3.1f)] without considering the coupling with the $\widetilde{A}^2B_1$ electronic state. The relative intensity (in arbitrary units) is plotted as a function of the energy of the levels of the final vibronic state. The theoretical stick spectrum is convoluted with a Lorentzian function of 20 meV FWHM to calculate the spectral envelope.

phenyl radical [110]. This information is too sketchy and cannot be compared with the present theoretical data. The discrepancy between the theoretical (Kim *et al* [122]) and experimental (Radziszewski [117]) results however speculated to be due to the nonadiabatic coupling with a nearby electronic state of A_2 symmetry by the former authors. We here consider this issue and show that such coupling does exist and the associated nonadiabatic effects cause a demolition of the vibronic structures in the high-energy tail of the $\widetilde{A}^2 B_1$ band and that of the entire $\widetilde{B}^2 A_2$ band. The vibrational structure of the uncoupled $\widetilde{B}$ electronic state of the phenyl radical (corresponding to the third photoelectron band of phenide anion) is shown in Fig. 3.9. The theoretical stick spectrum is obtained by considering fifteen [six a_1 (ν_1, ν_2, ν_3, ν_5, ν_6, and ν_7), four b_1 (ν_{11}, ν_{12}, ν_{14} and ν_{15}), four b_2 (ν_{16}, ν_{18}, ν_{21} and ν_{22}) and one a_2 (ν_{25})] vibrational modes and using 7, 2, 2, 2, 2, 5, 4, 2, 2, 2, 2, 2, 2, 3 and 3 harmonic oscillator basis functions along these modes, in that order. The resulting secular matrix of dimension 12,902,40 is diagonalized using 5000 Lanczos iterations. The theoretical stick data is convoluted with a Lorentzian of 20 meV FWHM to generate the spectral envelope. The spectrum in Fig. 3.9 reveals well resolved progressions due to the ν_1, ν_2, ν_3 and ν_6 vibrational modes. Peak spacings of ~ 0.072 eV, ~ 0.113 eV, ~ 0.12 eV and ~ 0.18 eV can be observed from the spectrum.

We now consider the nonadiabatic coupling between the $\widetilde{A}$ and $\widetilde{B}$ electronic states and simulate the nuclear dynamics including all relevant vibrational modes. It is discussed before, that this coupling in first-order is caused by the vibrational modes of b_2 symmetry. The data given in Table 3.3 reveal that the vibrational modes ν_{16}, ν_{18}, ν_{21} and ν_{22} have moderate coupling strengths and are expected to have some impact on the vibronic dynamics in the coupled electronic states. The second order coupling parameters of nine b_2 vibrational modes (cf., Table 3.2) reveal that each one of them is important in either of the two electronic states. Therefore, although only four b_2 modes are relevant from the coupling point of view, it is necessary to include others also for the reason stated above.
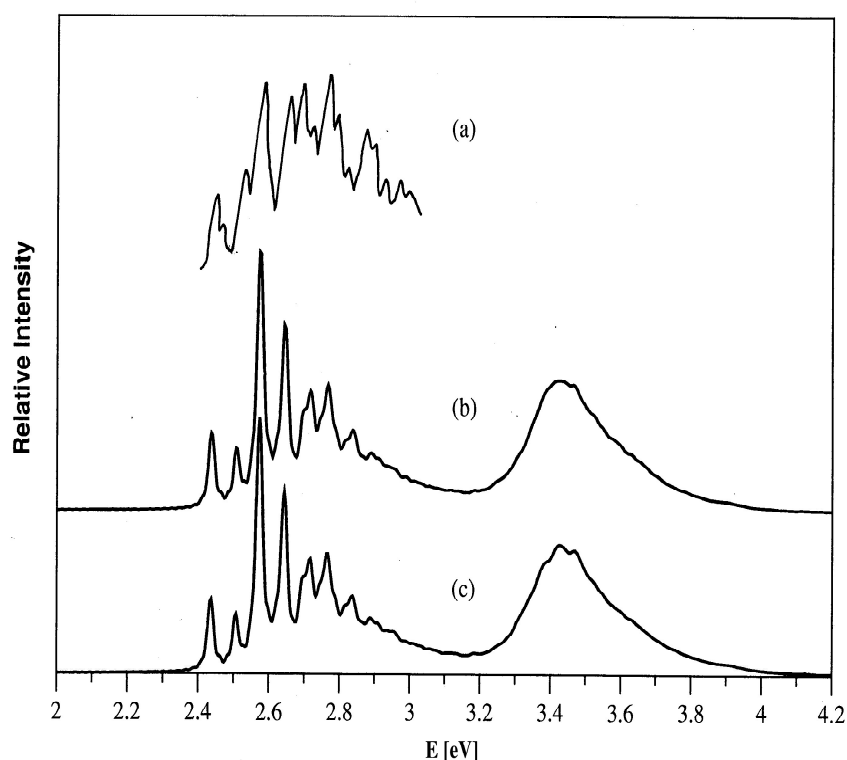
Figure 3.10: The final theoretical photoelectron bands pertinent to the coupled $\widetilde{A}^2B_1$ - $\widetilde{B}^2A_2$ electronic states of phenyl radical. The theoretical bands are obtained by propagating wave packets within the MCTDH scheme using (b) the 21 most relevant and (c) all 27 vibrational modes of phenide anion. For comparison the UV absorption band of the $\widetilde{A}$ electronic state of the phenyl radical is reproduced from Ref. [117] in the panel and indicated as (a). The theoretical spectrum is shifted by 0.5 eV to the lower energy along the abscissa to reproduce the adiabatic ionization position of the band at the observed value in the optical absorption.

The final theoretical simulation therefore involves two electronic states ($\widetilde{A}$ and $\widetilde{B}$) and six a_1 (ν_1, ν_2, ν_3, ν_5, ν_6, and ν_7), four b_1 (ν_{11}, ν_{12}, ν_{13} and ν_{15}), nine b_2 (ν_{16}, ν_{17}, ν_{18}, ν_{19}, ν_{20}, ν_{21}, ν_{22}, ν_{23} and ν_{24}) and two a_2 (ν_{25} and ν_{26}) vibrational modes. This leads to a problem of enormous size which cannot be solved by the matrix diagonalization approach. To this end we also included all 27 vibrational degrees of freedom to simulate the spectrum. These tasks were accomplished by propagating wave packets using the MCTDH algorithm [109]. The details of the mode combinations, sizes of the primitive and single particle bases used in these simulations are given in Table 3.4. The vibrational modes are grouped into multidimensional particles and thereby the computational overhead is reduced. The theoretical photoelectron bands along with the experimental absorption spectroscopy results for the $\widetilde{A}$ electronic state are shown in Fig. 3.10. In the panel, the spectra marked by a, b and c represent the experimental absorption band of the $\widetilde{A}$ electronic state (reproduced from the reference [117]), the theoretical photodetachment spectrum of the coupled $\widetilde{A}$ - $\widetilde{B}$ electronic states considering 21 most relevant vibrational modes and the same including all 27 vibrational modes, respectively. Each theoretical spectrum of Fig. 3.10 is generated by combining two partial spectra obtained for two different ($\widetilde{A}$ or $\widetilde{B}$) initial location of the wave packet. In each calculation the wave packet is propagated up to 100 fs, and since we use a real initial wave packet this yields time autocorrelation function up to 200 fs [124]. The latter is then damped with an exponential function [exp ($-t/\tau_r$); with $\tau_r = 66$ fs which corresponds to a 20 meV FWHM Lorentzian] and Fourier transformed to generate the spectrum. In representing the spectrum the intensity in arbitrary units is plotted as a function of the energy of the final vibronic states. The adiabatic ionization position of the theoretical band is adjusted to that of the experimental absorption band of the $\widetilde{A}$ state occurring at ~ 2.4 eV. This quantity is not so far measured in a photodetachment experiment.

Apart from some expected discrepancies between the theory and experiment for the intensities of the peaks of the $\widetilde{A}$ band, the main vibronic structure and the

Table 3.4: Normal mode combinations, sizes of the primitive and single particle bases used in the MCTDH calculations for the coupled $\widetilde{A}^2B_1$ - $\widetilde{B}^2A_2$ electronic states of phenyl radical.

Normal modes	Primitive basis [a]	SPF basis [b] $[\widetilde{A}^2B_1, \widetilde{B}^2A_2]$	Fig.
(ν_1, ν_3, ν_6)	(40, 10, 5)	[15,12]	
(ν_2, ν_5, ν_7)	(33, 5, 4)	[8,10]	
$(\nu_{11}, \nu_{12}, \nu_{13}, \nu_{15}, \nu_{26})$	(4, 3, 2, 2, 4)	[5,4]	3.10(b)
$(\nu_{16}, \nu_{17}, \nu_{18}, \nu_{19} \, \nu_{25})$	(5, 4, 5, 4, 4)	[6,6]	
$(\nu_{20}, \nu_{21}, \nu_{22}, \nu_{23} \, \nu_{24})$	(4, 4, 4, 4, 4)	[4,5]	
$(\nu_1, \nu_9, \nu_{10}, \nu_{13}, \nu_{17})$	(40, 4, 4, 2, 4)	[15,12]	
$(\nu_2, \nu_4, \nu_8, \nu_{16}, \nu_{22}, \nu_{27})$	(33, 5, 5, 5, 4, 4)	[8,10]	
$(\nu_3, \nu_7, \nu_{11}, \nu_{14}, \nu_{15}, \nu_{26})$	(10, 4, 4, 2, 2, 4)	[5,4]	3.10(c)
$(\nu_6, \nu_{12}, \nu_{18}, \nu_{19}, \nu_{25})$	(5, 3, 5, 4, 4)	[6,4]	
$(\nu_5, \nu_{20}, \nu_{21}, \nu_{23}, \nu_{24})$	(5, 4, 4, 4, 4)	[4,5]	

[a] The primitive basis is the number of harmonic oscillator DVR functions, in the dimensionless coordinate system required to represent the system dynamics along the relevant mode. The primitive basis for each particle is the product of the one-dimensional bases; e.g for particle 1 in the set given for Fig. 3.10(b) the primitive basis contains $40 \times 10 \times 5 = 2000$ functions and the full primitive basis consists of a total of 4.15×10^{14} functions. For Fig. 3.10(c) the full primitive basis consists of 1.33×10^{19} functions. [b] The SPF basis is the number of single-particle functions used. There are 28,800 and 24,000 configurations altogether for Fig. 3.10(b) and Fig. 3.10(c) calculations respectively.

progressions of the vibrational modes are reproduced satisfactorily. Furthermore, the results of 21 modes and 27 modes calculations are essentially identical. The available experimental spectroscopic data do not reveal any clear evidence of $\widetilde{B}$ and therefore results on this state shown here as a theoretical prediction. Strong impact of nonadiabatic coupling is immediately visible by comparing the above theoretical results with those obtained for the uncoupled $\widetilde{B}$ and $\widetilde{A}$ states (cf., Figs 3.9, 3.8). The nonadiabatic coupling causes a partial demolition of the vibronic structure in the high energy wing of the $\widetilde{A}$ band and it has huge impact on the vibronic structure of the $\widetilde{B}$ band. The energetic minimum of the CIs of the multidimensional potential energy hypersurfaces occurs at $\sim$ 3.28 eV and this almost coincides at the minimum of the $\widetilde{B}$ state estimated at $\sim$ 3.27 eV. Therefore, although the strength of nonadiabatic coupling is not very strong (cf., Table 3.3), it severely affects the $\widetilde{B}$ band and as a result the vibronic structure of the latter is completely demolished and it is transformed to a diffuse broad bump. It would be worthwhile to carry out photodetachment experiment to validate these new findings.

3.3.3 Time-dependent dynamics

The time dependence of electronic populations provide valuable information on the decay of an excited molecular state which can be measured in a femtosecond time resolved experiment. In the present case this decay is solely driven by the CIs and the associated nonadiabatic coupling. The energetic locations of the minimum of the seam of CIs as well as the minimum of the participating electronic states solely governs the nonadiabatic decay process.

In Fig. 3.11 we show the time-dependence of the diabatic electronic populations of the $\widetilde{A}$ and $\widetilde{B}$ electronic states of the phenyl radical in the coupled-states situations. In panel (a), the diabatic electronic populations of the $\widetilde{A}$ (shown by the solid line) and $\widetilde{B}$ (shown by the dashed line) electronic states obtained by

locating the wave packet initially (at $t = 0$) on the $\widetilde{A}$ electronic state are plotted. These populations are obtained by propagating the wave packet including all 27 vibrational degrees of freedom. It can seen that very little population transfer occurs to the $\widetilde{B}$ electronic state in this situation. This is because the energetic minimum of the seam of intersections occurs at higher energy and the low lying vibronic levels of the $\widetilde{B}$ state are not perturbed by the nonadiabatic interactions. In contrast, a large population transfer occurs through the $\widetilde{A}$ - $\widetilde{B}$ CIs when the wave packet is initially located on the $\widetilde{B}$ state. The diabatic electronic populations obtained in this situation are plotted in panel (b). As stated before that the minimum of this state nearly coincides with the minimum of the seam of intersections and therefore, a profound effect of the nonadiabatic coupling prevails on the vibronic dynamics of the $\widetilde{B}$ state. It can be seen that the population of this state (dashed line) starting from 1.0 at t=0 sharply decays to less than 0.1 in about 30 fs and reaches to a value of ~ 0.05 at longer times. The population of the $\widetilde{A}$ state on the other hand starting from 0.0 at t=0 grows to a value ~ 0.95 at longer time. The initial sharp decrease of the population of the $\widetilde{B}$ state relates to a decay rate of ~ 30 fs of this state.

3.4   Summary and Outlook

We have presented a detailed theoretical account of the photodetachment spectroscopy of the phenide anion. The vibronic structures of the ground $\widetilde{X}^2 A_1$ and two low-lying excited $\widetilde{A}^2 B_1$ and $\widetilde{B}^2 A_2$ electronic states of phenyl radical are examined. A vibronic coupling model is established with the aid of extensive electronic structure calculations and the nuclear dynamics is simulated by solving the quantum eigenvalue equation both in time-independent and time-dependent framework.

The $\widetilde{X}$ state of the phenyl radical is energetically well separated from the $\widetilde{A}$ and $\widetilde{B}$ states. Whereas, the latter two states are energetically close to each
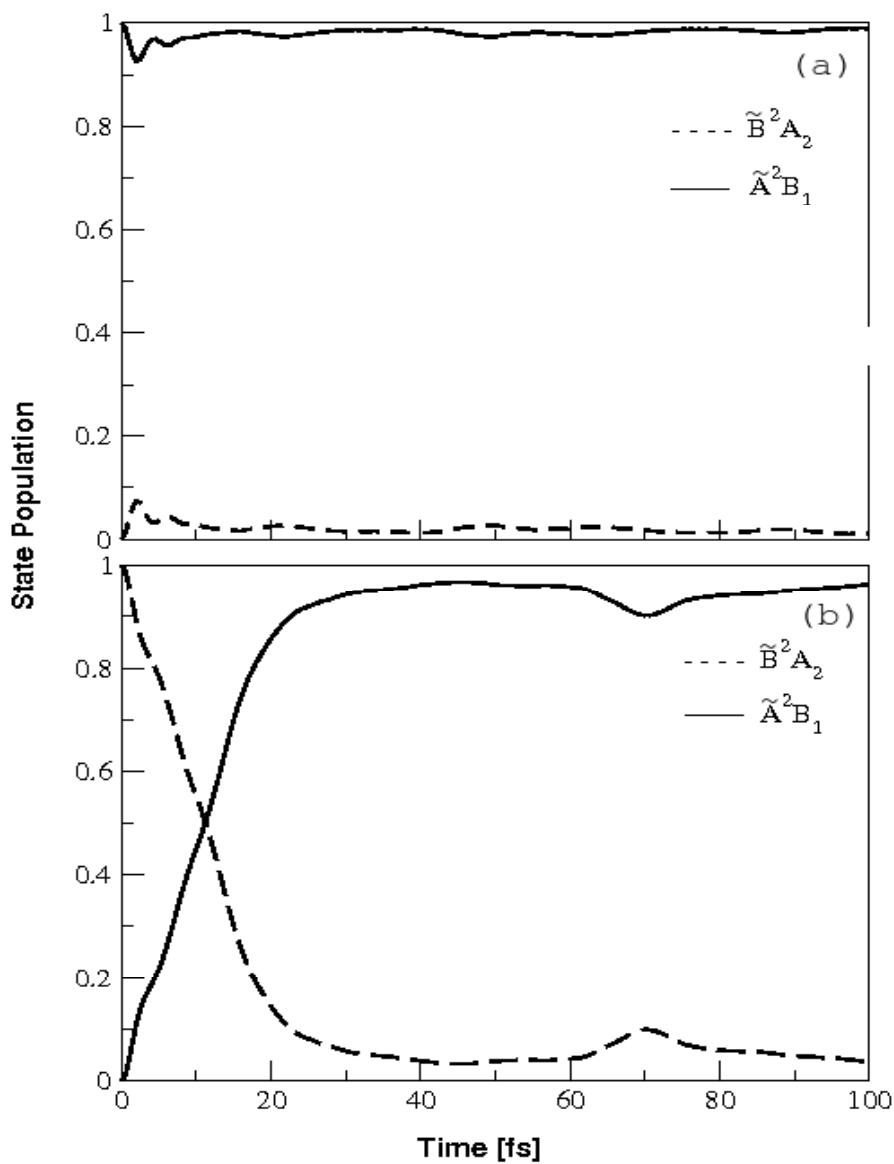
Figure 3.11: Time dependence of the diabatic electronic populations in the coupled states simulations of Fig. 3.10. The populations of the $\widetilde{B}$ and $\widetilde{A}$ states are shown by the dashed and solid lines, respectively. The upper and lower panel corresponds to the initial location of the wave packet on the $\widetilde{A}$ and $\widetilde{B}$ state, respectively.

other. The possible symmetry allowed crossings among these three electronic states are examined. It is found that the $\widetilde{X}$ state undergoes crossings with the $\widetilde{A}$ and $\widetilde{B}$ states at much higher energies (beyond 5 eV) and such crossings are not relevant for the energy range of the first three bands of the photodetachment spectrum. Furthermore, the strength of the coupling between the $\widetilde{X}$ state and either of the $\widetilde{A}$ and $\widetilde{B}$ electronic state is very small. The crossings between the $\widetilde{A}$ and $\widetilde{B}$ electronic states on the other hand, occurs at much lower energy and are relevant for the energy range of the second and third photoelectron bands. Low-energy CIs between these two states are discovered and their impact on the vibronic structures of these electronic states is examined.

The theoretical results on the first band are in good accord with the resolved vibrational progressions observed in the experimental photodetachment recording. Two totally symmetrical vibrational modes of ring deformation type (ν_1 and ν_2) form the major progression in this photoelectron band. The existing ambiguity in the assignment of these progressions is resolved here.

The experimental photodetachment spectrum of the $\widetilde{A}$ state is not available. However, information on the vibronic level structure of this state is available from the electronic absorption spectroscopic measurements. The rich vibronic structure observed in the absorption spectrum is very well reproduced in our theoretical nuclear dynamical simulations of the uncoupled $\widetilde{A}$ state. Despite some differences in the intensity of the individual lines. The vibrational modes ν_1, ν_2, ν_3 and ν_5 form most of the progressions in this band. The $\widetilde{B}$ state of the phenyl radical is optically dark and no clear evidence of this state emerged from the photodetachment measurements. In the uncoupled state calculations distinct vibrational progressions due to ν_1, ν_2, ν_3 and ν_6 are found for this electronic state.

The energetic minimum of the $\widetilde{A}$ - $\widetilde{B}$ CIs occurs at ~ 3.29 eV which is located very near to the energetic minimum of the $\widetilde{B}$ state. The final theoretical simulations of the nuclear dynamics in the coupled $\widetilde{A}$ - $\widetilde{B}$ electronic states is carried out by propagating wave packets using the MCTDH algorithm. The theoreti-

cal simulations were carried out by considering the most relevant 21 vibrational degrees of freedom as well as by including all 27 vibrational degrees of freedom also. It is found that the vibronic structures of the high-energy tail of the $\widetilde{A}$ band and the entire $\widetilde{B}$ band are severely affected by the nonadiabatic coupling. As a result the $\widetilde{B}$ band transforms to a broad and structureless envelope in the coupled states situations. Although the nonadiabatic couplings are not particularly strong in this case, the crossing between the $\widetilde{A}$ and $\widetilde{B}$ state occurs nearly at the minimum of the latter state and therefore, such a profound effect of the crossing on the vibronic structure of the $\widetilde{B}$ state is seen. Photodetachment experiments at higher photon energies will be valuable to support these theoretical findings. An ultrafast nonradiative decay rate of ~ 30 fs of the $\widetilde{B}$ state is estimated from the decay of the electronic population in the coupled electronic manifold.

Chapter 4

Electronic nonadiabatic interaction and internal conversion in phenylacetylene radical cation

4.1 Introduction

In this chapter we consider the structural and dynamical aspects of the low-lying electronic states of phenylacetylene radical cation (PA$^+$) and attempt to investigate them by an *ab initio* quantum mechanical approach. Phenylacetylene (PA) belongs to the C$_{2v}$ symmetry point group at the equilibrium geometry of its electronic ground state ($\widetilde{X}^1A_1$). The 36 vibrational modes of PA (shown in Table 4.1) decompose into 13 a_1 $\oplus$ 3 a_2 $\oplus$ 8 b_1 $\oplus$ 12 b_2 irreducible representations (IREPs) of the C$_{2v}$ point group (Table I). The ground and first three excited electronic states of PA$^+$ belong to the $\widetilde{X}^2B_1$, $\widetilde{A}^2A_2$, $\widetilde{B}^2B_2$ and $\widetilde{C}^2B_1$ symmetry species of the equilibrium C$_{2v}$ point group and result from ionization of the first four valence b_1, a_2, b_2 and b_1 type of molecular orbitals (MOs) of PA, respectively. These

canonical MOs, viz., the HOMO (highest occupied MO), HOMO-1, HOMO-2 and HOMO-3 of PA are of π-type MOs. While the HOMO and HOMO-1 represent the π orbitals mainly localized on the phenyl ring, the HOMO-2 and HOMO-3 are representatives of the acetylenic π orbitals parallel and perpendicular to the phenyl ring, respectively.

The gas-phase photoelectron (PE) spectrum of PA$^+$ measured by Rabalias et $al.$ [125] and Lichtenberger et $al.$ [126] revealed resolved vibrational level structure of its $\widetilde{X}^2B_1$, $\widetilde{B}^2B_2$ and $\widetilde{C}^2B_1$ electronic states and a diffuse and structureless band for the $\widetilde{A}^2A_2$ electronic state. The $\widetilde{C} \leftarrow \widetilde{X}$ gas-phase visible absorption spectrum of PA$^+$-Ar van der Waals complex recorded by Bréchignac et $al.$ shows a well resolved vibrational structure of the $\widetilde{C}$ state [127, 128]. An upper limit of non-radiative decay rate of 1.4×10^{12} s^{-1} is estimated from the average line width of the resolved vibrational structure of this state. This decay rate is related to a sub-picoseconds life time of the $\widetilde{C}$ state arising from possible internal conversion within the electronic doublet states of PA$^+$. Youn et $al.$ have predicted a long life time (of the order 10 microseconds) for the $\widetilde{B}$ state of PA$^+$ in a charge exchange ionization followed by mass spectroscopic measurement [129]. The resolved vibrational spectrum of the $\widetilde{X}$ state is recorded by Kwon et $al.$ in a one-photon MATI experiment [130]. An adiabatic ionization energy of 8.8195 $\pm$ 0.0006 eV is estimated from the position of the 0-0 peak of this MATI spectrum [130]. Excitations of both the totally and non-totally symmetric vibrational modes are reported in the MATI spectrum. The latter modes are predicted to appear due to the vibronic coupling of the $\widetilde{X}$ state with the other excited electronic stats of PA$^+$.

Xu et $al.$ have recorded the the PIRI spectrum of the $\widetilde{C}$ electronic state by exciting the ion core of the Rydberg molecule [131]. An adiabatic ionization energy of 11.03 eV is estimated for this state. Again both the totally and non-totally symmetric vibrational modes are reported to form progressions in this state. The width of the vibrational peaks are estimated in the range of 20-40

Table 4.1: Details of the 36 vibrational modes and their frequencies (in cm^{-1}) of the ground electronic state of PA. The theoretical numbers are harmonic where as the experimental ones are fundamentals. Wilson's numbering of the vibrational modes are also given in the parentheses.

symm-etry	mode	MP2 (cc-pVDZ)	Expt([130])	Expt([134])	Mode description
a_1	ν_1	3493	3291 (νCH)	3332	C-H stretching
	ν_2	3247	3083 (20a)	3078 (20a)	C-H stretching
	ν_3	3234	3064 (2)	3067 (2)	C-H stretching
	ν_4	3215	3035 (7a)	3047 (7a)	C-H stretching
	ν_5	2121	2118 (νCC)	2120	C≡C stretching
	ν_6	1652	1598 (8a)	1610 (8a)	C=C stretching
	ν_7	1515	1489 (19a)	1488 (19a)	C=C stretching
	ν_8	1225	1192 (13)	1192 (13)	-C-C≡C-H stretching
	ν_9	1189	1178 (9a)	1175 (9a)	C-H in-plane bending
	ν_{10}	1048	1028 (18a)	1028 (18a)	C-H in-plane bending
	ν_{11}	1009	1000 (12)	998 (1)	C=C=C in-plane bending
	ν_{12}	769	763 (1)	760 (12)	-C≡C-H stretching
	ν_{13}	464	467 (6a)	465 (6a)	-C≡C-H stretching
a_2	ν_{14}	952	971 (17a)	968 (17a)	C-H out-of-plane bending
	ν_{15}	848	842 (10a)	842 (10a)	C-H out-of-plane bending
	ν_{16}	398	418 (16a)	418 (16a)	C=C out-of-plane bending
b_1	ν_{17}	956	986 (5)	985 (5)	C-H out-of-plane bending
	ν_{18}	902	918 (17b)	915 (17b)	C-H out-of-plane bending
	ν_{19}	741	756 (11)	756 (11)	C-H out-of-plane bending
	ν_{20}	636	691 (4)	689 (4)	acetylenic C-H in-plane bending
	ν_{21}	582	610 (γCH)	613	acetylenic C-H out-of-plane bending
	ν_{22}	490	531 (16b)	530 (16b)	C=C out-of-plane bending
	ν_{23}	343	352 (γCC)	349 (10b)	-C-C≡C out-of-plane bending
	ν_{24}	137	165 (10b)	162	-C≡C-H out-of-plane bending
b_2	ν_{25}	3241	- (7b)	3096 (7b)	C-H stretching
	ν_{26}	3224	3058 (20b)	3058 (20b)	C-H stretching
	ν_{27}	1625	1573 (8b)	1573 (8b)	C=C stretching
	ν_{28}	1484	1444 (19b)	1447 (19b)	C=C stretching
	ν_{29}	1449	1331 (14)	1330 (3)	C=C stretching
	ν_{30}	1321	1283 (3)	1282 (14)	C-H in-plane bending
	ν_{31}	1172	1158 (9b)	1157 (9b)	C-H in-plane bending
	ν_{32}	1095	1071 (18b)	1070 (18b)	C-H in-plane bending
	ν_{33}	623	653 (βCH)	649	acetylenic C-H in-plane bending
	ν_{34}	622	619 (6b)	613 (6b)	acetylenic C-H in-plane bending
	ν_{35}	502	516 (βCC)	513	-C≡C-H in-plane bending
	ν_{36}	147	- (15)	162	-C≡C-H in-plane bending

cm^{-1} and found to be broader than the halogen substituted benzene cations. The broadening of the peaks is attributed to a predissociating nature of the $\widetilde{C}$ state or its possible vibronic mixing with the other electronic states. The $\widetilde{C}$ $\leftarrow \widetilde{X}$ visible spectrum of the PA$^+$ measured and compared by Pino *et al.* by employing two methods namely a resonant multiphoton dissociation scheme for the bare cations and a resonant photodissociation technique applied to the PA$^+$-Ar$_{n=1,2}$ ionic complexes [132]. The well resolved vibrational peaks with dominant progression due to the totally symmetric vibrational modes are reported in these measurements.

4.2 The Vibronic Hamiltonian

For the nuclear dynamical simulations, a vibronic Hamiltonian is constructed below in terms of the dimensionless normal coordinates of the vibrational modes and utilizing a diabatic electronic basis [89–91]. The coupling between the states m and n in the diabatic electronic Hamiltonian through a given vibrational mode (Q) is assessed using the symmetry selection rule given in the Chapter 2

$$\Gamma_m \otimes \Gamma_Q \otimes \Gamma_n \supset \Gamma_A \quad ,$$

According to this rule, the totally symmetric (a_1) vibrational modes are always active in a given electronic state and the first-order coupling between the $\widetilde{X}$-$\widetilde{A}$, $\widetilde{X}$-$\widetilde{B}$, $\widetilde{A}$-$\widetilde{B}$, $\widetilde{A}$-$\widetilde{C}$ and $\widetilde{B}$-$\widetilde{C}$ electronic states of PA$^+$ is caused by the vibrational modes of b_2, a_2, b_1, b_2 and a_2 symmetry, respectively. These couplings lead to multiple multidimensional CIs in the mentioned manifold of electronic states of PA$^+$. The impact of the electronic nonadiabatic effects on the vibrational level structure of a state depends on the strength of the associated coupling. A detailed account such effects is exposed in this chapter. Till date, none of the theoretical studies dealt with these details in order to corroborate to the vast

amount of experimental data available on this system. A combination of time-independent/dependent quantum mechanical simulations presented below enable us to explain a large part of the complex vibronic spectrum of PA$^+$ and the dynamics of its excited electronic states. Very good agreement is achieved with the PE spectroscopy data. Despite some differences, the theoretical data also reveal good agreement with the high resolution measurements. Possible avenues for further improvements of the study is also discussed.

The Hamiltonian for the coupled manifold of $\widetilde{X}$-$\widetilde{A}$-$\widetilde{B}$-$\widetilde{C}$ electronic states of PA$^+$ is constructed in terms of the dimensionless normal displacement coordinates (Q) of its 36 nondegenerate vibrational modes in a diabatic electronic basis as

$$
\mathcal{H} \;=\; (\mathcal{T}_N + \mathcal{V}_0)\mathbf{1_4} +
\begin{pmatrix}
W_{\widetilde{X}} & W_{\widetilde{X}-\widetilde{A}} & W_{\widetilde{X}-\widetilde{B}} & W_{\widetilde{X}-\widetilde{C}} \\
 & W_{\widetilde{A}} & W_{\widetilde{A}-\widetilde{B}} & W_{\widetilde{A}-\widetilde{C}} \\
h.c. & & W_{\widetilde{B}} & W_{\widetilde{B}-\widetilde{C}} \\
 & & & W_{\widetilde{C}}
\end{pmatrix},
\tag{4.1a}
$$

where $\mathbf{1_4}$ is a 4×4 unit matrix and $(\mathcal{T}_N + \mathcal{V}_0)$ is the Hamiltonian for the unperturbed electronic ground state of the neutral PA. This reference state is assumed to be harmonic and vibronically decoupled from the other states. Therefore, $\mathcal{T}_N$ and $\mathcal{V}_0$ are given by

$$
\mathcal{T}_N = -\frac{1}{2}\sum_{i=1}^{36}\omega_i\frac{\partial^2}{\partial Q_i^2},
\tag{4.1b}
$$

$$
\mathcal{V}_0 = \frac{1}{2}\sum_{i=1}^{36}\omega_i Q_i^2.
\tag{4.1c}
$$

The non-diagonal matrix Hamiltonian in Eq. (4.1a) represents the change in the electronic energy upon ionization of PA and describes the diabatic electronic PESs (diagonal elements) of the $\widetilde{X}$, $\widetilde{A}$, $\widetilde{B}$ and $\widetilde{C}$ electronic states of PA$^+$ and

their coupling potentials (off-diagonal elements). These are expanded in a Taylor series (excluding the intermode bilinear coupling terms) around the equilibrium geometry of the reference state at ($\mathbf{Q}$=0) as [22]

$$W_j \;=\; E_0^{(j)} + \sum_{i=1}^{13} \kappa_i^{(j)} Q_i + \frac{1}{2} \sum_{i=1}^{36} \gamma_i^{(j)} Q_i^2 \;\; ; \;\; j \;\in\; \widetilde{X}, \widetilde{A}, \widetilde{B}, \widetilde{C} \quad (4.1\text{d})$$

$$W_{j-k} \;\;=\;\; \sum_i \lambda_i^{(j-k)} Q_i \qquad\qquad (4.1\text{e})$$

where $j - k \in \widetilde{X}\text{-}\widetilde{A}, \; \widetilde{X}\text{-}\widetilde{B}, \; \widetilde{A}\text{-}\widetilde{B}, \; \widetilde{A}\text{-}\widetilde{C}, \; \widetilde{B}\text{-}\widetilde{C}$ with $i \in b_2, \, a_2, \, b_1, \, b_2, \, a_2$ in that order. In the above equations the quantity $E_0^{(j)}$ represents the vertical ionization energy of the jth electronic state and $\kappa_i^{(j)}$ and $\gamma_i^{(j)}$ are the linear and second-order coupling parameters of the ith vibrational mode in the jth electronic state. The quantity $\lambda_i^{(j-k)}$ describes the first-order coupling parameter between the j and k electronic states through the vibrational mode i. A linear interstate coupling is considered throughout this study. We find the bilinear coupling terms are smaller in size (of the order of $\sim 10^{-3}$ or less) and therefore not included in the dynamical simulations. These coupling parameters are extracted from *ab initio* electronic structure calculations as mentioned in Chapter 2 and are listed in Table 4.2-4.4.

4.3 Results and Discussions

4.3.1 Adiabatic electronic potential energy surfaces and conical intersections

The adiabatic PESs of the $\widetilde{X}$, $\widetilde{A}$, $\widetilde{B}$ and $\widetilde{C}$ electronic states of PA$^+$ are obtained by diagonalizing the diabatic electronic Hamiltonian of Eq. (4.1a) and the parameters of Tables 4.2-4.4. One dimensional cuts of the multidimensional

Table 4.2: The linear coupling parameters (κ_i) for the $\widetilde{X}^2B_1$, $\widetilde{A}^2A_2$, $\widetilde{B}^2B_2$ and $\widetilde{C}^2B_1$ electronic states of the PA$^+$ derived from the *ab initio* electronic structure data. The dimensionless coupling strengths, $\kappa^2/2\omega^2$, are given in the parentheses. The vertical ionization energies (E^0) of the above electronic states are also given. All quantities are in eV.

modes (symmetry)	frequency (eV)	$\kappa^{(X)}$ $\widetilde{X}^2B_1$	$\kappa^{(A)}$ $\widetilde{A}^2A_2$	$\kappa^{(B)}$ $\widetilde{B}^2B_2$	$\kappa^{(C)}$ $\widetilde{C}^2B_1$
$\nu_1(a_1)$	0.4332	0.0044 (0.0001)	0.0160 (0.0007)	-0.0230 (0.0014)	-0.0053 (0.0001)
$\nu_2(a_1)$	0.4026	-0.0144 (0.0006)	-0.0157 (0.0007)	-0.0113 (0.0001)	-0.0185 (0.0011)
$\nu_3(a_1)$	0.4010	0.0045 (0.0001)	-0.0018 (0.0001)	0.0035 (0.0001)	-0.0043 (0.0001)
$\nu_4(a_1)$	0.3987	0.0025 (0.0001)	-0.0026 (0.0001)	-0.0017 (0.0001)	0.0025 (0.0001)
$\nu_5(a_1)$	0.2631	0.1407 (0.1430)	0.0028 (0.0001)	0.3097 (0.6928)	0.1283 (0.1189)
$\nu_6(a_1)$	0.2049	-0.1322 (0.2081)	0.1538 (0.2817)	0.0117 (0.0016)	-0.0036 (0.0001)
$\nu_7(a_1)$	0.1879	0.0288 (0.0117)	0.0271 (0.0104)	-0.0049 (0.0003)	-0.0911 (0.1175)
$\nu_8(a_1)$	0.1519	-0.0489 (0.0517)	-0.1075 (0.2504)	0.0447 (0.0433)	0.0775 (0.1302)
$\nu_9(a_1)$	0.1475	0.0728 (0.1218)	-0.0543 (0.0677)	0.0318 (0.0232)	0.0173 (0.0069)
$\nu_{10}(a_1)$	0.1300	-0.0161 (0.0077)	-0.0464 (0.0636)	0.0275 (0.0223)	-0.0473 (0.0662)
$\nu_{11}(a_1)$	0.1251	-0.0470 (0.0706)	-0.0540 (0.0932)	-0.0421 (0.0566)	-0.0556 (0.0988)
$\nu_{12}(a_1)$	0.0954	-0.0420 (0.0969)	0.0302 (0.0501)	-0.0269 (0.0397)	-0.0713 (0.2793)
$\nu_{13}(a_1)$	0.0576	-0.0580 (0.5070)	0.0647 (0.6309)	-0.0266 (0.1066)	-0.0014 (0.0003)
$E^0_{B_1}$	8.5079				
$E^0_{A_2}$	9.1548				
$E^0_{B_2}$	9.9821				
$E^0_{B_1}$	10.7509				

Table 4.3: The second-order coupling parameters (γ_i) (in eV) for the $\widetilde{X}^2B_1$, $\widetilde{A}^2A_2$, $\widetilde{B}^2B_2$ and $\widetilde{C}^2B_1$ electronic states of the PA$^+$ derived from the *ab initio* electronic structure data.

modes (symmetry)	frequency (eV)	$\gamma^{(X)}$ $\widetilde{X}^2B_1$	$\gamma^{(A)}$ $\widetilde{A}^2A_2$	$\gamma^{(B)}$ $\widetilde{B}^2B_2$	$\gamma^{(C)}$ $\widetilde{C}^2B_1$
$\nu_1(a_1)$	0.4332	0.0010	0.0012	0.0010	0.0010
$\nu_2(a_1)$	0.4026	0.0034	0.0038	0.0016	0.0024
$\nu_3(a_1)$	0.4010	0.0042	0.0044	0.0020	0.0030
$\nu_4(a_1)$	0.3987	0.0054	0.0058	0.0036	0.0048
$\nu_5(a_1)$	0.2631	-0.0194	0.0002	0.0074	0.0282
$\nu_6(a_1)$	0.2049	-0.0056	0.0104	-0.0146	0.0046
$\nu_7(a_1)$	0.1879	-0.0052	0.0030	-0.0104	0.0016
$\nu_8(a_1)$	0.1519	-0.0046	0.0052	-0.0120	-0.0116
$\nu_9(a_1)$	0.1475	0.0044	0.0056	0.0054	0.0054
$\nu_{10}(a_1)$	0.1300	0.0018	-0.0028	0.0014	-0.0022
$\nu_{11}(a_1)$	0.1251	0.0006	-0.0010	-0.0024	-0.0004
$\nu_{12}(a_1)$	0.0954	-0.0024	-0.0006	-0.0038	-0.0022
$\nu_{13}(a_1)$	0.0576	-0.0042	0.0004	-0.0044	-0.0010
$\nu_{14}(a_2)$	0.1181	0.0090	0.0076	0.0020	-0.0078
$\nu_{15}(a_2)$	0.1052	-0.0080	0.0070	-0.0018	-0.0088
$\nu_{16}(a_2)$	0.0493	-0.0100	-0.0332	-0.0026	-0.0106
$\nu_{17}(b_1)$	0.1186	0.0040	-0.0108	0.0100	-0.0168
$\nu_{18}(b_1)$	0.1119	0.0152	-0.0188	0.0074	-0.0054
$\nu_{19}(b_1)$	0.0919	0.0024	-0.0034	0.0052	-0.0026
$\nu_{20}(b_1)$	0.0789	-0.0062	-0.0184	-0.0100	-0.0166
$\nu_{21}(b_1)$	0.0722	0.0086	0.0080	-0.0304	-0.0168
$\nu_{22}(b_1)$	0.0608	0.0016	-0.0074	-0.0136	-0.0110
$\nu_{23}(b_1)$	0.0426	-0.0168	-0.0098	-0.0248	-0.0194
$\nu_{24}(b_1)$	0.0170	-0.0128	-0.0144	-0.0400	-0.0294
$\nu_{25}(b_2)$	0.4018	0.0032	0.0046	0.0016	0.0024
$\nu_{26}(b_2)$	0.3998	0.0048	0.0054	0.0026	0.0038
$\nu_{27}(b_2)$	0.2016	-0.0430	0.0438	-0.0058	0.0152
$\nu_{28}(b_2)$	0.1840	0.0132	0.0388	-0.0034	0.0168
$\nu_{29}(b_2)$	0.1797	0.0272	0.0142	-0.0018	0.0130
$\nu_{30}(b_2)$	0.1638	0.0026	0.0058	0.0034	0.0042
$\nu_{31}(b_2)$	0.1454	0.0024	0.0128	0.0040	0.0074
$\nu_{32}(b_2)$	0.1358	0.0008	-0.0020	0.0024	0.0070
$\nu_{33}(b_2)$	0.0773	-0.0120	0.0060	-0.0058	-0.0010
$\nu_{34}(b_2)$	0.0772	-0.0076	0.0080	0.0040	-0.0026
$\nu_{35}(b_2)$	0.0623	-0.0028	-0.0020	-0.0054	-0.0164
$\nu_{36}(b_2)$	0.0182	-0.0222	-0.0028	-0.0624	-0.0390

Table 4.4: The linear interstate coupling parameters (λ_i) (in eV) of PA$^+$. The dimensionless coupling strengths, $\lambda^2/2\omega^2$, are given in parentheses.

modes (symmetry)	λ^{X-A} $\widetilde{X}^2B_1$ - $\widetilde{A}^2A_2$	λ^{X-B} $\widetilde{X}^2B_1$ - $\widetilde{B}^2B_2$	λ^{A-B} $\widetilde{A}^2A_2$ - $\widetilde{B}^2B_2$	λ^{A-C} $\widetilde{A}^2A_2$ - $\widetilde{C}^2B_1$	λ^{B-C} $\widetilde{B}^2B_2$ - $\widetilde{C}^2B_1$
$\nu_{25}(b_2)$	0.0150 (0.0007)	-	-	-	-
$\nu_{26}(b_2)$	0.0107 (0.0003)	-	-	-	-
$\nu_{27}(b_2)$	0.1228 (0.1855)	-	-	-	-
$\nu_{28}(b_2)$	0.0644 (0.0613)	-	-	-	-
$\nu_{29}(b_2)$	-	-	-	-	-
$\nu_{30}(b_2)$	0.0223 (0.0093)	-	-	-	-
$\nu_{31}(b_2)$	0.0403 (0.0384)	-	-	-	-
$\nu_{32}(b_2)$	-	-	-	0.0589 (0.0941)	-
$\nu_{33}(b_2)$	0.0542 (0.2458)	-	-	-	-
$\nu_{34}(b_2)$	0.0501 (0.2106)	-	-	-	-
$\nu_{35}(b_2)$	0.0092 (0.0109)	-	-	-	-
$\nu_{36}(b_2)$	0.0557 (4.6831)	-	-	-	-
$\nu_{14}(a_2)$	-	-	-	-	-
$\nu_{15}(a_2)$	-	0.0486 (0.1067)	-	-	-
$\nu_{16}(a_2)$	-	0.0529 (0.5757)	-	-	-
$\nu_{17}(b_1)$	-	-	0.0699 (0.1737)	-	-
$\nu_{18}(b_1)$	-	-	0.0745 (0.2216)	-	-
$\nu_{19}(b_1)$	-	-	0.0435 (0.1120)	-	-
$\nu_{20}(b_1)$	-	-	0.0430 (0.1485)	-	-
$\nu_{21}(b_1)$	-	-	-	-	-
$\nu_{22}(b_1)$	-	-	-	-	-
$\nu_{23}(b_1)$	-	-	-	-	-
$\nu_{24}(b_1)$	-	-	-	-	-

potential energy hypersurface of PA$^+$ along totally symmetric vibrational modes (ν_1-ν_{13}) are shown in Fig. 4.1. The $\widetilde{X}$-$\widetilde{A}$ states crossings can be seen along the ν_{13}, ν_9, ν_6 and ν_5. Similarly, the $\widetilde{A}$-$\widetilde{B}$ states crossings can be seen along ν_8 and ν_5. A magnified view of the low-energy crossings of the $\widetilde{X}$-$\widetilde{A}$ and $\widetilde{A}$-$\widetilde{B}$ states along the ν_5 (acetylenic C≡C stretching) and ν_6 (C=C stretching of the benzene ring) vibrational modes is shown in Fig. 4.2. These curve crossings would lead to the formation of multidimensional CIs when distorted along the nontotally symmetric vibrational modes. Within the linear coupling scheme the energetic minimum [22] of the seam of the $\widetilde{X}$-$\widetilde{A}$, $\widetilde{A}$-$\widetilde{B}$ and $\widetilde{B}$-$\widetilde{C}$ CIs is estimated to occur at ≈ 9.01 eV, ≈ 9.83 eV and ≈ 11.69 eV respectively. This minimum for the $\widetilde{X}$-$\widetilde{A}$ surfaces occurs ≈ 0.02 eV above the equilibrium minimum of the $\widetilde{A}$ electronic state. The vibrational structure of the $\widetilde{A}$ state is therefore expected to be strongly perturbed by the associated nonadiabatic interactions. The minimum of the $\widetilde{A}$-$\widetilde{B}$ CIs occurs at ≈ 0.95 eV and ≈ 0.06 eV above the minimum of the $\widetilde{A}$ and $\widetilde{B}$ electronic states, respectively. The minimum of the $\widetilde{B}$-$\widetilde{C}$ CIs occurs at ≈ 1.06 eV above the global minimum of the $\widetilde{C}$ state. The minimum of the $\widetilde{X}$-$\widetilde{B}$ CIs occurs at ≈ 12.23 eV, which is ≈ 2.5 eV above the equilibrium minimum of the $\widetilde{B}$ state. The $\widetilde{X}$ and $\widetilde{C}$ CIs occur at much higher energy and are not considered here.

A careful examination of the linear coupling parameters and the excitation strengths of all 36 vibrational modes given in Table 4.2 and 4.4 reveals the importance of 9 a_1 (ν_{13}-ν_5), 9 b_1 (ν_{36}-ν_{27}), 2 a_2 (ν_{16} and ν_{15}) and 4 b_1 (ν_{20}-ν_{17}) vibrational modes in the coupled state dynamics of the $\widetilde{X}$-$\widetilde{A}$-$\widetilde{B}$-$\widetilde{C}$ electronic states of PA$^+$.

4.3.2 Electronic spectra

As stated in the introduction, the complex vibronic bands in the energy range of the $\widetilde{X}$, $\widetilde{A}$, $\widetilde{B}$ and $\widetilde{C}$ electronic states of PA$^+$ are recorded in the PE spectroscopy experiment [125]. The vibrational level structures of the $\widetilde{X}$ electronic state is recorded in a MATI [130] and that of the $\widetilde{C}$ state in PIRI [131] spectroscopy
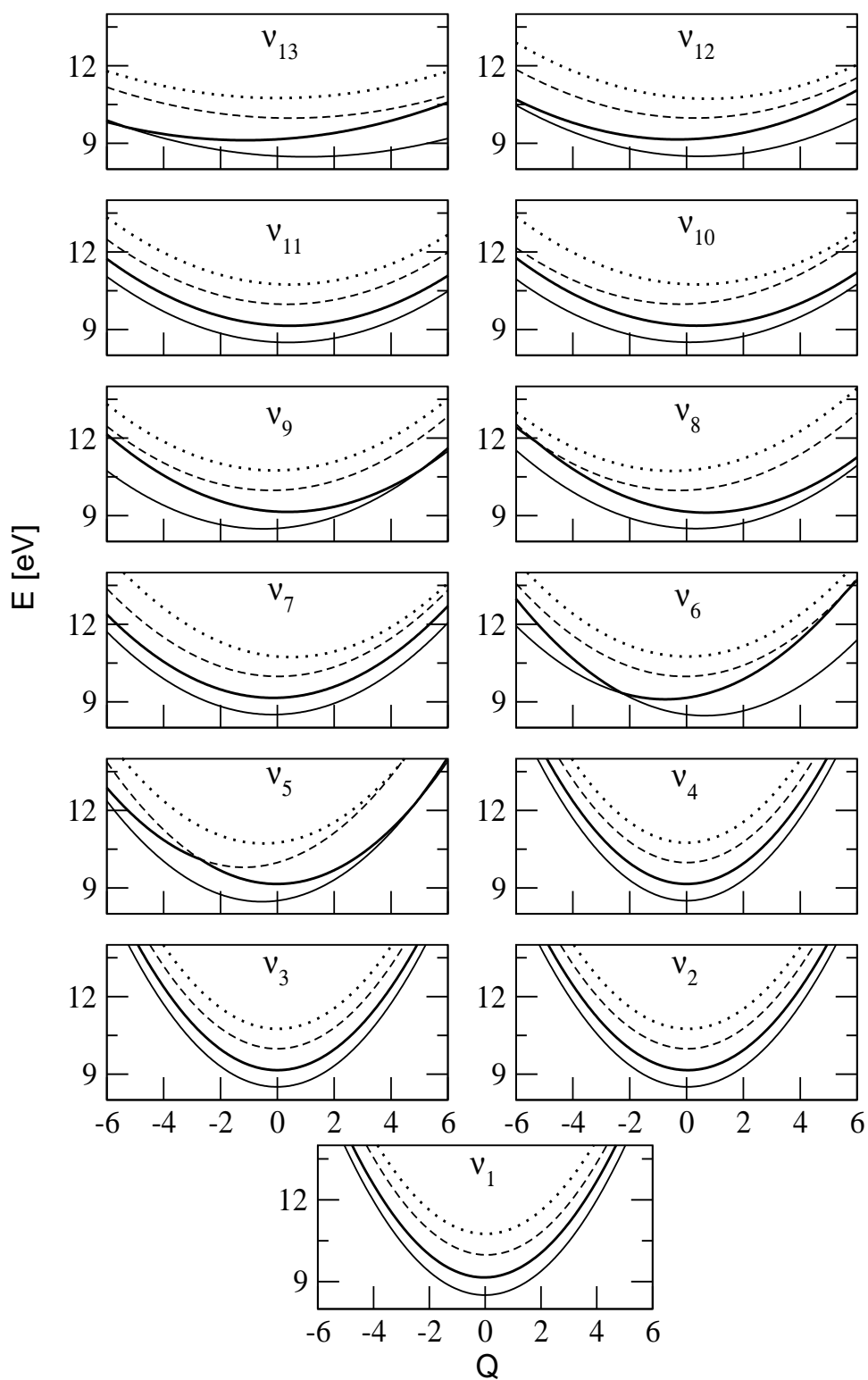
Figure 4.1: Adiabatic potential energies of the $\widetilde{X}$ (thin line), $\widetilde{A}$ (thick line), $\widetilde{B}$ (dashed line) and $\widetilde{C}$ (dotted line) electronic states of PA$^+$ as a function of the dimensionless normal coordinates of the totally symmetric (a_1) vibrational modes, ν_1-ν_{13}.
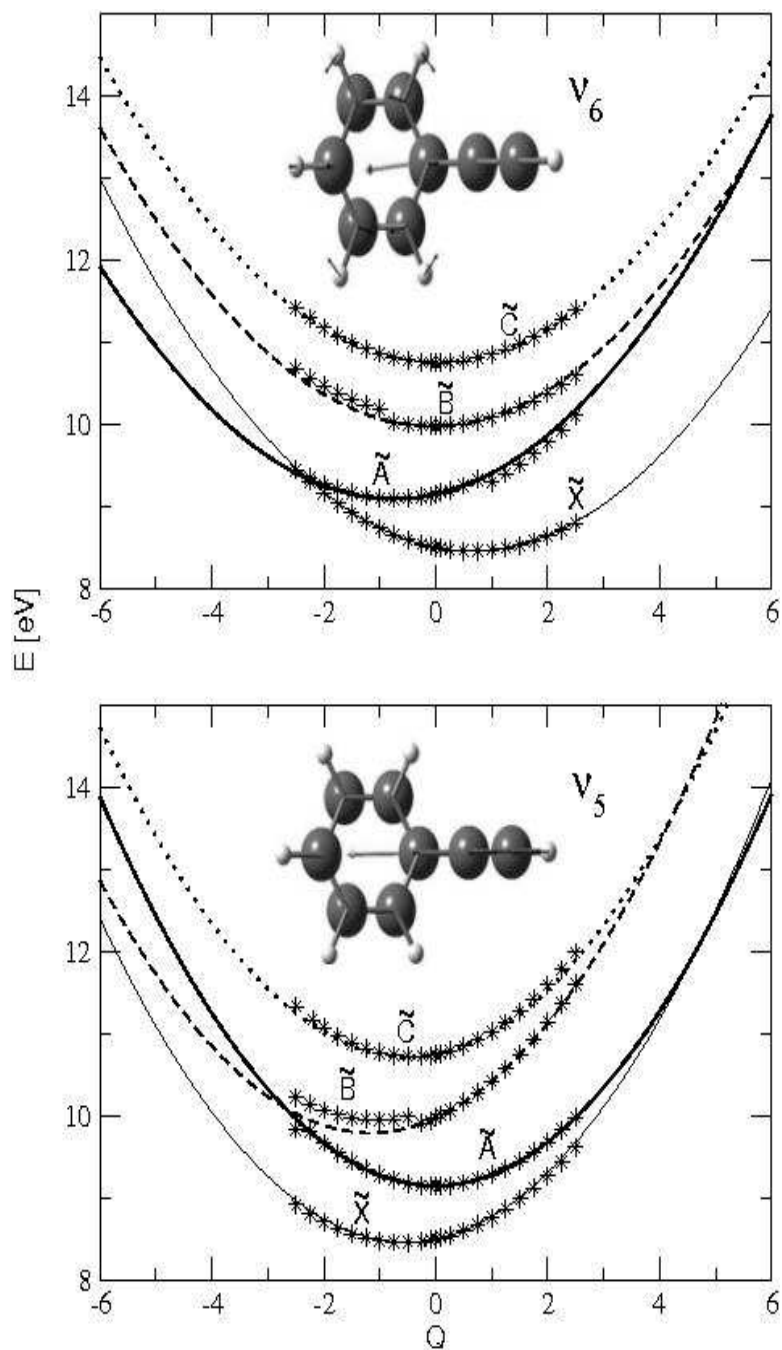
Figure 4.2: Adiabatic potential energies of the $\widetilde{X}$, $\widetilde{A}$, $\widetilde{B}$ and $\widetilde{C}$ electronic states of PA$^+$ along the vibrational modes ν_6 and ν_5. A sketch of the vibrational mode is also shown in the respective panel. The potential energy surfaces are obtained with the quadratic vibronic coupling scheme. The computed *ab initio* potential energies of these states are superimposed and shown by the asterisks on each curve. The equilibrium geometry of PA in its electronic ground state ($\widetilde{X}^1A_1$) corresponds to $\mathbf{Q} = 0$.

experiment at improved energy resolution. In the following, we first focus on the PE spectroscopy results and show and compare the theoretical results obtained at lower energy resolution using the full vibronic Hamiltonian of Eqs. 4.1(a-e) with 24 relevant vibrational modes listed above. The results at a higher energy resolution are considered next to compare with the observed MATI and PIRI spectroscopy data.

In Fig. 4.3, theoretical results obtained for the coupled $\widetilde{X}$-$\widetilde{A}$-$\widetilde{B}$-$\widetilde{C}$ electronic states are shown in the bottom panel along with the experimental PE spectroscopy results [125] in the top panel. The relative intensity in arbitrary units is plotted as a function of the energy of the final vibronic states. The theoretical results are obtained using the *ab initio* parameters of the Hamiltonian given in Table 4.2-4.4 without any adjustments. The quantum dynamical simulations are carried out by propagating WPs using the MCTDH algorithm [109]. Understandably, the large dimensionality of the problem and huge requirements of computer hardware makes the matrix diagonalization approach impracticable in this case. The details of the basis set and mode combinations employed in the WP propagations using the MCTDH algorithm are given Table 4.5. Four separate WP calculations are carried out with four different choices of initial states of PA^+ and finally the results are combined to obtain the composite vibronic band presented in Fig. 4.3. In each WP propagation the time autocorrelation function is calculated upto a total time of 300 fs. The combined autocorrelation function is finally damped with an exponential function, e^{-t/τ_r} (with $\tau_r = 66$ fs), before Fourier transformation to generate the spectrum of Fig. 4.3. This damping corresponds to a convolution of the vibronic lines with a Lorentzian function of 20 meV full width at the half maximum (FWHM). An energy shift of 0.98 eV is applied along the abscissa to reproduce the experimental adiabatic ionization position of the $\widetilde{X}$ state at ~ 8.83 eV [125].

Despite very minor differences in the finer details, the theoretical results of Fig. 4.3 are in excellent accord with the experiment and reveal resolved vibronic
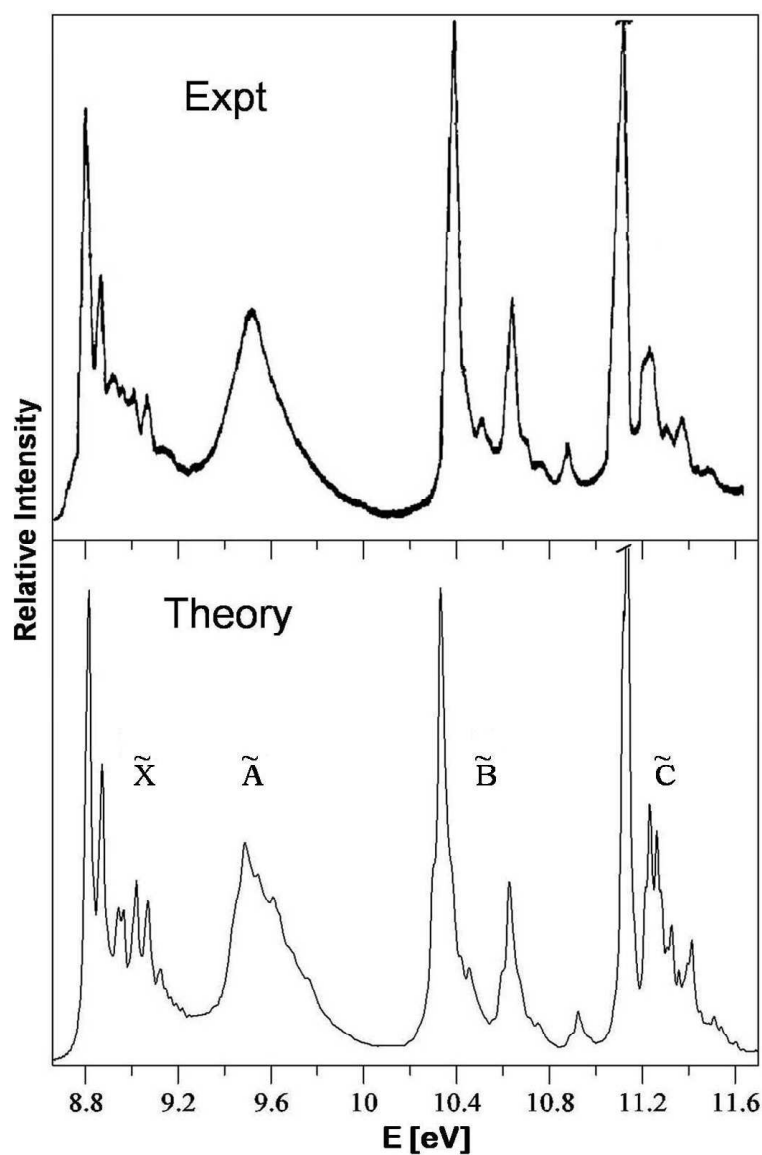
Figure 4.3: The PE spectrum of the coupled $\widetilde{X}$-$\widetilde{A}$-$\widetilde{B}$-$\widetilde{C}$ electronic states of PA$^+$. The experimental (reproduced from Ref [125]) and the present theoretical results are shown in the top and bottom panels, respectively. The intensity (in arbitrary units) is plotted along the energy (measured relative to electronic ground state of PA) of the final vibronic states. An energy offset of ~ 0.98 eV to the theoretical results is applied along the abscissa to reproduce the experimental adiabatic ionization energy of the $\widetilde{X}$ band.

Table 4.5: Normal mode combinations, sizes of the primitive and single particle bases used in the MCTDH calculations for the coupled $\widetilde{X}$-$\widetilde{A}$-$\widetilde{B}$-$\widetilde{C}$ electronic states of PA$^+$.

Normal modes	Primitive basis [a]	SPF basis [b] $[\widetilde{X}, \widetilde{A}, \widetilde{B}, \widetilde{C}]$
$(\nu_{11}, \nu_8, \nu_{17}, \nu_{27})$	(4, 5, 5, 6)	[8, 7, 8, 5]
$(\nu_{18}, \nu_{10}, \nu_{28}, \nu_{32})$	(4, 5, 4, 4)	[6, 8, 6, 7]
$(\nu_{16}, \nu_6, \nu_{34}, \nu_{12})$	(5, 4, 6, 5)	[8, 6, 5, 6]
$(\nu_{19}, \nu_{35}, \nu_{30}, \nu_{20})$	(5, 5, 4, 4)	[6, 7, 9, 5]
$(\nu_{36}, \nu_5, \nu_{33}, \nu_{31})$	(8, 20, 5, 4)	[9, 6, 5, 8]
$(\nu_{13}, \nu_9, \nu_{15}, \nu_7)$	(5, 5, 5, 5)	[6, 5, 6, 7]

The calculations were converged with respect to the spectrum. [a] The primitive basis is the number of Harmonic oscillator DVR functions, in the dimensionless coordinate system required to represent the system dynamics along the relevant mode. The primitive basis for each particle is the product of the one-dimensional bases; e.g for particle 1 in the set given for Fig. 4.3 the primitive basis contains $4 \times 5 \times 5 \times 6 = 600$ functions and the full primitive basis consists of a total of 9.216×10^{16} functions. [b] The SPF basis is the number of single-particle functions used.

structure of the $\widetilde{X}$, $\widetilde{B}$ and $\widetilde{C}$ states and an extremely broad and diffuse vibronic band of the $\widetilde{A}$ state. Nonadiabatic coupling among the four electronic states leads to the complex vibrational structures of the bands in Fig. 4.3. Apart from a few dominant progressions, it is difficult to decipher the entire vibrational level structure from the theoretical results of Fig. 4.3. The $\widetilde{X}$ and $\widetilde{A}$ states are strongly coupled (cf. Table 4.4), particularly through the vibrational mode ν_{36} (15). This is a low-frequency mode of b_2 type and causes strong mixing of the $\widetilde{X}$ and $\widetilde{A}$ states. As the energetic minimum of the $\widetilde{X}$-$\widetilde{A}$ CIs occurs at $\approx$ 9.01 eV, the low-energy vibrational structures of the $\widetilde{X}$ state are not much affected by this strong nonadiabatic mixing. The vibrational structures of the $\widetilde{A}$ state, on the other hand, is strongly perturbed starting from its onset, as the minimum of the $\widetilde{X}$-$\widetilde{A}$ CIs occurs below the zero-point energy level of the $\widetilde{A}$ state. Furthermore, the latter state is also coupled moderately with the $\widetilde{B}$ and weakly with the $\widetilde{C}$ state through the vibrational modes of b_1 and b_2 symmetry, respectively (cf., Table 4.4). However, the impact of the $\widetilde{A}$-$\widetilde{B}$ and $\widetilde{A}$-$\widetilde{C}$ CIs on its vibronic structure is much less compared to that of $\widetilde{X}$-$\widetilde{A}$ CIs. The $\widetilde{X}$ state is also coupled with the

$\widetilde{B}$ state through the vibrational modes of a_2 symmetry. Reduced dimensional calculations and a systematic analysis of the results enable us to make a few remarks here. The low-lying vibrational structure of the $\widetilde{X}$ state is unaffected by the nonadiabatic coupling. The effect of the latter seems to be the strongest in the vibrational structure of the $\widetilde{A}$ state. The low-lying vibrational structure of the $\widetilde{B}$ band is affected by the $\widetilde{X}$-$\widetilde{B}$ and $\widetilde{A}$-$\widetilde{B}$ CIs. The $\widetilde{C}$ state is found to be only weakly coupled with the $\widetilde{A}$ state through the b_2 vibrational mode, ν_{32} (18b) and therefore this coupling does not have any noticeable impact on its vibrational structure.

The dominant progressions in the $\widetilde{X}$ band is found to be caused by the vibrational mode ν_{13} (6a). A long progression of this mode due to several overtone transitions is found. The peaks are ~ 429 cm^{-1} apart corresponding to the frequency of this mode. This result is in accord with the PE spectroscopy data, which reveal a slightly higher value of ~ 489 cm^{-1}. A value of ~ 460 cm^{-1} has been reported for this progression in the threshold photoelectron spectroscopy measurements [135]. It is attributed to one of the bending mode in the experiment [125]. However, Table 4.1 shows that this vibration is of stretching type. Short progressions of ~ 1204 cm^{-1} and ~ 1147 cm^{-1} due to ν_8 (13) and ν_9 (9a) vibrational modes, respectively, are also found from the theoretical results. Apart from these, several combination levels of ν_{13} with ν_8 and ν_9 vibrational modes are also found from the theoretical data. Further discussions on the vibrational structure of the $\widetilde{X}$ band is considered below in relation to the observed MATI results.

An extended progression of ~ 467 cm^{-1} due to ν_{13} mode is also observed in the $\widetilde{A}$ state. The vibrational modes ν_8 (13) and ν_6 (8a) are also excited in the $\widetilde{A}$ band. Peak spacings of ~ 1267 cm^{-1} and ~ 1734 cm^{-1} are attributed to their progressions, respectively. Apart from these, the densely packed vibronic levels of the $\widetilde{A}$ state could not be assigned further. The increase in the vibronic level density is caused by a strong mixing of this state with the $\widetilde{X}$ and $\widetilde{B}$ states as

discussed above. The progressions in the $\widetilde{B}$ state is primarily caused by ν_{13} (6a), ν_5 (μ_{CC}) and ν_8 vibrational modes. Peak spacings of ~ 427 cm^{-1}, ~ 2180 cm^{-1} and ~ 1170 cm^{-1} are attributed to these progressions, respectively. Progressions of ~ 484 cm^{-1} (due to ν_{13}) and ~ 2050 cm^{-1} (due to ν_5) are extracted from the PE spectrum [125]. The latter is predominantly acetylenic C$\equiv$C stretching vibration and is strongly excited in the $\widetilde{B}$ state. This indicates that the $\widetilde{B}$ state originates from a MO mainly localized on the acetylenic moiety, on par with the nature of the HOMO-2 plotted in Fig. 4.7.

The vibrational structure of the $\widetilde{C}$ state is formed by many low frequency vibrational modes. Among the symmetric vibrational modes ν_{12}, ν_{11}, ν_{10}, ν_7 and ν_5 are excited. In contrast to the $\widetilde{X}$, $\widetilde{A}$ and $\widetilde{B}$ electronic states the vibrational mode ν_{13} is very weakly excited in the $\widetilde{C}$ state. While the overall structure of the $\widetilde{C}$ band reveals very good agreement with the experiment in Fig. 4.3, the finer details show some discrepancies when compared with the PIRI spectrum recorded by Xu *et al.* [131]. These authors have reported the vibrational energy level structure of the $\widetilde{C}$ state upto an energy of ~ 2200 cm^{-1} above its origin at ~ 17834 cm^{-1}. The dominant progressions in the spectrum are reported to be formed by the totally symmetric vibrational modes. In addition, weak excitations of the overtones and combinations of the nontotally symmetric modes are also assigned in the experiment.

In order to corroborate to these experimental results, we performed reduced dimensional calculations of the vibrational energy levels of the $\widetilde{C}$ state employing the matrix diagonalization approach within the capability of the computer hardware. These calculations are performed both for the uncoupled and coupled state situations in order to obtain the precise locations of the vibrational levels to be compared with the experiment. The present electronic structure data reveal a weak coupling of the $\widetilde{C}$ state with the $\widetilde{A}$ state via the vibrational mode ν_{32} (18b). Apart from this the $\widetilde{C}$ state is not found to have any coupling with the other states in the set of electronic states considered here. Therefore, the dynamical

simulations are carried out by retaining the $\widetilde{A}$-$\widetilde{C}$ coupling and considering the vibrational modes [six a_1 (ν_{13}-ν_{10}, ν_7 and ν_5), three b_1 (ν_{36}, ν_{35} and ν_{32}) and three b_2 (ν_{24}, ν_{23} and ν_{21})] assigned to the observed lines in the PIRI spectrum [131]. Again we note that, with these 12 vibrational modes and two electronic states, calculations become computationally intensive and seem not well converged. We, therefore, also carried out various two states and single state calculations by reducing number of vibrational modes to confirm the location of a given vibrational level in the spectrum.

In the experimental spectrum the mode 6a (ν_{13} in our list) is found to be strongly excited at $\sim$ 448 cm^{-1} and transition upto its third overtone level has been reported [131]. In contrast, we find only weak excitation of its fundamental at $\sim$ 456 cm^{-1} (also apparent from its excitation strength given in Table 4.2) and its first overtone is hardly observed at $\sim$ 913 cm^{-1}. The weak excitation of ν_{13} is in agreement with the laser photodissociation spectroscopy results of Pino *et al.* [132], who reported its fundamental at $\sim$ 452 cm^{-1}. We find the mode ν_{12} (12 in the Wilson's notation) is strongly excited in the theoretical spectrum. Intensity of ν_{13} fundamental is about a factor of 10^3 less than that of the ν_{12}. The excitation upto the second overtone level of the latter mode is found from the theoretical data. The fundamental of ν_{12} is found at $\sim$ 751 cm^{-1} as compared to its experimental value of $\sim$ 939 cm^{-1} [131]. We mention, that the Wilson's and Herzberg's notations are interchanged for this mode in different articles. We believe that 12 of Ref. [131] corresponds to the mode ν_{11} in our list. If this is the case, then excitation of the mode ν_{12} is not observed at all in the experiment [131]. Apart from the modes ν_{13} and ν_{12}, fundamentals of ν_{11} at $\sim$ 1028 cm^{-1}, ν_{10} at $\sim$ 1046 cm^{-1}, ν_8 at $\sim$ 1232 cm^{-1}, ν_7 at $\sim$ 1528 cm^{-1} and ν_5 at 2280 cm^{-1} are found from the theoretical data. The fundamentals of 18a (ν_{10}), 13 (ν_8) and 19a (ν_7) are observed at $\sim$ 996 cm^{-1}, $\sim$ 1147 cm^{-1} and $\sim$ 1467 cm^{-1}, respectively, in the experimental spectrum [131]. The fundamentals of ν_9 and ν_6 appear with much lower intensity at $\sim$ 1207 cm^{-1} and $\sim$ 1689 cm^{-1}, respectively, to be compared

with their experimental value of ~ 1116 cm^{-1} (1118 cm^{-1} in Ref. [132]) and $\sim$ 1546 cm^{-1} (1561 cm^{-1} in Ref. [132]), respectively. However, we are not very comfortable with the latter two transitions as the observed intensities are very small on par with their excitation strengths given in the Table 4.2. Excitations of combinations $\nu_{12}^1\nu_{13}^1$, $\nu_{12}^1\nu_{11}^1$, $\nu_{12}^1\nu_{10}^1$, $\nu_{12}^1\nu_8^1$ and $\nu_{13}^1\nu_{11}^1$, $\nu_{13}^1\nu_{10}^1$ at ~ 1212 cm^{-1}, ~ 1759 cm^{-1}, ~ 1783 cm^{-1}, ~ 1988 cm^{-1}, ~ 1463 cm^{-1} and ~ 1488 cm^{-1}, respectively is also revealed by the theoretical data. Excitations at ~ 2074 cm^{-1}, ~ 2258 cm^{-1} and ~ 2577 cm^{-1} are attributed to $\nu_{10}^1\nu_{11}^1$, ν_{12}^3 and $\nu_7^1\nu_{10}^1$, respectively. Weak lines at ~ 2075 cm^{-1}, ~ 2241 cm^{-1} and ~ 2577 cm^{-1} are also reported in the photodissociation spectrum of PA$^+$ [132]. As regard to the nontotally symmetric modes, the $\widetilde{A}$-$\widetilde{C}$ vibronic coupling does not induce their noticeable excitations in the $\widetilde{C}$ state. The minimum of the seam of CIs of the $\widetilde{A}$ and $\widetilde{C}$ states occur at ~ 8500 cm^{-1} above the equilibrium minimum of the $\widetilde{C}$ state, therefore the low-lying vibronic levels of the $\widetilde{C}$ state are not found to be affected by this vibronic coupling. Comparison calculations with and without the b_1 and b_2 vibrational modes also support these findings.

It is worthwhile to make a few remarks here. The theoretical results obtained with the complete model of four coupled electronic states and 24 vibrational modes exhibit excellent agreement with the broad band PE spectroscopy results. For comparison with the high resolution PIRI spectrum of the $\widetilde{C}$ state appropriate reduced dimensional models had to be constructed to be able to simulate the dynamics by the computationally intensive matrix diagonalization approach. Analysis of the results from various models enabled us to compare the dominant excitations of the totally symmetric vibrational modes with the experiment. The weak excitations of the nontotally symmetric modes reported in the experiment are however not revealed by the theoretical results. The discrepancies may be attributed to a difference in the initial state considered in the theory (neutral ground state) and experiment (ion core of the Rydberg state) and possible coupling of the $\widetilde{C}$ state with the other high-lying excited electronic states of PA$^+$.

The quality of the *ab initio* electronic structure data may also be refined further to reproduce the high resolution experiment quantitatively. Work along these lines are presently in progress.

4.3.3 The MATI spectrum of the $\widetilde{X}^2B_1$ state

Kwon *et al.* have recorded one photon MATI spectrum of the $\widetilde{X}$ state by directly exciting PA to a Rydberg state using vacuum ultraviolet radiation [130]. This one photon measurement avoids the excitation to an intermediate state as in a two photon measurement and yields better intensity. We note that, the theoretical calculations reported here directly probe the cationic states, and does not go through the Rydberg electronic state. Therefore, we do not expect to reproduce the intensities so as to compare with the experiment. This is also the case with the PIRI spectroscopy results discussed above. The line positions are therefore directly compared with the experimental data. The relative intensities are shown to be comparable with the PE spectroscopy data in Fig. 4.3 within the Condon approximation. Furthermore, the results shown in this section are obtained by the matrix diagonalization method, so as to accurately calculate the position of the vibronic levels. Therefore, huge computational overheads prohibit to perform a full dimensional calculation and we resort to various reduced dimensional models to compare the results with the experiment.

From the foregoing discussions it is clear that the $\widetilde{X}$-$\widetilde{A}$ CIs play some role in the high energy tail of the $\widetilde{X}$ band. The MATI spectrum extends upto an energy of ~ 74500 cm^{-1}, which is about 2100 cm^{-1} below the minimum of the seam of the $\widetilde{X}$-$\widetilde{A}$ CIs. Therefore, only weak excitations of the nontotally symmetric modes are to be expected in the recorded energy range of the MATI spectrum. Because of vibronic mixing of the $\widetilde{X}$ and $\widetilde{A}$ electronic states, both the fundamentals and overtones of these vibrational modes would show up in the spectrum.

In Fig. 4.4, the experimentally recorded MATI spectrum from Ref. [130] is
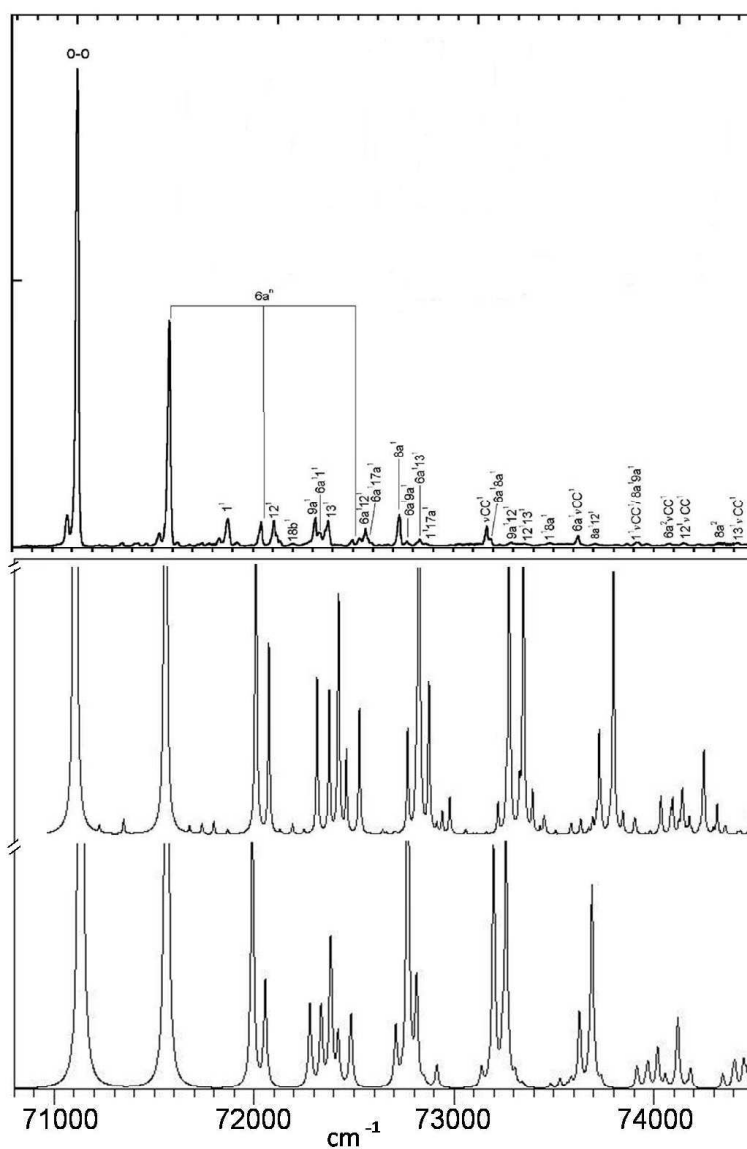
Figure 4.4: The MATI spectrum of the $\widetilde{X}$ state. The experimental spectrum (reproduced from Ref. [130] is shown in the top panel. In the bottom panel, the coupled $\widetilde{X}$-$\widetilde{A}$ spectrum (a) including 7 a_1 + 4 b_2 vibrational modes and also the uncoupled $\widetilde{X}$ state spectrum (b) including the 7 a_1 vibrational modes are shown.

plotted (top panel) along with the theoretically calculated coupled $\widetilde{X}$-$\widetilde{A}$ spectrum (a). The latter is obtained by including seven totally symmetric (ν_{13}-ν_{11}, ν_9, ν_8, ν_6 and ν_5) and four nontotally symmetric (ν_{36}, ν_{34}, ν_{33} and ν_{27}) vibrational modes. Among various reduced dimensional calculations, the above set yields result close to the experimental lines. The eleven vibrational modes above are selected based on their dominant linear coupling parameter (cf., Tables 4.2 and 4.4). At the bottom of the lower panel of Fig. 4.4 the uncoupled (without $\widetilde{X}$-$\widetilde{A}$ coupling) $\widetilde{X}$ band (b) obtained with the above set of vibrational modes is shown.

The calculated stick lines are convoluted with a 2 meV FWHM Lorentzian to obtain the spectral envelopes plotted in Fig. 4.4. The theoretical spectrum is shifted by $\sim$ 4027 cm^{-1} along the abscissa to reproduce the adiabatic ionization position of the band at $\sim$ 71133 cm^{-1}. A critical analysis reveals that the first peak at $\sim$ 115 cm^{-1} from the 0-0 line corresponds to the fundamental of the coupling vibrational mode ν_{36} (15) of b_2 symmetry. It is to be noted that this line appears at $\sim$ 110 cm^{-1} in the MATI spectrum and is attributed to the vibrational mode 10b of b_1 symmetry (ν_{24} in our list) [130]. The fundamentals of ν_{34} (6b), ν_{33} (β_{CH}) and ν_{27} (8b) are found at $\sim$ 602, $\sim$ 658 and $\sim$ 1624 cm^{-1} in accordance with their experimental locations at $\sim$ 561, $\sim$ 658 and $\sim$ 1505 cm^{-1}, respectively. Additional calculations are carried out considering the weak coupling b_2 vibrational modes ν_{35} (β_{CC}), ν_{31} (9b), ν_{30} (3) and ν_{28} (19b) along with the seven a_1 modes discussed above. Very weak lines at $\sim$ 1169, $\sim$ 1320 and $\sim$ 1480 cm^{-1} due to ν_{31}, ν_{30} and ν_{28}, respectively, are found from the theoretical data. The fundamentals of ν_{31} and ν_{30} are reported at $\sim$ 1158, $\sim$ 1287 cm^{-1}, respectively, in the MATI spectrum [130].

The most dominant excitations in the vibronic spectrum of Fig. 4.4 are due to the vibrational modes of a_1 symmetry. Nonadiabatic mixing with the $\widetilde{A}$ state leads to weak excitations of the vibrational modes of b_2 symmetry. This can be seen by comparing the two theoretical spectra shown in the middle and lower part of Fig. 4.4. Among the seven totally symmetric vibrational modes ν_{13} is strongly

excited at ~ 429 cm^{-1}. Strong excitation of this mode is also observed at ~ 458 cm^{-1} in the experiment [130]. Relatively weaker excitations of ν_{12}, ν_{11}, ν_9, ν_8, ν_6 and ν_5 fundamentals are found at ~ 788 (~ 759 cm^{-1} in Ref. [135]), ~ 1013, ~ 1147, ~ 1249, ~ 1628 and ~ 2055 cm^{-1}, respectively. These transitions are reported to occur at ~ 747, ~ 979, ~ 1185, ~ 1249, ~ 1604 and ~ 2040 cm^{-1}, respectively, from the MATI spectroscopy data. The nonadiabatic interaction mixes the vibronic levels at the high energy tail of the $\widetilde{X}$ band with those at the onset of the $\widetilde{A}$ band. The weak peaks in the spectrum at the middle, absent in the one at the bottom of Fig. 4.4, originate from this vibronic mixing.

Apart from the above fundamentals numerous weak lines appear in the spectrum of Fig. 4.4 due to overtones and combinations. For example, excitations upto the third overtone level is observed for ν_{36}. Lines at ~ 231 (230 in MATI), ~ 346 and ~ 464 cm^{-1} are assigned to $\nu_{36}{}^2$ and $\nu_{36}{}^3$ and $\nu_{36}{}^4$, respectively. Similarly, several overtone levels of the strongly excited ν_{13} are observed from the theoretical data. The weak shoulder peak reported at ~ 989 cm^{-1} [130] appears at ~ 970 cm^{-1} in the theoretical data and is assigned to a combination peak $\nu_{13}{}^2\nu_{36}$. With increasing energy the spectrum becomes congested due to an increase in the vibronic mixing. The bound levels become resonances which causes an increase of the line density as can be seen from the spectrum of Fig. 4.4. A clear and systematic assignment of the spectrum in the high energy region therefore becomes ambiguous and impossible.

The b_1 vibrational modes does not couple the $\widetilde{X}$ and $\widetilde{A}$ electronic states and only second order effects due to these modes are expected in the spectrum. Calculations are performed for the uncoupled $\widetilde{X}$ state including the above seven a_1 modes and the b_1 vibrational modes. We did not observe any noticeable excitations of the b_1 vibrational modes.

To this end, we reiterate that the results discussed above are obtained through a reduced dimensional treatment of the dynamics, therefore, the experimental and theoretical positions of the prominent peaks differ to some extent. Because

of the dimensionality problem the coupling of the $\widetilde{X}$ state with the others, apart from the $\widetilde{A}$ state, could not be considered. Furthermore, as stated before, the model PESs and nonadiabatic coupling surfaces developed here may would need further refinements in order to have a more quantitative agreement with the high-resolution experimental data, although an excellent agreement with the less resolved PE spectroscopy results is obtained with these surfaces.

4.3.4 On the life time of the excited electronic states of PA$^+$: time-dependent dynamics

In this section we show and discuss the time evolution of diabatic electronic population in the coupled states dynamics discussed in section 4.3.2. The time-dependent populations of the four diabatic electronic states are shown in each panel of Figs 4.5(a-d) and indicated by different line types. The results obtained by initially populating the $\widetilde{X}$, $\widetilde{A}$, $\widetilde{B}$ and $\widetilde{C}$ states in the WP dynamics are shown in the panels a-d, respectively. It can be seen from the Fig. 4.5(a) that the populations of all four states exhibit minor variations when the dynamics is initially started in the $\widetilde{X}$ state. Since the $\widetilde{X}$-$\widetilde{A}$ and $\widetilde{X}$-$\widetilde{B}$ CIs are located at higher energies (see the text above) they do not affect the short time dynamics of the $\widetilde{X}$ state. This leads to the observed sharp vibrational level structure of the $\widetilde{X}$ band. Despite this, minor transitions ($\sim < 0.1\%$ population) to the $\widetilde{A}$ state take place owing to a very strong $\widetilde{X}$-$\widetilde{A}$ coupling. This minor population flow triggers weak excitations of the nontotally symmetric vibrational modes in the high energy tail of the $\widetilde{X}$ band as clearly observed in the MATI spectrum of Fig. 4.4.

Profound effects of the strong $\widetilde{X}$-$\widetilde{A}$ coupling can be seen in the population dynamics of the $\widetilde{A}$ state shown in Fig. 4.5(b). As the minimum of the seam of $\widetilde{X}$-$\widetilde{A}$ CIs located only ≈ 0.02 eV above the equilibrium minimum of the $\widetilde{A}$ state, a rapid flow of the population to the $\widetilde{X}$ state takes place during the dynamics. The population of the $\widetilde{X}$ state reaches to ~ 90 % within ~ 100 fs. The rapid
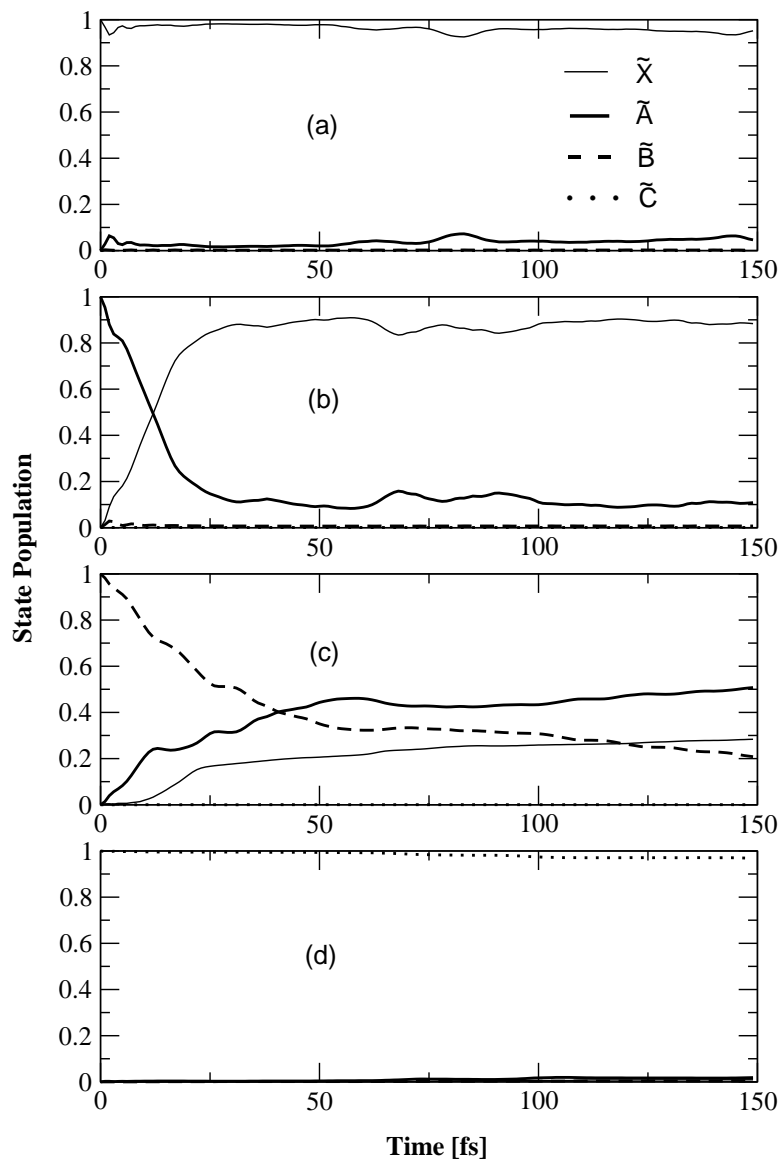
Figure 4.5: The time dependence of electronic (diabatic) populations of the $\widetilde{X}$ (thin lines), $\widetilde{A}$ (thick lines), $\widetilde{B}$ (dashed lines) and $\widetilde{C}$ (dotted lines) states of PA$^+$ for an initial transition of the WP to the $\widetilde{X}$ (panel a), $\widetilde{A}$ (panel b), $\widetilde{B}$ (panel c) and $\widetilde{C}$ (panel b) in the coupled $\widetilde{X}$-$\widetilde{A}$-$\widetilde{B}$-$\widetilde{C}$ states dynamical treatment of PA$^+$ discussed in section 4.3.2 in the text.

initial decay of the $\widetilde{A}$ state population relates to a nonradiative decay rate of ~ 20 fs. This also accounts for the photostability PA^+ excited to the $\widetilde{A}$ state and its possible contributions to the diffused interstellar bands. The broadening of the vibronic band of the $\widetilde{A}$ state mainly results from this rapid nonradiative decay. Similar findings are reported recently for the dynamics of electronically excited naphthalene radical cation [136]. The $\widetilde{A}$-$\widetilde{B}$ CIs do not seem to have much importance in the short time dynamics of the $\widetilde{A}$ state as indicated by a minor transfer of population to the $\widetilde{B}$ state (cf. Fig. 4.5(b)). Again, this is because the minimum of the seam of $\widetilde{A}$-$\widetilde{B}$ CIs occurs ≈ 0.95 eV above the equilibrium minimum of the $\widetilde{A}$ state.

For monosubstituted benzene cations the $\widetilde{B}$ state is generally predicted to be long lived. For most of these cations the $\widetilde{B}$ and $\widetilde{C}$ states are close in energy and they belong either to a $^2B_2$ or a $^2B_1$ representation depending on the nature of substitution. In PA^+ the $\widetilde{B}$ state is $^2B_2$ and the $\widetilde{C}$ state is of $^2B_1$ type. Youn *et al.* have carried out charge exchange ionization followed by mass spectroscopic measurements for the monosubstituted radical cations of benzene [129]. Narrow band width in the high resolution PE spectrum is used as a guideline to search for the long lived states in those measurements. By analyzing the signals due to fragment ions and their recombination energies, these authors have predicted $\widetilde{B}^2B_2$ as the long lived state of $C_6H_5Cl^{\bullet+}$, $C_6H_5Br^{\bullet+}$, $C_6H_5CN^{\bullet+}$ and PA^+ [129].

Long lived excited electronic state should be devoid of any efficient nonradiative decay channel. The electronic structure data of the $\widetilde{B}^2B_2$ state of PA^+ discussed above obviously show that this state is moderately coupled with the $\widetilde{A}$ and $\widetilde{X}$ states through the vibrational modes of b_1 and a_2 symmetry, respectively, (see, Table 4.4). The minimum of the seam of $\widetilde{X}$-$\widetilde{B}$ and $\widetilde{A}$-$\widetilde{B}$ CIs located at ≈ 2.5 eV and ≈ 0.06 eV above the equilibrium minimum of the $\widetilde{B}$ state, respectively. Therefore, the $\widetilde{A}$-$\widetilde{B}$ CIs indeed expected to impart considerable nonadiabatic effects in the vibronic dynamics of the $\widetilde{B}$ state of PA^+. A short detour to the $\widetilde{X}$-$\widetilde{B}$ and $\widetilde{A}$-$\widetilde{B}$ coupled state spectra presented in Figs. 4.5(a-b), respectively, support
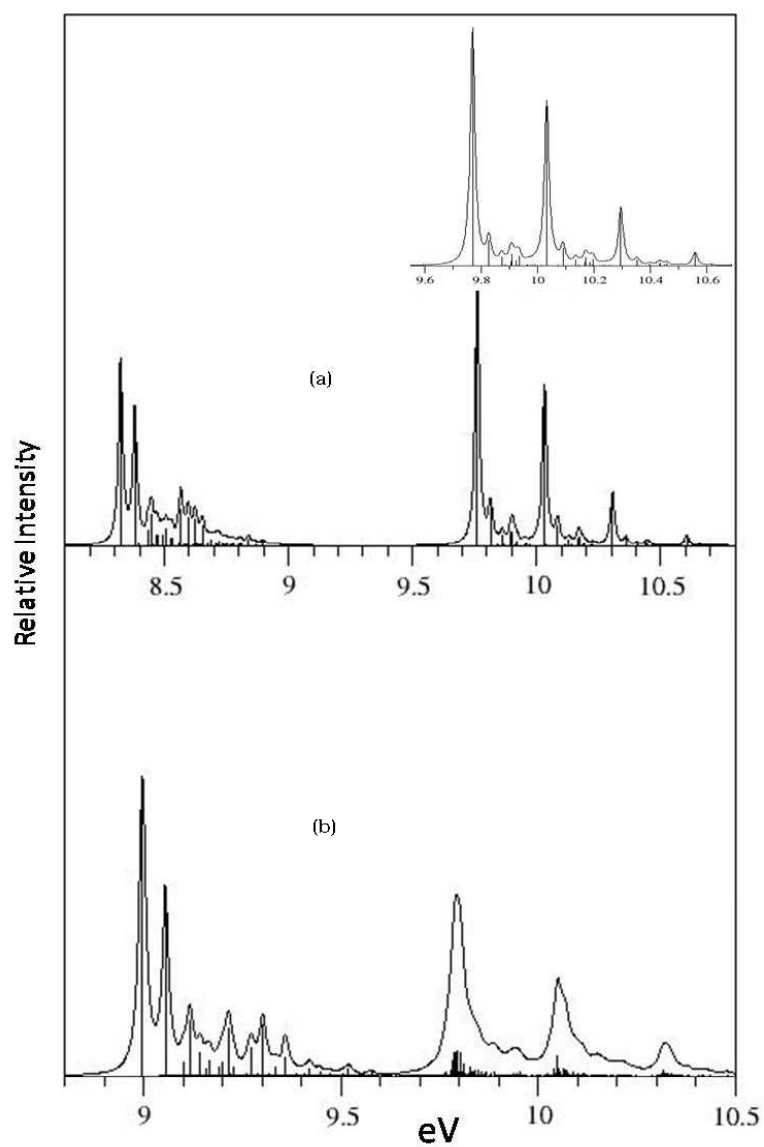
Figure 4.6: The vibronic spectra of the coupled $\widetilde{X}$-$\widetilde{B}$ (panel a) and $\widetilde{A}$-$\widetilde{B}$ (panel b) electronic states of PA$^+$. The vibrational energy level spectrum of the uncoupled $\widetilde{B}$ state is shown as an insert in panel a.

the above remarks. These spectra are obtained by the matrix diagonalization method and considering seven symmetric vibrational modes (ν_{13}-ν_{11}, ν_9, ν_8, ν_6 and ν_5) plus the coupling modes (ν_{16} and ν_{15}) for the $\widetilde{X}$-$\widetilde{B}$ spectrum (panel a) and (ν_{20}-ν_{17}) for the $\widetilde{A}$-$\widetilde{B}$ spectrum (panel b). It can be seen that the $\widetilde{X}$-$\widetilde{B}$ coupling has only minor effects on the vibronic structure of the $\widetilde{B}$ band, whereas, the latter is significantly affected starting from its onset by the $\widetilde{A}$-$\widetilde{B}$ coupling. Notice, the clustering of the lines around the origin peak of the $\widetilde{B}$ band in Fig. 4.6(b). The uncoupled $\widetilde{B}$ state spectrum is also included in panel a for a better comparison. Broadening of the vibrational peaks of the $\widetilde{B}$ band is also in accord with the PE spectroscopy results of Fig. 4.3. Reverting back to the population dynamics of Fig. 4.5, it can be seen from the panel c that the $\widetilde{B}$ state population decreases in time and reaches to a value of 20 % at 150 fs. Both the populations of the $\widetilde{A}$ and $\widetilde{X}$ state grows in time and the growth rate is in accord with the estimated impact of the $\widetilde{A}$-$\widetilde{B}$ and $\widetilde{X}$-$\widetilde{B}$ CIs on the nuclear dynamics of the $\widetilde{B}$ state. The initial decay of the $\widetilde{B}$ state population relates to a nonradiative decay rate of ~ 88 fs of this state. Collecting all the evidences given above, it appears that the $\widetilde{B}^2B_2$ state of PA$^+$ is not a very long lived state which deviates from the experimental prediction [129]. A sub-picosecond lifetime of the $\widetilde{B}^2B_2$ state of $C_6H_5F^+$ has also been reported recently [137].

The population dynamics of the $\widetilde{C}^2B_1$ state of PA$^+$ is shown in panel d of Fig. 4.5. The foregoing discussions reveal that the $\widetilde{C}$ state is very weakly coupled with the $\widetilde{A}$ state only. Therefore, the population of this state remains almost unchanged over the entire period of dynamics considered here. The sharp peaks observed in its vibronic structure supports the above findings.

4.3.5 Correlations with the benzene and fluorobenzene radical cations

It is worth while at this point to compare some of the above findings with those of the Jahn-Teller (JT) and non-JT analogue benzene radical cation (Bz$^+$) and fluorobenzene radical cation (F-Bz$^+$), respectively. Particularly, it will be of interest to understand how the substitution effects prevail in the MO sequence, vibronic band structure and the ultrafast nonradiative dynamics of the excited states. The HOMO and a few low-lying MOs of benzene (Bz), fluorobenzene (F-Bz) and PA are sketched in Fig. 4.7. The HOMO of Bz comprises the components of the degenerate e_{1g} MO. Fluorine and acetylene substitution breaks the D_{6h} equilibrium symmetry of Bz to C_{2v} in F-Bz and PA and the orbital degeneracy is split. The HOMO and HOMO-1 in FBz and PA belong to nondegenerate b_1 and a_2 species, respectively, and correlates to the two components of the e_{1g} MO of Bz. The HOMO-1 of Bz again comprises the two components of the degenerate e_{2g} MO. It can be seen that the second component of this MO correlates to the HOMO-2 of b_2 symmetry of F-Bz. The HOMO-3 of the latter of b_1 symmetry correlates to the nondegenerate a_{2u} MO (HOMO-2) of Bz. The HOMO-2 and HOMO-3 of PA of b_2 and b_1 symmetry, respectively, on the other hand do not correlate to these MOs of either Bz or F-Bz. Instead, the HOMO-2 and HOMO-3 of PA describe the acetylenic π-type orbital parallel and perpendicular to the phenyl ring, respectively.

It follows from Fig. 4.7 that within the Koopman's theorem in the MO picture, the $\widetilde{X}^2E_{1g}$ JT state of Bz$^+$ would correlate to the $\widetilde{X}^2B_1$ and $\widetilde{A}^2A_2$ electronic states of both F-Bz$^+$ and PA$^+$. The $\widetilde{B}^2B_2$ and $\widetilde{C}^2B_1$ states of F-Bz$^+$ would correlate to one component of the $\widetilde{X}^2E_{2g}$ JT state and the $\widetilde{B}^2A_{2u}$ state of Bz$^+$, respectively. The $\widetilde{B}^2B_2$ and $\widetilde{C}^2B_1$ state of PA$^+$ on the other hand, do not correspond to the corresponding states of F-Bz$^+$ and also of Bz$^+$. Therefore, the $\widetilde{B}$ and $\widetilde{C}$ states of PA$^+$ seems to be very different and originate from the ionization from
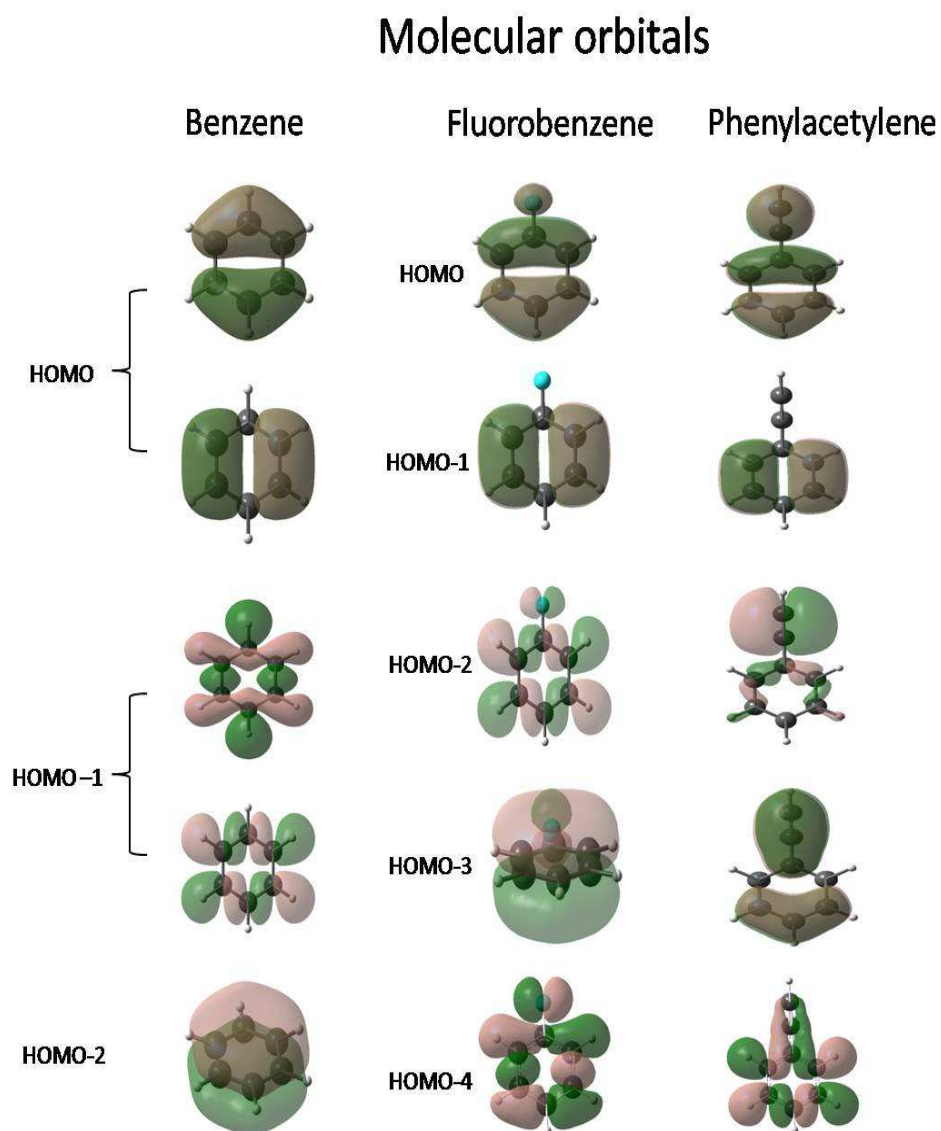
Figure 4.7: Schematic plots of the canonical MOs of benzene, fluorobenzene and PA for the respective equilibrium configurations.

Table 4.6: Frequencies and coupling constants (in eV) of relevant vibrational modes for the JT active $\widetilde{X}^2E_{1g}$ state of Bz$^+$ and their counterparts for the $\widetilde{X}^2B_1$ and $\widetilde{A}^2A_2$ electronic states of F-Bz$^+$ (PA$^+$). The results for Bz$^+$ and F-Bz$^+$ reproduced from Ref. [140] and Ref. [137], respectively.

Species	Vibrational modes		Frequency	Coupling parameter	
				$\widetilde{X}^2E_{1g}$	
Bz$^+$	e_{2g}	ν_6	0.0767	0.077	
		ν_8	0.2053	0.152	
				$\widetilde{X}^2B_1$	$\widetilde{A}^2A_2$
F-Bz$^+$ (PA$^+$)	a_1	ν_{6a}	0.0643 (0.0576)	0.091 (-0.058)	-0.055 (0.065)
		ν_{8a}	0.2021 (0.2049)	0.176 (-0.132)	-0.125 (0.154)
	b_2	ν_{6b}	0.077 (0.0772)	0.075 (0.050)	
		ν_{8b}	0.203 (0.2016)	0.158 (0.123)	

the acetylenic π-type of orbitals. The relation between the Bz$^+$ and its non-JT counterpart, F-Bz$^+$ has been discussed by Bâldea *et al.* [137]. A comparison of the static and dynamical aspects of the JT $\widetilde{X}^2E_{1g}$ state in Bz$^+$ vs. the corresponding nondegenerate $\widetilde{X}^2B_1$-$\widetilde{A}^2A_2$ states in F-Bz$^+$ is the following. The degenerate (e_{2g}) skeletal deformation (ν_6) and C=C stretching (ν_8) vibrational modes are most strongly JT active in the $\widetilde{X}$ state of Bz$^+$ [140]. These transform to ν_{6a}, ν_{6b} and ν_{8a}, ν_{8b} (in Wilson's numbering) in F-Bz$^+$ and are the most active Condon and coupling modes, respectively [137]. Therefore, the moderate JT coupling due to these modes in Bz$^+$ prevails in a comparable manner in the vibronic dynamics of the $\widetilde{X}$-$\widetilde{A}$ coupled electronic manifold of F-Bz$^+$. The lower part of the better resolved MATI spectrum of the two exhibit similar pattern.

The scenario in the $\widetilde{X}$-$\widetilde{A}$ states of PA$^+$ is quite analogous to the above picture as discussed before in the text. We reiterate that both the C=C stretching (6a and 6b) and the skeletal deformation (8a and 8b) modes in PA$^+$ are similarly active as in the case of F-Bz$^+$. The coupling strengths and harmonic vibrational frequencies of these modes in Bz$^+$, F-Bz$^+$ and PA$^+$ are comparable as can be seen from Table. 4.6. What seems to be more novel in PA$^+$ in addition is very strong coupling due to the low frequency bending mode ν_{36} (15) and also moderate coupling due to another low frequency bending mode ν_{33} (β_{CH}) (cf., Table. 4.4).

These two modes involve the acetylenic moiety and are absent in Bz^+ and F-Bz^+. Excitation of the fundamentals, overtones and combinations of these modes are observed in the MATI spectrum of the $\widetilde{X}$ state of PA^+ as discussed in Sec. 4.3.3. The broad structure of the $\widetilde{A}$ band correlates well with that of F-Bz^+. A nonradiative decay rate of ~ 20 fs is estimated for the $\widetilde{A}$ state of both these cations. Both the $\widetilde{B}$ and $\widetilde{C}$ bands of PA^+ originate from an ionization of the acetylenic moiety, which is supported by the excitation of the C≡C stretching vibration ν_5 in these states, and bear no correlations with those of F-Bz^+. For example, the $\widetilde{B}$ state decays at a relatively faster rate in PA^+. The $\widetilde{C}$ state of the latter is found to be long lived, where as, a decay rate of ~ 20-30 fs is estimated for this state in F-Bz^+ [137].

4.4 Summary and outlook

A theoretical account of the quantum chemistry and dynamics of the four low-lying electronic states of phenylacetylene radical cation are examined in this article. A model diabatic electronic Hamiltonian is constructed with the aid of dimensionless normal coordinates and *ab initio* electronic structure calculations. First principles simulation of nuclear dynamics is carried out to determine the vibrational level structure of the electronic states and their time-dependent properties.

The electronic structure data reveals a strong coupling between the $\widetilde{X}$ and $\widetilde{A}$ electronic states of PA^+. The coupling of the $\widetilde{C}$ state with the $\widetilde{A}$ state is found to be quite weak. The $\widetilde{B}$ state is moderately coupled to both the $\widetilde{X}$ and $\widetilde{A}$ states. Considering the possibility of various intra- and inter-state coupling, we find that 24 (out of 36) vibrational modes are relevant for the nuclear dynamics of the $\widetilde{X}$-$\widetilde{A}$-$\widetilde{B}$-$\widetilde{C}$ electronic states of PA^+. The full simulations of the nuclear dynamics are therefore carried out on the four coupled electronic states including these 24 vibrational modes and employing the MCTDH WP propagation algorithm. The

resulting vibronic spectrum is found to be in excellent accord with the broad band PE spectroscopy results attesting the reliability of the present theoretical model. Partial simulations of the nuclear dynamics are also carried out employing the matrix diagonalization approach to calculate the precise locations of the vibrational levels and to compare with the better resolved MATI spectrum of the $\widetilde{X}$ state and PIRI and photodissociation spectrum of the $\widetilde{C}$ state. Except for ν_{13} in the PIRI spectrum, excitations of all other totally symmetric modes are found to be in accord with the experimental data. Strong coupling between $\widetilde{X}$ and $\widetilde{A}$ electronic states triggers weak excitations of the fundamentals of the nontotally symmetric b_2 vibrational modes in the MATI spectrum of the $\widetilde{X}$ state. Because of very weak coupling between the $\widetilde{A}$ and $\widetilde{C}$ electronic states, the weak excitations of the nontotally symmetric modes assigned in the PIRI spectrum are not observed in the present theoretical results. The assignment of the complex vibrational spectrum of the $\widetilde{A}$ and $\widetilde{B}$ state appears to be a formidable task because of the nonadiabatic mixing. The $\widetilde{A}$ band is particularly very diffuse and broad and a nonradiative decay time of ~ 20 fs has been estimated for this state. Nonadiabatic effects on the $\widetilde{B}$ band are relatively mild and therefore its PE spectrum reveals structures. A nonradiative decay rate of ~ 88 fs is estimated for the $\widetilde{B}$ state from the theoretical data, although experimentally it is predicted to be a long-lived state of PA$^+$.

Despite a very good agreement between the theory and experiment as regard to the PE spectroscopy results, the high-resolution spectroscopy results perhaps would require further refinements. Part of the problem behind the discrepancy is difficult to repair as a full dimensional simulation using the matrix diagonalization approach is beyond the scope for this large polyatomic molecular system with many relevant degrees of freedom. Another part concerns the further refinement of the *ab initio* electronic structure data and examination of other possible interstate couplings, particularly, between the $\widetilde{C}$ state and further higher electronic states of PA$^+$. Such an exercise is left for the future work.

Chapter 5

Photophysics of naphthalene radical cation

5.1 Introduction

Understanding of the origin of diffused interstellar bands (DIBs) and their assignments are long standing issues in astrophysical investigations [141]. The consensus is, they originate from electronically excited radical cations of polycyclic aromatic hydrocarbons (PAHs), most abundant in the interstellar medium (ISM) [142]. This PAH hypothesis inspired new laboratory measurements in the typical conditions of ISM which revealed diffuse vibronic bands and subpicosecond dynamics of their low-lying electronic states [54, 56–58, 149, 150, 153] Very recently, spectroscopic measurements of moderately reddened star Cernis 52 located in the Perseus molecular cloud lead to the discovery of three new DIBs [59]. Aided by the laboratory measurements they are assigned to the electronic transitions in the naphthalene radical cation (Np^+). Despite some attempts [154–159] a detailed complementary theoretical study is missing till date.

The present chapter deals with the electronic structure and nuclear dynamics of Np^+. Neutral naphthalene (Np) belongs to D_{2h} symmetry point group at
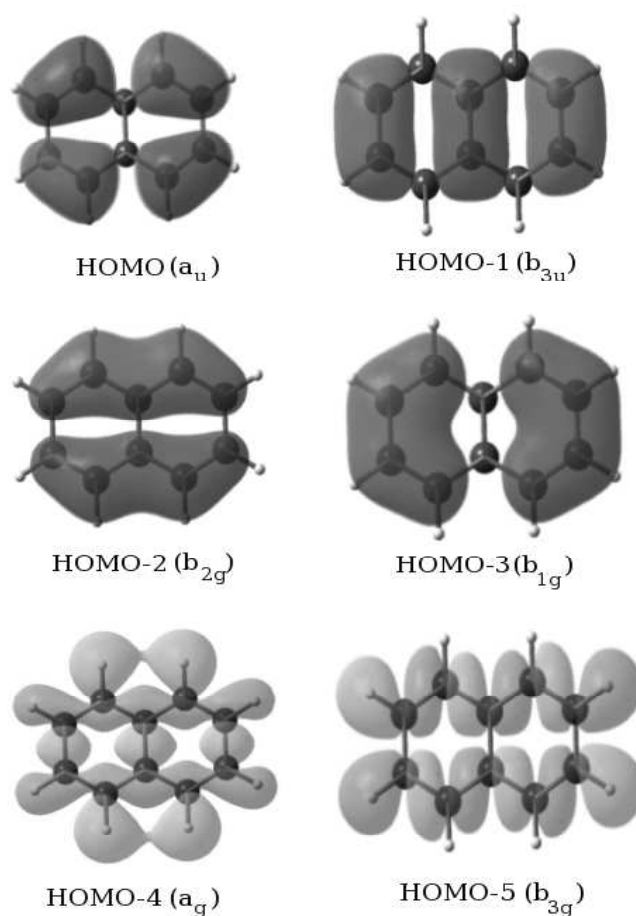
Figure 5.1: Schematic diagram of the valance molecular orbitals of naphthalene.

the equilibrium geometry of its $\widetilde{X}^1 A_g$ electronic ground state. The six low-lying electronic states $\widetilde{X}^2 A_u(D_0)$, $\widetilde{A}^2 B_{3u}(D_1)$, $\widetilde{B}^2 B_{2g}(D_2)$, $\widetilde{C}^2 B_{1g}(D_3)$, $\widetilde{D}^2 A_g(D_4)$ and $\widetilde{E}^2 B_{3g}(D_5)$ of Np$^+$ results from valence ionization of six highest occupied molecular orbitals (HOMOs) a_u, b_{3u}, b_{2g}, b_{1g}, a_g and b_{3g} of Np. These MOs are of π-type and are schematically shown in Fig. 5.1. The 48 vibrational degrees of freedom of Np decomposes into the following irreducible representation of the D_{2h} symmetry point group,

$$\Gamma_{vib} = 9a_g + 3b_{1g} + 4b_{2g} + 8b_{3g} + 4a_u + 8b_{1u} + 8b_{2u} + 4b_{3u}$$
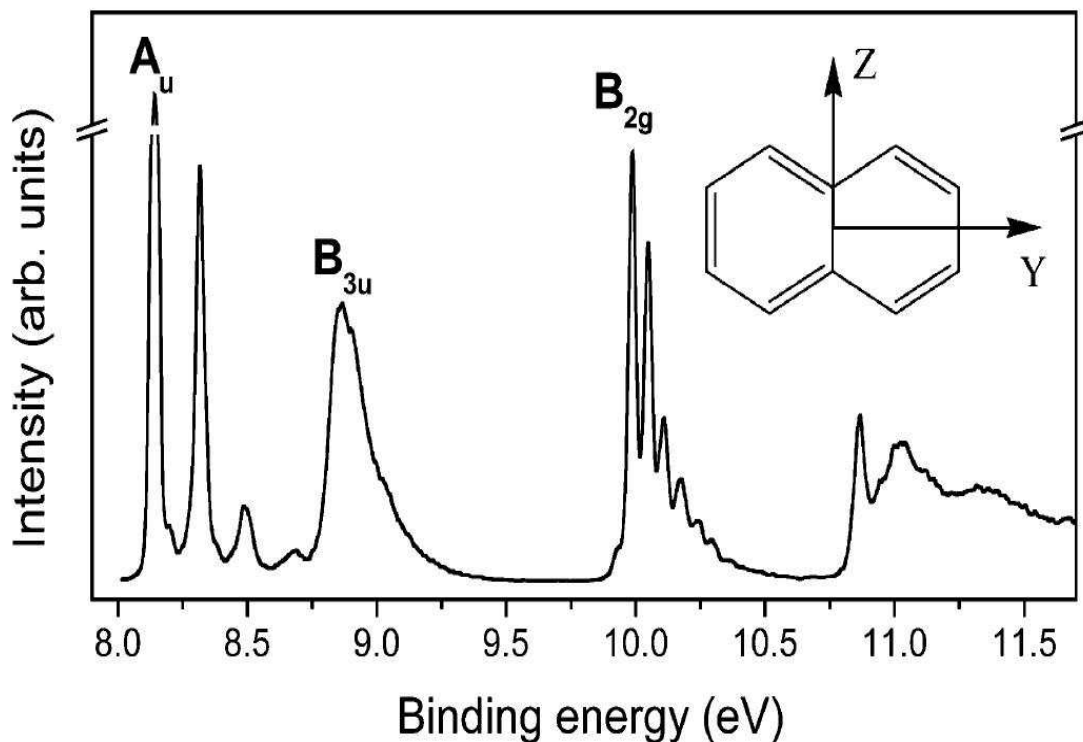
Figure 5.2: The experimental gas phase photoelectron spectrum of naphthalene reproduced from Ref. [149].

The totally symmetric vibrational modes (a_g) are always Condon active within a given electronic state [22]. The possible interstate coupling vibrational modes between different electronic states of Np^+ are derived from symmetry selection rules discussed in Chapter 2.

The photoelectron spectrum of NP is recorded by various experimental groups [143–150]. The high resolution gas phase spectrum recorded by da Silva Filho *et al.* [149], shown in Fig. 5.2 reveals well resolved vibronic structures of the $\widetilde{X}$ and $\widetilde{B}$ electronic states and a broad band for the $\widetilde{A}$ state. The highly overlapping bands for the $\widetilde{C}$, $\widetilde{D}$ and $\widetilde{E}$ electronic states show complex structure in the 10.75-11.75 eV ionization energy range. The broadening of the $\widetilde{A}$ band in the spectrum is attributed to the vibronic coupling of $\widetilde{X}$ with the $\widetilde{A}$ state [149]. Excitation of nontotally symmetric vibrational modes (b_{1g}) in the $\widetilde{X}$ state of Np^+ was observed in a two color zero kinetic energy (ZEKE)-photoelectron spectroscopy
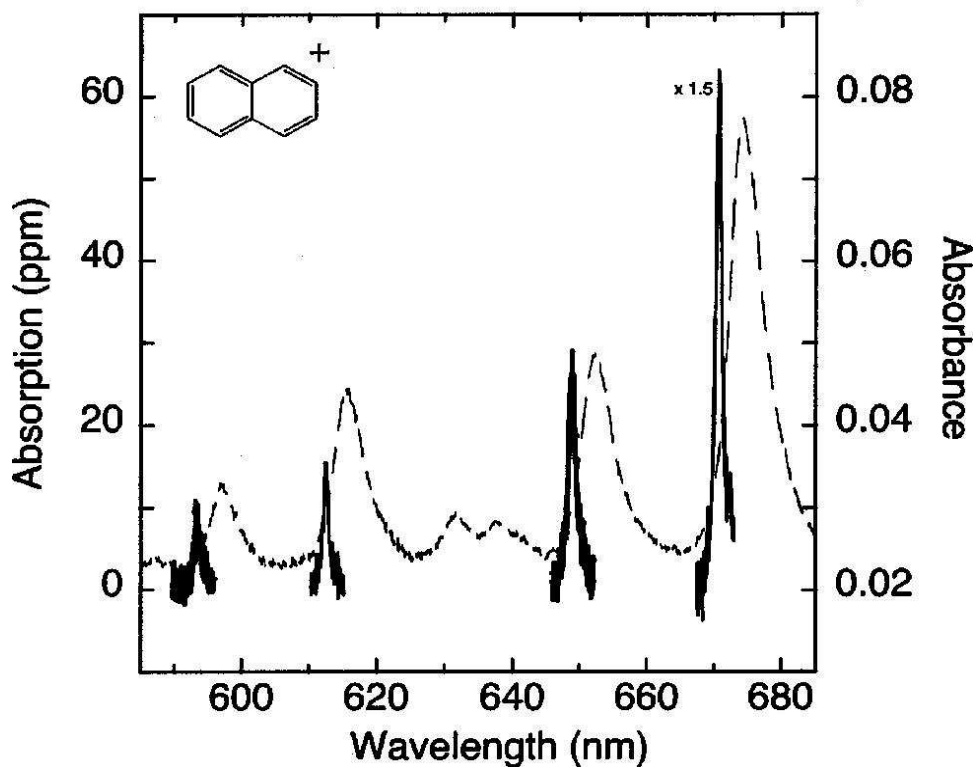
Figure 5.3: The vibrational progression of the D_2 $(\widetilde{B})$ ← D_0 $(\widetilde{X})$ electronic transition of Np^+ reproduced from Ref. [58].

measurement [151].

The gas phase electronic absorption spectrum of Np^+ has been the subject of major interest. The DIBs, the absorption features observed over the interstellar media in the range of ultraviolet and infrared region of electromagnetic spectrum, are linked to the electronic transitions of Np^+. The novel experimental spectroscopic techniques such as matrix isolation spectroscopy, cavity ringdown spectroscopy and photodissociation of van der Waals complex are developed and utilized to explore the intrinsic band profiles of the low-lying electronic states of Np^+. The vibrational peak positions and widths are measured in the laboratory experiments by mimicking astrophysical environments and are directly compared with the observed DIBs. The resolved vibrational structures of D_2 $(\widetilde{B})$ ← D_0 $(\widetilde{X})$ transition are reported [54, 56–58, 152]. The four sharp peaks in this transition (shown in Fig. 5.3) correspond to the excitation of the two totally symmetric

vibrational modes [58]. The recorded experimental data have been used recently to assign the three new DIBs discovered by astronomers [59]. So far no theoretical data is available to validate this assignment. The vibrational structure of D_3 $(\widetilde{C})$ $\leftarrow D_0$ $(\widetilde{X})$ transition revealed larger peak widths compared to that of D_2 $(\widetilde{B})$ $\leftarrow$ D_0 $(\widetilde{X})$ transition [57].

The relaxation dynamics of electronically excited Np^+ is studied in glass matrix environments using (femto) picosecond transient grating spectroscopic techniques [153]. A biexponential recovery kinetics of the photobleached D_0 $(\widetilde{X})$ state containing a fast ($\approx$ 200 fs) and a slow ($\approx$ 3-20 ps) component is observed [153]. The former is attributed to the D_2 $(\widetilde{B})$ $\leftarrow D_0$ $(\widetilde{X})$ transition and the latter is to the vibrational relaxation of the D_0 $(\widetilde{X})$ state in the matrix. The D_2 state relaxation time was further estimated later to be $\approx$ 212 fs from the cavity ringdown spectroscopy data [58] shown in Fig. 5.3. A nonradiative decay rate of $\sim 1.7x10^{13}$ s^{-1} is estimated for D_3 $(\widetilde{C})$ electronic state from the absorption spectroscopy measurements [57]. These results reveal that the excited state intramolecular dynamics of Np^+ is quite involved and is dominated by ultrafast internal conversion mechanism. This issue is also unraveled below.

Although there are several theoretical studies on the electronic structure of Np^+ [148, 150, 154–159], the mechanistic details of the dynamical processes are not explored, presumably due to its large dimensionality and the complex nature of vibronic interactions. We address these unresolved issues here and develop a theoretical model through *ab initio* electronic structure calculations and simulate the nuclear dynamics quantum mechanically employing a vibronic coupling approach [22] aided by the MCTDH WP propagation [109] as well as matrix diagonalization methods.

5.2 Vibronic Hamiltonian

A vibronic coupling model is established using a diabatic ansatz for the electronic basis [89–91] and dimensionless normal coordinates of the reference electronic ground state of Np. The Hamiltonian for the $\widetilde{X}$-$\widetilde{A}$-$\widetilde{B}$-$\widetilde{C}$-$\widetilde{D}$-$\widetilde{E}$ coupled electronic manifold can be written as

$$\mathcal{H} = (\mathcal{T}_N + \mathcal{V}_0)\mathbf{1_6} + \Delta\mathcal{H} \tag{5.1}$$

where $\mathbf{1_6}$ is a 6×6 unit matrix and $\mathcal{T}_N$ and $\mathcal{V}_0$ are the kinetic and potential energy operators of the reference state of the Np. This state is assumed to be harmonic and vibronically decoupled from the other states. The electronic Hamiltonian matrix of the ionic states, $\Delta\mathcal{H}$, is given by

$$\Delta\mathcal{H} = \begin{pmatrix} W_{\widetilde{X}} & W_{\widetilde{X}-\widetilde{A}} & W_{\widetilde{X}-\widetilde{B}} & W_{\widetilde{X}-\widetilde{C}} & W_{\widetilde{X}-\widetilde{D}} & W_{\widetilde{X}-\widetilde{E}} \\ & W_{\widetilde{A}} & W_{\widetilde{A}-\widetilde{B}} & W_{\widetilde{A}-\widetilde{C}} & W_{\widetilde{A}-\widetilde{D}} & W_{\widetilde{A}-\widetilde{E}} \\ & & W_{\widetilde{B}} & W_{\widetilde{B}-\widetilde{C}} & W_{\widetilde{B}-\widetilde{D}} & W_{\widetilde{B}-\widetilde{E}} \\ h.c & & & W_{\widetilde{C}} & W_{\widetilde{C}-\widetilde{D}} & W_{\widetilde{C}-\widetilde{E}} \\ & & & & W_{\widetilde{D}} & W_{\widetilde{D}-\widetilde{E}} \\ & & & & & W_{\widetilde{E}} \end{pmatrix}. \tag{5.2}$$

In the above, the diagonal and off-diagonal elements refer to the energy of the diabatic electronic and their coupling surfaces, respectively. The elements of the above matrix Hamiltonian are expanded in a Taylor series around the equilibrium geometry ($\mathbf{Q}$=0) of the reference state as

$$W_j = E_0^{(j)} + \sum_{i=1}^{9} \kappa_i^{(j)} Q_i + \frac{1}{2}\sum_{i=1}^{48} \gamma_i^{(j)} Q_i^2 \ ; \quad j \ \in \ \widetilde{X}, \widetilde{A}, \widetilde{B}, \widetilde{C}, \widetilde{D}, \widetilde{E} \tag{5.3}$$

$$W_{j-k} \quad = \quad \sum_i \lambda_i^{(j-k)} Q_i \qquad (5.4)$$

The quantity $E_0^{(j)}$ is the vertical ionization energy of the jth electronic state. $\kappa_i^{(j)}$ and $\gamma_i^{(j)}$ are the first and second-order coupling parameters of the ith vibration in the jth electronic state, respectively. The quantity $\lambda^{(j-k)}$ is the linear parameter of coupling between electronic states, j and k, through i^{th} vibration. The complete set of coupling parameters for the $\widetilde{X}$, $\widetilde{A}$, $\widetilde{B}$, $\widetilde{C}$, $\widetilde{D}$ and $\widetilde{E}$ electronic states of the Np^+ are computed *ab initio* as mentioned in Chapter 2 and are listed in Table 5.1-5.5.

A concise account of the coupling parameters of the Hamiltonian is as follows. A large excitation strength for the ν_7 in the $\widetilde{X}$, ν_1 and ν_2 in the $\widetilde{A}$, ν_1 in the $\widetilde{B}$, ν_3 and ν_6 in the $\widetilde{C}$, ν_1, ν_5 and ν_7 in the $\widetilde{D}$ and ν_1, ν_2, ν_6 and ν_7 in the $\widetilde{E}$ state can be seen from the Table 5.1. The vibrations ν_5 and ν_6 in the $\widetilde{X}$, ν_3 and ν_7 in the $\widetilde{A}$, ν_2 and ν_7 in the $\widetilde{B}$, ν_2 in the $\widetilde{C}$ state have moderate excitation strength. The excitation of the remaining a_{1g} vibrations are weak. The vibrational modes of a_u symmetry, ν_{10} and ν_{11} between the $\widetilde{A}$-$\widetilde{E}$, ν_{10} between the $\widetilde{X}$-$\widetilde{D}$ states possesses large coupling strength (cf., Table 5.2-5.3). In case of b_{1g} symmetry vibrations, ν_{14} between the $\widetilde{B}$-$\widetilde{E}$, ν_{14} and ν_{16} between the $\widetilde{C}$-$\widetilde{D}$ states, have large coupling strength. The b_{1u} symmetry vibrational modes have moderate coupling between the $\widetilde{X}$-$\widetilde{C}$ and $\widetilde{A}$-$\widetilde{B}$ states. The $\widetilde{B}$-$\widetilde{D}$ and $\widetilde{C}$-$\widetilde{D}$ states are strongly coupled by the vibrational modes of b_{2g} symmetry. The vibrations of b_{2u} symmetry couple the $\widetilde{X}$-$\widetilde{B}$ states and ν_{29}, ν_{32} and ν_{34} reveal moderate coupling in this case. A moderate coupling strength of ν_{34} between $\widetilde{A}$-$\widetilde{C}$ states can also be found from Table 5.2. Among the vibrational modes of b_{3g} symmetry, the coupling strengths of ν_{37} and ν_{42} are largest between the $\widetilde{X}$-$\widetilde{A}$ and $\widetilde{D}$-$\widetilde{E}$ states. The $\widetilde{A}$ and $\widetilde{D}$ states are strongly coupled by the vibrational mode, ν_{46}, of b_{3u} symmetry.

Table 5.1: The linear intrastate coupling parameters (κ_i) for the $\widetilde{X}^2 A_u$, $\widetilde{A}^2 B_{3u}$, $\widetilde{B}^2 B_{2g}$, $\widetilde{C}^2 B_{1g}$, $\widetilde{D}^2 A_g$ and $\widetilde{E}^2 B_{3g}$ electronic states of the Np$^+$ are derived from the OVGF data. The dimensionless coupling strengths, $\kappa^2/2\omega^2$ are given in parentheses. The vertical ionization energies of the ground and excited electronic states of the this radical cation are also given. All quantities are given in eV.

modes (symmetry)	frequency (eV)	κ $\widetilde{X}^2 A_u$	κ $\widetilde{A}^2 B_{3u}$	κ $\widetilde{B}^2 B_{2g}$	κ $\widetilde{C}^2 B_{1g}$	κ $\widetilde{D}^2 A_g$	κ $\widetilde{E}^2 B_{3g}$
$\nu_1(a_g)$	0.0638	-0.0162(0.032)	0.0467(0.269)	-0.0898(0.990)	0.0013(0.0002)	-0.1121(1.543)	0.0927(1.056)
$\nu_2(a_g)$	0.0956	0.0034(0.001)	-0.0890(0.433)	-0.0371(0.075)	-0.0563(0.174)	0.0149(0.012)	-0.0651(0.232)
$\nu_3(a_g)$	0.1303	-0.0059(0.001)	-0.0589(0.102)	-0.0073(0.002)	-0.1280(0.483)	0.0438(0.056)	-0.0283(0.024)
$\nu_4(a_g)$	0.1451	0.0346(0.028)	-0.0502(0.060)	0.0346(0.028)	-0.0093(0.002)	0.0097(0.002)	-0.0334(0.027)
$\nu_5(a_g)$	0.1808	-0.0841(0.108)	-0.0166(0.004)	0.0558(0.048)	0.0125(0.002)	-0.1355(0.283)	0.0534(0.044)
$\nu_6(a_g)$	0.1847	0.1095(0.176)	0.0412(0.025)	-0.0664(0.065)	0.1323(0.257)	0.0547(0.044)	-0.1504(0.334)
$\nu_7(a_g)$	0.2014	0.1633(0.329)	-0.1246(0.192)	0.1195(0.176)	0.0319(0.013)	-0.2673(0.881)	0.2728(0.919)
$\nu_8(a_g)$	0.3979	0.0045(0.001)	0.0149(0.001)	0.0026(0.001)	0.0117(0.001)	-0.0944(0.028)	0.0769(0.019)
$\nu_9(a_g)$	0.4015	0.0169(0.001)	0.0200(0.001)	0.0181(0.001)	0.0356(0.004)	-0.0362(0.004)	-0.0672(0.014)
E_X^0	7.7903						
E_A^0	8.4987						
E_B^0	9.7589						
E_C^0	10.9475						
E_D^0	11.3785						
E_E^0	11.5299						

Table 5.2: The linear interstate vibronic coupling parameters (λ_i) for the $\widetilde{X}$-$\widetilde{A}$-$\widetilde{B}$-$\widetilde{C}$-$\widetilde{D}$-$\widetilde{E}$ electronic states of the Np$^+$ derived from the OVGF data. The dimensionless coupling strengths, $\lambda^2/2\omega^2$ are given in parentheses. All quantities are given in eV.

modes (symmetry)	$\lambda_{X,A}$ $\widetilde{X}^2A_u$-$\widetilde{A}^2B_{3u}$	$\lambda_{X,B}$ $\widetilde{X}^2A_u$-$\widetilde{B}^2B_{2g}$	$\lambda_{X,C}$ $\widetilde{X}^2A_u$-$\widetilde{C}^2B_{1g}$	$\lambda_{X,D}$ $\widetilde{X}^2A_u$-$\widetilde{D}^2A_g$	$\lambda_{X,E}$ $\widetilde{X}^2A_u$-$\widetilde{E}^2B_{3g}$	$\lambda_{A,B}$ $\widetilde{A}^2B_{3u}$-$\widetilde{B}^2B_{2g}$	$\lambda_{A,C}$ $\widetilde{A}^2B_{3u}$-$\widetilde{C}^2B_{1g}$
$\nu_{10}(a_u)$	-	-	-	-	-	-	-
$\nu_{11}(a_u)$	-	-	-	0.0843 (0.739)	-	-	-
$\nu_{12}(a_u)$	-	-	-	-	-	-	-
$\nu_{13}(a_u)$	-	-	-	-	-	-	-
$\nu_{14}(b_{1g})$	-	-	-	-	-	-	-
$\nu_{15}(b_{1g})$	-	-	-	-	-	-	-
$\nu_{16}(b_{1g})$	-	-	-	-	-	-	-
$\nu_{17}(b_{1u})$	-	-	0.0223 (0.128)	-	-	-	-
$\nu_{18}(b_{1u})$	-	-	-	-	-	0.0650 (0.213)	-
$\nu_{19}(b_{1u})$	-	-	0.0696 (0.122)	-	-	-	-
$\nu_{20}(b_{1u})$	-	-	-	-	-	0.0539 (0.058)	-
$\nu_{21}(b_{1u})$	-	-	-	-	-	0.0349 (0.020)	-
$\nu_{22}(b_{1u})$	-	-	0.1321 (0.212)	-	-	0.1204 (0.176)	-
$\nu_{23}(b_{1u})$	-	-	-	-	-	-	-
$\nu_{24}(b_{1u})$	-	-	-	-	-	-	-
$\nu_{25}(b_{2g})$	-	-	-	-	-	-	-
$\nu_{26}(b_{2g})$	-	-	-	-	-	-	-
$\nu_{27}(b_{2g})$	-	-	-	-	-	-	-
$\nu_{28}(b_{2g})$	-	-	-	-	-	-	-
$\nu_{29}(b_{2u})$	-	0.0579 (0.286)	-	-	-	-	-
$\nu_{30}(b_{2u})$	-	0.0225 (0.015)	-	-	-	-	-
$\nu_{31}(b_{2u})$	-	0.0254 (0.015)	-	-	-	-	-
$\nu_{32}(b_{2u})$	-	0.0918 (0.179)	-	-	-	-	-
$\nu_{33}(b_{2u})$	-	0.0204 (0.006)	-	-	-	-	-
$\nu_{34}(b_{2u})$	-	0.1027 (0.141)	-	-	-	-	0.1108 (0.164)
$\nu_{35}(b_{2u})$	-	-	-	-	-	-	-
$\nu_{36}(b_{2u})$	-	-	-	-	-	-	-
$\nu_{37}(b_{3g})$	0.0579 (0.426)	-	-	-	-	-	-
$\nu_{38}(b_{3g})$	0.0271 (0.028)	-	-	-	-	-	-
$\nu_{39}(b_{3g})$	0.0430 (0.045)	-	-	-	-	-	-
$\nu_{40}(b_{3g})$	0.0298 (0.018)	-	-	-	-	-	-
$\nu_{41}(b_{3g})$	0.0183 (0.005)	-	-	-	-	-	-
$\nu_{42}(b_{3g})$	0.1579 (0.285)	-	-	-	-	-	-
$\nu_{43}(b_{3g})$	-	-	-	-	-	-	-
$\nu_{44}(b_{3g})$	-	-	-	-	-	-	-
$\nu_{45}(b_{3u})$	-	-	-	-	-	-	-
$\nu_{46}(b_{3u})$	-	-	-	-	-	-	-
$\nu_{47}(b_{3u})$	-	-	-	-	-	-	-
$\nu_{48}(b_{3u})$	-	-	-	-	-	-	-

Table 5.3: The linear interstate vibronic coupling parameters (λ_i) for the $\widetilde{A}$-$\widetilde{B}$-$\widetilde{C}$-$\widetilde{D}$-$\widetilde{E}$ electronic states of the Np$^+$ derived from the OVGF data. The dimensionless coupling strengths, $\lambda^2/2\omega^2$ are given in parentheses. All quantities are given in eV.

modes (symmetry)	$\lambda_{A,D}$ $\widetilde{A}^2 B_{3u}$-$\widetilde{D}^2 A_g$	$\lambda_{A,E}$ $\widetilde{A}^2 B_{3u}$-$\widetilde{E}^2 B_{3g}$	$\lambda_{B,C}$ $\widetilde{B}^2 B_{2g}$-$\widetilde{C}^2 B_{1g}$	$\lambda_{B,D}$ $\widetilde{B}^2 B_{2g}$-$\widetilde{D}^2 A_g$	$\lambda_{B,E}$ $\widetilde{B}^2 B_{2g}$-$\widetilde{E}^2 B_{3g}$	$\lambda_{C,D}$ $\widetilde{C}^2 B_{1g}$-$\widetilde{D}^2 A_g$	$\lambda_{C,E}$ $\widetilde{C}^2 B_{1g}$-$\widetilde{E}^2 B_{3g}$	$\lambda_{D,E}$ $\widetilde{D}^2 A_g$-$\widetilde{E}^2 B_{3g}$
$\nu_{10}(a_u)$	-	0.0744 (5.419)	-	-	-	-	-	-
$\nu_{11}(a_u)$	-	0.1694 (2.988)	-	-	-	-	-	-
$\nu_{12}(a_u)$	-	0.0491 (0.112)	-	-	-	-	-	-
$\nu_{13}(a_u)$	-	-	-	-	-	-	-	-
$\nu_{14}(b_{1g})$	-	-	-	-	0.0970 (2.148)	0.0762 (1.326)	-	-
$\nu_{15}(b_{1g})$	-	-	-	-	0.0346 (0.075)	-	-	-
$\nu_{16}(b_{1g})$	-	-	-	-	0.0225 (0.019)	0.1410 (0.757)	-	-
$\nu_{17}(b_{1u})$	-	-	-	-	-	-	-	-
$\nu_{18}(b_{1u})$	-	-	-	-	-	-	-	-
$\nu_{19}(b_{1u})$	-	-	-	-	-	-	-	-
$\nu_{20}(b_{1u})$	-	-	-	-	-	-	-	-
$\nu_{21}(b_{1u})$	-	-	-	-	-	-	-	-
$\nu_{22}(b_{1u})$	-	-	-	-	-	-	-	-
$\nu_{23}(b_{1u})$	-	-	-	-	-	-	-	-
$\nu_{24}(b_{1u})$	-	-	-	-	-	-	-	-
$\nu_{25}(b_{2g})$	-	-	-	-	-	-	0.0748 (0.895)	-
$\nu_{26}(b_{2g})$	-	-	-	0.0777 (0.687)	-	-	0.0503 (0.288)	-
$\nu_{27}(b_{2g})$	-	-	-	0.1308 (0.772)	-	-	0.0921 (0.383)	-
$\nu_{28}(b_{2g})$	-	-	-	0.1070 (0.412)	-	-	0.1460 (0.767)	-
$\nu_{29}(b_{2u})$	-	-	-	-	-	-	-	-
$\nu_{30}(b_{2u})$	-	-	-	-	-	-	-	-
$\nu_{31}(b_{2u})$	-	-	-	-	-	-	-	-
$\nu_{32}(b_{2u})$	-	-	-	-	-	-	-	-
$\nu_{33}(b_{2u})$	-	-	-	-	-	-	-	-
$\nu_{34}(b_{2u})$	-	-	-	-	-	-	-	-
$\nu_{35}(b_{2u})$	-	-	-	-	-	-	-	-
$\nu_{36}(b_{2u})$	-	-	-	-	-	-	-	-
$\nu_{37}(b_{3g})$	-	-	0.0132 (0.022)	-	-	-	-	0.0744 (0.704)
$\nu_{38}(b_{3g})$	-	-	0.0316 (0.038)	-	-	-	-	0.0410 (0.063)
$\nu_{39}(b_{3g})$	-	-	0.0645 (0.101)	-	-	-	-	0.0543 (0.072)
$\nu_{40}(b_{3g})$	-	-	0.0412 (0.035)	-	-	-	-	0.0290 (0.017)
$\nu_{41}(b_{3g})$	-	-	0.1029 (0.156)	-	-	-	-	0.0377 (0.021)
$\nu_{42}(b_{3g})$	-	-	-	-	-	-	-	0.3016 (1.038)
$\nu_{43}(b_{3g})$	-	-	0.0081 (0.001)	-	-	-	-	0.0397 (0.004)
$\nu_{44}(b_{3g})$	-	-	-	-	-	-	-	0.0575 (0.010)
$\nu_{45}(b_{3u})$	-	-	-	-	-	-	-	-
$\nu_{46}(b_{3u})$	0.1028 (1.604)	-	-	-	-	-	-	-
$\nu_{47}(b_{3u})$	-	-	-	-	-	-	-	-
$\nu_{48}(b_{3u})$	-	-	-	-	-	-	-	-

Table 5.4: The quadratic intrastate coupling parameters (γ_i) for the $\widetilde{X}^2 A_u$, $\widetilde{A}^2 B_{3u}$, $\widetilde{B}^2 B_{2g}$, $\widetilde{C}^2 B_{1g}$, $\widetilde{D}^2 A_g$ and $\widetilde{E}^2 B_{3g}$ electronic states of Np$^+$ derived from the OVGF data.

modes (symmetry)	frequency (eV)	$\gamma^{(X)}$ $\widetilde{X}^2 A_u$	$\gamma^{(A)}$ $\widetilde{A}^2 B_{3u}$	$\gamma^{(B)}$ $\widetilde{B}^2 B_{2g}$	$\gamma^{(C)}$ $\widetilde{C}^2 B_{1g}$	$\gamma^{(D)}$ $\widetilde{D}^2 A_g$	$\gamma^{(E)}$ $\widetilde{E}^2 B_{3g}$
$\nu_1(a_g)$	0.0638	-0.0014	-0.0014	0.0010	-0.0006	0.0060	-0.0102
$\nu_2(a_g)$	0.0956	-0.0026	0.0026	-0.0016	-0.0002	-0.0020	-0.0028
$\nu_3(a_g)$	0.1303	0.0002	0.0036	0.0006	0.0054	-0.0036	-0.0066
$\nu_4(a_g)$	0.1451	0.0058	0.0074	0.0054	0.0062	-0.0074	-0.0214
$\nu_5(a_g)$	0.1808	0.0044	0.0234	0.0058	0.0084	-0.0656	-0.0150
$\nu_6(a_g)$	0.1847	0.0044	0.0050	0.0134	0.0034	-0.0340	-0.0434
$\nu_7(a_g)$	0.2014	0.0040	0.0084	0.0010	0.0064	-0.0108	-0.0144
$\nu_8(a_g)$	0.3979	0.0042	0.0042	0.0034	0.0034	0.0012	0.0040
$\nu_9(a_g)$	0.4015	0.0032	0.0032	0.0028	0.0030	0.0012	-0.0050
$\nu_{10}(a_u)$	0.0226	0.0068	-0.0188	-0.0114	-0.0112	-0.0026	-0.0118
$\nu_{11}(a_u)$	0.0693	-0.0064	-0.0252	-0.0144	-0.0168	0.0014	0.0122
$\nu_{12}(a_u)$	0.1038	0.0088	-0.0006	-0.0020	-0.0132	-0.0140	0.0024
$\nu_{13}(a_u)$	0.1157	0.0052	0.0008	0.0002	-0.0190	-0.0010	-0.0282
$\nu_{14}(b_{1g})$	0.0468	-0.0104	-0.0112	-0.0272	-0.0274	0.0236	-0.0062
$\nu_{15}(b_{1g})$	0.0894	0.0094	0.0030	-0.0076	-0.0004	-0.0130	-0.0052
$\nu_{16}(b_{1g})$	0.1146	0.0098	0.0084	-0.0040	-0.0858	0.0734	-0.0032
$\nu_{17}(b_{1u})$	0.0441	-0.0046	0.0008	-0.0038	-0.0040	0.0038	-0.0088
$\nu_{18}(b_{1u})$	0.0995	0.0014	-0.0094	0.0042	-0.0018	-0.0138	-0.0250
$\nu_{19}(b_{1u})$	0.1412	0.0004	0.0042	-0.0010	0.0070	-0.0246	-0.0318
$\nu_{20}(b_{1u})$	0.1583	0.0032	-0.0016	0.0078	0.0030	-0.0286	-0.0232
$\nu_{21}(b_{1u})$	0.1744	0.0026	-0.0016	0.0026	0.0024	-0.0200	-0.0758
$\nu_{22}(b_{1u})$	0.2029	-0.0058	-0.0200	0.0252	0.0162	-0.0398	-0.1024
$\nu_{23}(b_{1u})$	0.3973	0.0046	0.0046	0.0042	0.0042	-0.0062	-0.0042
$\nu_{24}(b_{1u})$	0.3998	0.0044	0.0040	0.0038	0.0038	-0.0062	-0.0064

Table 5.5: The quadratic intrastate coupling parameters (γ_i) for the $\widetilde{X}^2 A_u$, $\widetilde{A}^2 B_{3u}$, $\widetilde{B}^2 B_{2g}$, $\widetilde{C}^2 B_{1g}$, $\widetilde{D}^2 A_g$ and $\widetilde{E}^2 B_{3g}$ electronic states of Np^+ derived from the OVGF data.

modes (symmetry)	frequency (eV)	$\gamma^{(X)}$ $\widetilde{X}^2 A_u$	$\gamma^{(A)}$ $\widetilde{A}^2 B_{3u}$	$\gamma^{(B)}$ $\widetilde{B}^2 B_{2g}$	$\gamma^{(C)}$ $\widetilde{C}^2 B_{1g}$	$\gamma^{(D)}$ $\widetilde{D}^2 A_g$	$\gamma^{(E)}$ $\widetilde{E}^2 B_{3g}$
$\nu_{25}(b_{2g})$	0.0559	-0.0058	-0.0206	-0.0098	-0.0214	-0.0158	0.0156
$\nu_{26}(b_{2g})$	0.0663	0.0018	0.0016	-0.0220	-0.0202	-0.0076	-0.0018
$\nu_{27}(b_{2g})$	0.1053	0.0134	0.0060	-0.0284	-0.0324	0.0126	0.0230
$\nu_{28}(b_{2g})$	0.1179	0.0052	0.0036	-0.0136	-0.0738	0.0140	0.0598
$\nu_{29}(b_{2u})$	0.0766	-0.0082	-0.0006	-0.0012	-0.0008	-0.0114	-0.0144
$\nu_{30}(b_{2u})$	0.1292	-0.0004	-0.0010	0.0010	-0.0018	-0.0052	-0.0062
$\nu_{31}(b_{2u})$	0.1450	0.0070	0.0102	0.0088	0.0090	-0.0152	-0.0148
$\nu_{32}(b_{2u})$	0.1556	-0.0012	0.0062	0.0016	-0.0076	-0.0194	-0.0062
$\nu_{33}(b_{2u})$	0.1853	0.0282	0.0332	0.0290	0.0322	-0.0626	-0.0466
$\nu_{34}(b_{2u})$	0.1936	-0.0104	-0.0066	0.0112	0.0136	-0.0824	-0.0480
$\nu_{35}(b_{2u})$	0.3976	0.0048	0.0042	0.0036	0.0040	-0.0216	0.0024
$\nu_{36}(b_{2u})$	0.4014	0.0036	0.0038	0.0030	0.0032	-0.0040	-0.0140
$\nu_{37}(b_{3g})$	0.0627	-0.0110	0.0078	-0.0012	-0.0008	-0.0594	0.0512
$\nu_{38}(b_{3g})$	0.1154	-0.0030	0.0012	-0.0036	-0.0004	-0.0534	-0.0134
$\nu_{39}(b_{3g})$	0.1439	-0.0012	0.0092	-0.0022	0.0116	-0.0432	0.0220
$\nu_{40}(b_{3g})$	0.1556	-0.0004	0.0046	0.0016	0.0074	-0.0276	-0.0066
$\nu_{41}(b_{3g})$	0.1840	-0.0016	0.0002	-0.0136	0.0214	-0.0536	-0.0188
$\nu_{42}(b_{3g})$	0.2093	-0.0636	0.0656	0.0042	0.0004	-0.3626	0.3296
$\nu_{43}(b_{3g})$	0.3971	0.0050	0.0048	0.0042	0.0044	-0.0242	0.0138
$\nu_{44}(b_{3g})$	0.3998	0.0048	0.0042	0.0042	0.0040	-0.0370	0.0324
$\nu_{45}(b_{3u})$	0.0208	-0.0186	0.0006	-0.0114	-0.0160	-0.0040	0.0012
$\nu_{46}(b_{3u})$	0.0574	-0.0134	0.0006	-0.0196	-0.0040	0.0152	-0.0244
$\nu_{47}(b_{3u})$	0.0973	-0.0006	0.0062	-0.0010	-0.0120	-0.0114	-0.0052
$\nu_{48}(b_{3u})$	0.1155	0.0094	0.0090	0.0028	-0.0318	-0.0558	-0.0064

5.3 Results and Discussion

5.3.1 Adiabatic potential energy surfaces and Conical Intersections

The adiabatic PESs of the $\widetilde{X}$, $\widetilde{A}$, $\widetilde{B}$, $\widetilde{C}$, $\widetilde{D}$ and $\widetilde{E}$ electronic states of Np$^+$ are obtained by diagonalizing the diabatic electronic Hamiltonian of Eq. (5.1). One dimensional cuts of the multidimensional adiabatic PESs of Np$^+$ are shown in Fig. 5.4 along the nine a_g vibrational modes, ν_1-ν_9. The low-energy curve crossings of $\widetilde{X}$-$\widetilde{A}$ and $\widetilde{A}$-$\widetilde{B}$ states can only be seen along the C=C stretching vibrational mode ν_7. The $\widetilde{B}$-$\widetilde{C}$ and $\widetilde{B}$-$\widetilde{D}$ states cross along ν_6 (at higher energies) and ν_7 vibrational modes, respectively. As $\widetilde{C}$, $\widetilde{D}$ and $\widetilde{E}$ states are energetically close lying at the vertical configuration, the crossings of these states are seen along the all nine vibrational modes. Various low-energy crossings of $\widetilde{X}$-$\widetilde{A}$-$\widetilde{B}$-$\widetilde{C}$-$\widetilde{D}$-$\widetilde{E}$ electronic states are shown more clearly in Fig. 5.5 along the totally symmetric vibrational mode ν_7. The computed *ab initio* energies are superimposed as points on the curves obtained by the present vibronic coupling model. It can be seen that the model reproduces the *ab initio* data extremely well even in the vicinity of various curve crossings. These curve crossings develop into CIs in multidimensions. The energetic equilibrium minimum and minimum of the seam of various CIs of the PESs of Np$^+$ are estimated within a linear coupling model (see Appendix I for details) [22] and are listed in Table 5.6.

The energetic minimum of the seam of $\widetilde{X}$-$\widetilde{A}$, $\widetilde{A}$-$\widetilde{B}$ and $\widetilde{X}$-$\widetilde{B}$ CIs are found to occur at ~ 8.48 eV, ~ 10.11 eV and ~ 13.67 eV, respectively. The $\widetilde{X}$, $\widetilde{A}$ and $\widetilde{A}$, $\widetilde{B}$ states are vertically ~ 0.70 eV and ~ 1.27 eV apart, respectively. The minimum of the $\widetilde{X}$-$\widetilde{A}$ CIs occurs ≈ 0.1 eV above the minimum of the $\widetilde{A}$ state. This result is ≈ 1 kcal mol^{-1} higher than the *ab initio* CASSCF estimate and well within the CASPT2 results of Hall *et al.* [158]. The minimum of the $\widetilde{A}$-$\widetilde{B}$ CIs occurs at ≈ 1.72 eV and ≈ 0.48 eV above the minimum of the $\widetilde{A}$ and $\widetilde{B}$ states, respectively.
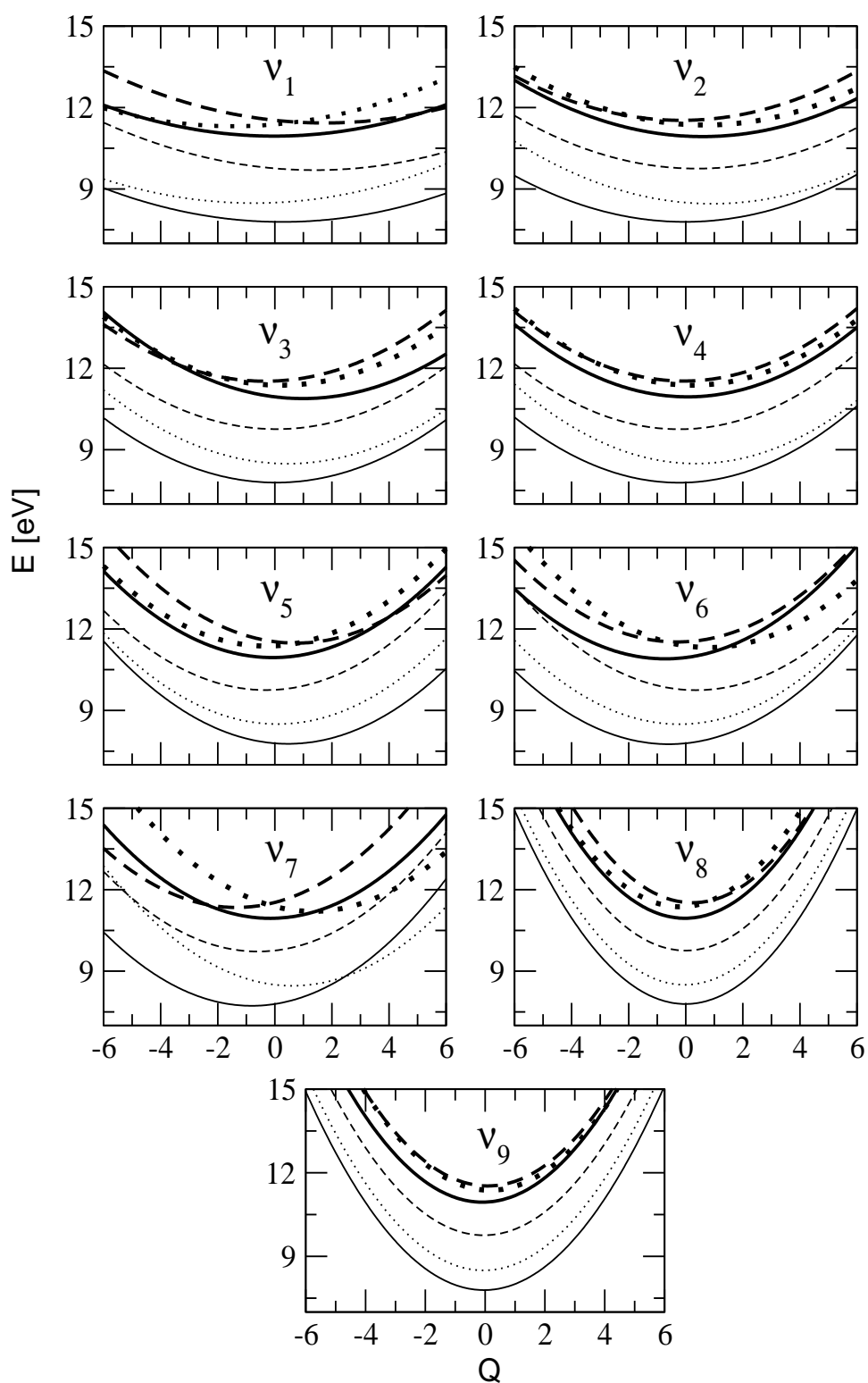
Figure 5.4: Adiabatic potential energies of the $\widetilde{X}$ (thin line), $\widetilde{A}$ (thin dotted line), $\widetilde{B}$ (thin dashed line), $\widetilde{C}$ (thick line), $\widetilde{D}$ (thick dotted line) and $\widetilde{E}$ (thick dashed line) electronic states of Np^+ as a function of the dimensionless normal coordinates of the totally symmetric (a_g) vibrational modes, ν_1-ν_9.
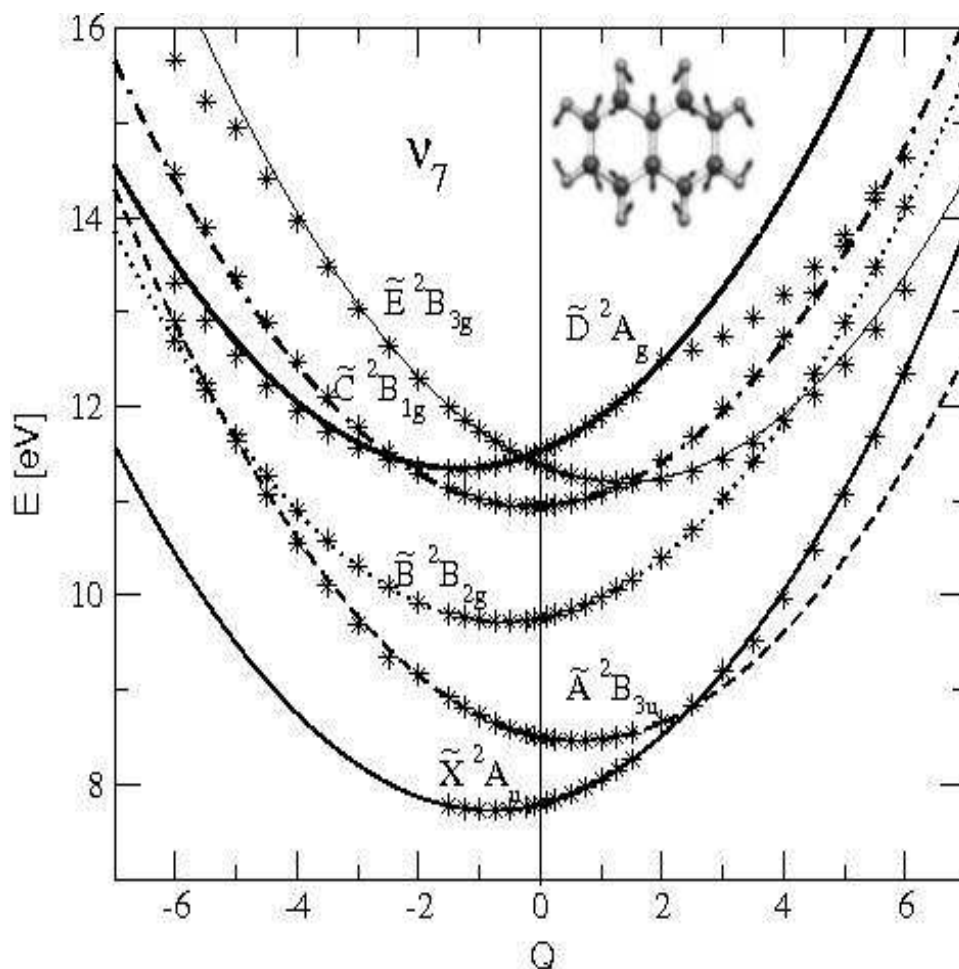
Figure 5.5: Adiabatic potential energy surfaces of the six low-lying electronic states of Np$^+$ along the vibrational modes ν_7. A sketch of the vibrational mode is also shown. The potential energy surfaces are obtained with the quadratic vibronic coupling scheme. The computed *ab initio* potential energies of these states are superimposed and shown by the points on each curve. The equilibrium geometry of Np in its electronic ground state ($\widetilde{X}^1 A_g$) corresponds to $\mathbf{Q} = 0$.

Table 5. 6. Equilibrium minimum (diagonal entries) and minimum of the seam of various CIs (off-diagonal entries) of the potential energy surfaces of Np^+. All quantities are given in eV.

$$
\begin{pmatrix}
 & \widetilde{X} & \widetilde{A} & \widetilde{B} & \widetilde{C} & \widetilde{D} & \widetilde{E} \\
\widetilde{X} & - & 8.48 & 13.67 & 25.25 & 14.38 & 16.89 \\
\widetilde{A} & & 8.37 & 10.11 & 20.94 & 14.02 & 13.50 \\
\widetilde{B} & & & 9.63 & 11.64 & 11.34 & 12.07 \\
\widetilde{C} & & & & 10.82 & 11.08 & 11.18 \\
\widetilde{D} & & & & & 11.02 & 11.44 \\
\widetilde{E} & & & & & & 11.17
\end{pmatrix}
$$

Hall *et al.* [158] obtained the latter number at ≈ 1.0 eV in the CASSCF and similar to our value in their CASPT2 treatment. The minimum of the $\widetilde{X}$-$\widetilde{B}$ CIs occurs at ≈ 4.0 eV above the minimum of the $\widetilde{B}$ state. The $\widetilde{B}$-$\widetilde{C}$ and $\widetilde{B}$-$\widetilde{D}$ CIs occur at much higher energies (not seen in Fig. 5.5) and expected to have no impact on the dynamics of $\widetilde{C}$ and $\widetilde{D}$ electronic states. Interestingly, $\widetilde{B}$-$\widetilde{E}$ CIs occur at ~ 0.9 eV above the $\widetilde{E}$ state minimum. As mentioned before, the $\widetilde{C}$, $\widetilde{D}$ and $\widetilde{E}$ electronic states are very close in energy. The $\widetilde{C}$-$\widetilde{D}$ CIs occur at ~ 0.06 eV above the minimum of $\widetilde{D}$ state.

Similarly, the $\widetilde{D}$-$\widetilde{E}$ CIs occur at ~ 0.17 eV above the minimum of the $\widetilde{D}$ state. The seam minimum of $\widetilde{C}$-$\widetilde{E}$ CIs (~ 11.18 eV) almost coincides with the minimum of $\widetilde{E}$ state (~ 11.17 eV). The $\widetilde{D}$ and $\widetilde{E}$ states resemble well known Jahn-Teller effect where their crossing occur very near the equilibrium geometry ($\mathbf{Q} = 0$) (cf., Fig. 5.5). The mentioned various CIs among these electronic states open up complex pathways for the nuclear motion on them. The effect of the low-energy CIs in the vibronic bands and excited state relaxation dynamics of Np^+ are

discussed in relevance to the astrophysical observations in the next section.

5.3.2 Vibronic band structures of electronic states of Np$^+$

5.3.2.1 $\widetilde{X}$, $\widetilde{A}$, $\widetilde{B}$, $\widetilde{C}$, $\widetilde{D}$ and $\widetilde{E}$ uncoupled state spectrum

The uncoupled state spectrum for the $\widetilde{X}$, $\widetilde{A}$, $\widetilde{B}$, $\widetilde{C}$, $\widetilde{D}$ and $\widetilde{E}$ electronic states of Np$^+$ is calculated by the matrix diagonalization approach using the Lanczos algorithm. The results are shown in Figs. 5.6-5.11 . The theoretical stick spectra for the $\widetilde{X}$ (Fig. 5.6), $\widetilde{A}$ (Fig. 5.7), $\widetilde{B}$ (Fig. 5.8), $\widetilde{C}$ (Fig. 5.9), $\widetilde{D}$ (Fig. 5.10) and $\widetilde{E}$ (Fig. 5.11) electronic states are calculated using 7 totally symmetric vibrational modes (ν_1-ν_7) within a linear as well as quadratic vibronic coupling model. The vibrational basis of harmonic oscillator functions, dimension of secular matrix and number of Lanczos iterations used to obtain converged theoretical data are given in Table 5.7. The spectral envelopes are generated by convoluting the theoretical stick data with a Lorentzian line shape function of 20 meV full width at the half maximum (FWHM).

The vibrational modes ν_6 and ν_7 form the dominant progression in the $\widetilde{X}$ state. The peaks are ~ 0.183 eV and ~ 0.2035 eV spaced in energy and correspond to the vibrational frequencies of these modes. The peak spacings of ~ 0.0632 eV, ~ 0.0968 eV and ~ 0.2064 eV corresponding to the excitation of ν_1, ν_2 and ν_7 vibrational modes, respectively, are observed in the $\widetilde{A}$ state. A dominant progression of ν_1, ν_5, ν_6, and ν_7 in the $\widetilde{B}$ state is found with the corresponding peak spacings ~ 0.0643, ~ 0.1852, ~ 0.1874 and ~ 0.2019 eV, respectively. It is also found that the vibrational modes ν_2, ν_3 and ν_6 in the $\widetilde{C}$, ν_1 and ν_7 in the $\widetilde{D}$ and ν_1 and ν_3 in the $\widetilde{E}$ state form the detectable progressions.

The vibrational structures of the uncoupled $\widetilde{X}$ and $\widetilde{B}$ electronic states reveal close resemblance with the experimental results [148, 149]. This is because the minimum of CIs are located at energies well above the location of the FC zone centers of the $\widetilde{X}$ and $\widetilde{B}$ states. The vibrational spectrum of the uncoupled $\widetilde{A}$
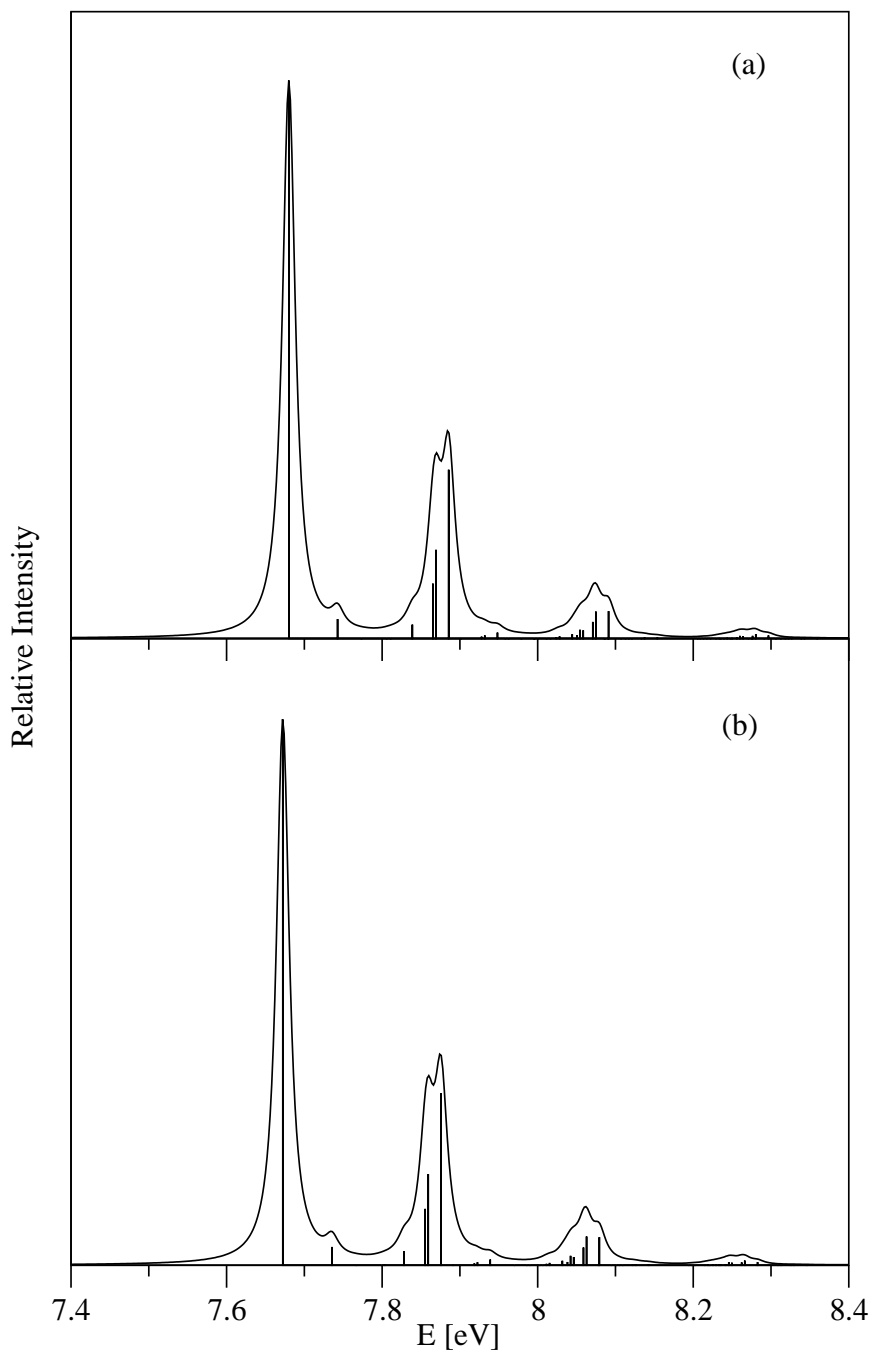
Figure 5.6: The uncoupled vibronic band of the $\widetilde{X}$ electronic state of Np^+ computed with relevant seven a_{1g} (ν_1-ν_7) vibrational modes within the linear (panel a) and quadratic (panel b) vibronic coupling scheme. The theoretical stick spectrum in each panel is convoluted with a Lorentzian function of 20 meV FWHM to calculate the spectral envelope.
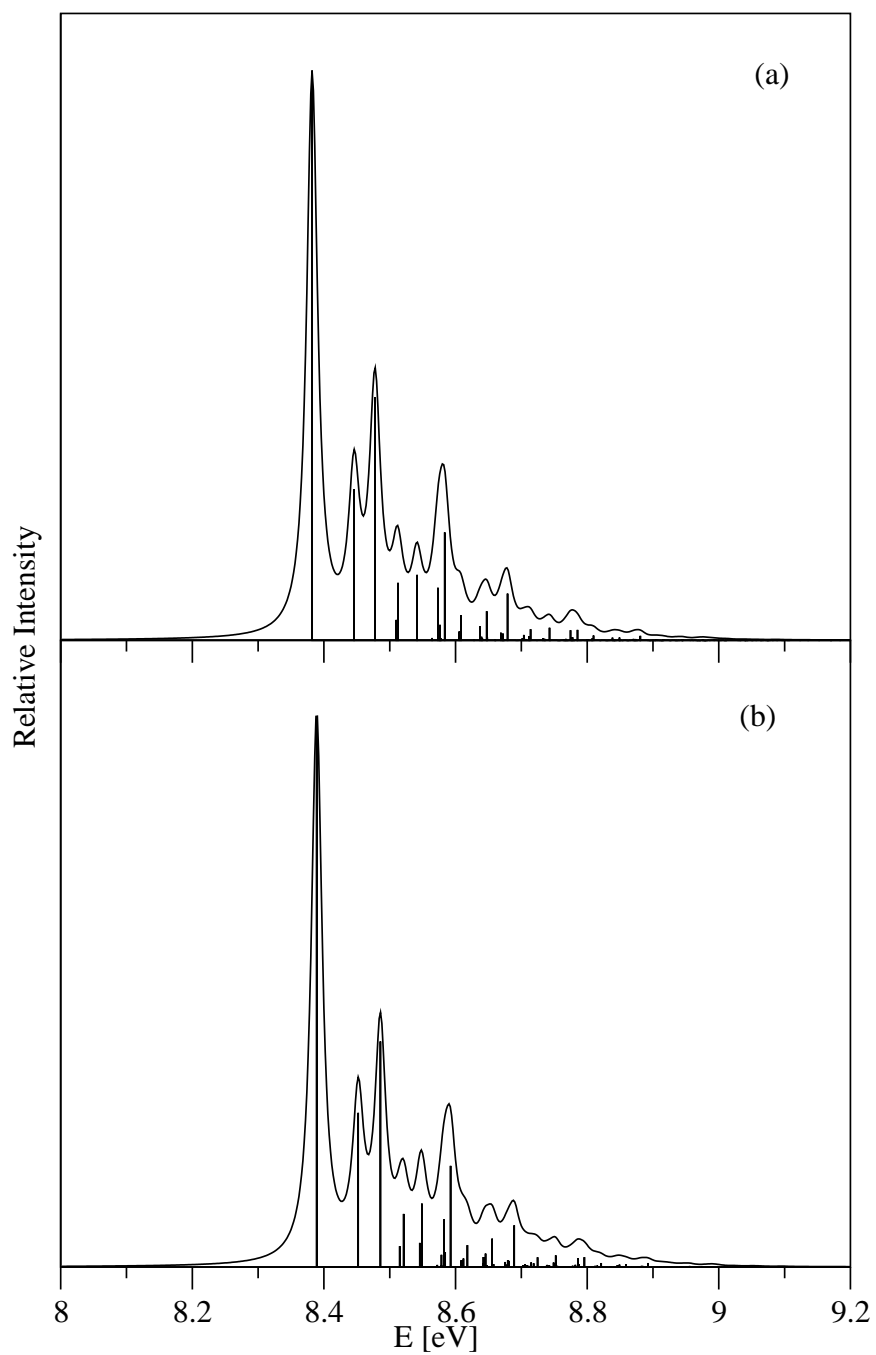
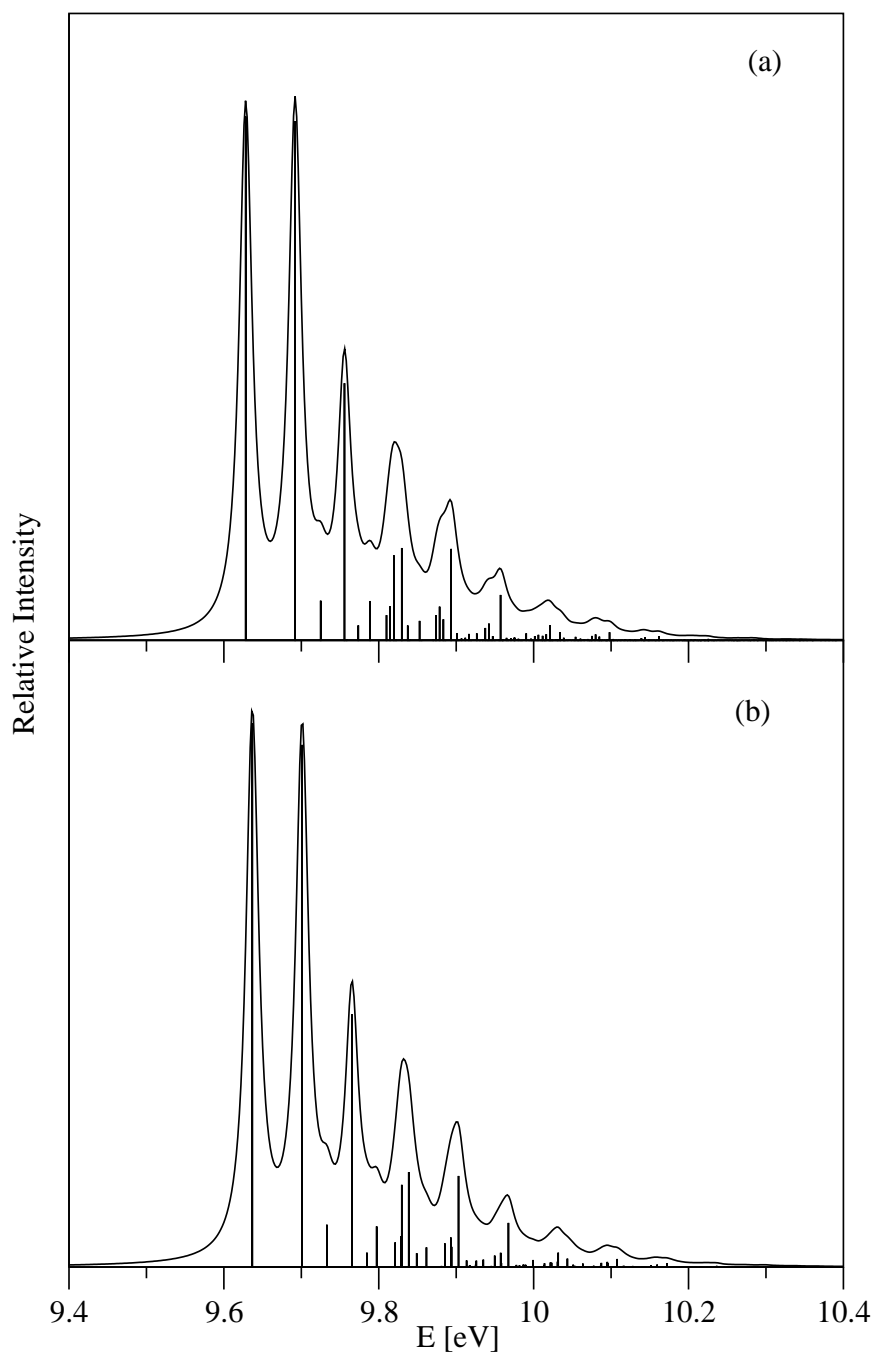Figure 5.7: Same as in Fig. 5.6 shown for the uncoupled vibronic band of $\widetilde{A}$ state of Np^+.

Figure 5.8: Same as in Fig. 5.6 shown for the uncoupled vibronic band of $\widetilde{B}$ state of Np$^+$.
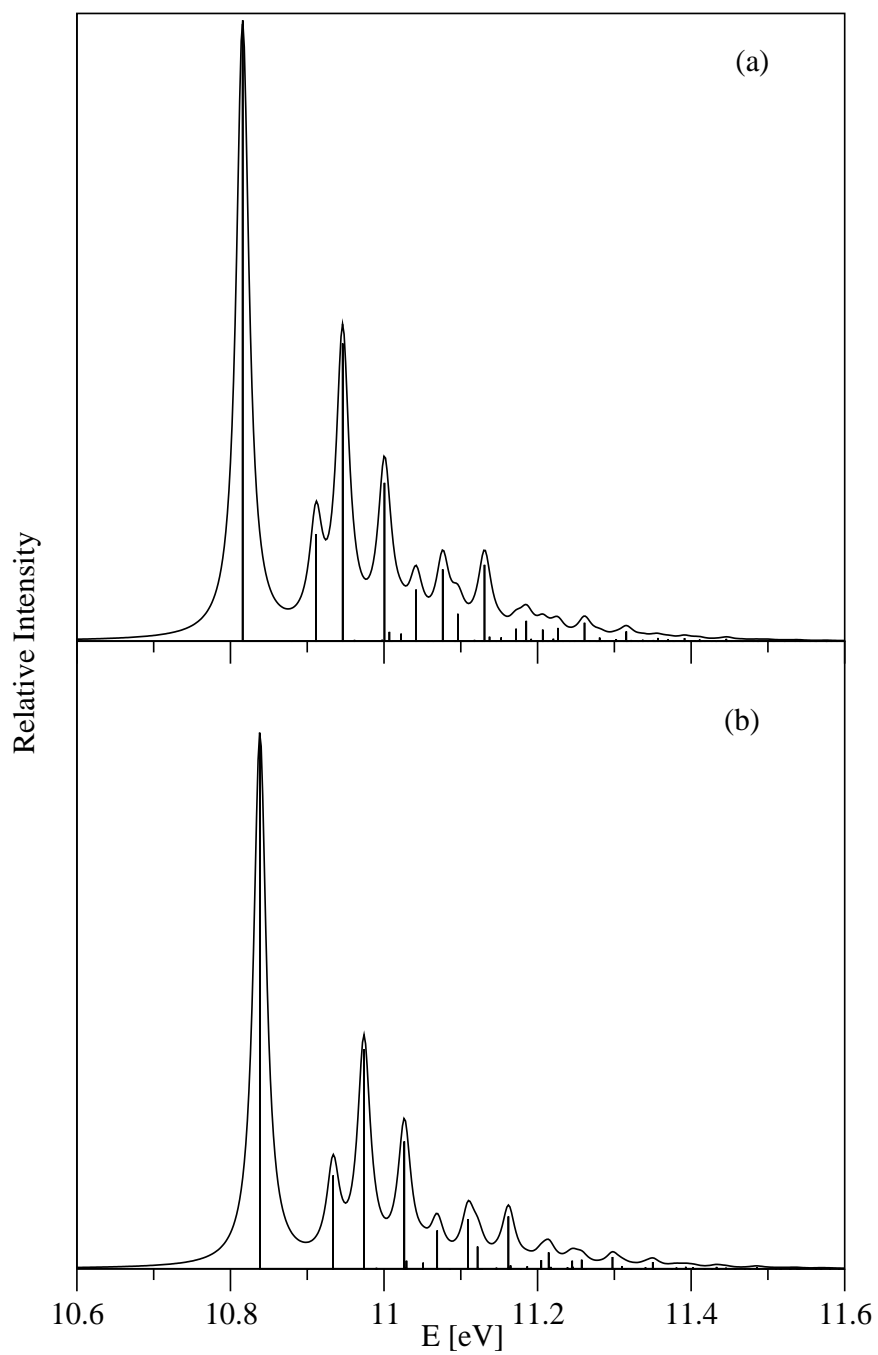
Figure 5.9: Same as in Fig. 5.6 shown for the uncoupled vibronic band of $\widetilde{C}$ state of Np^+.
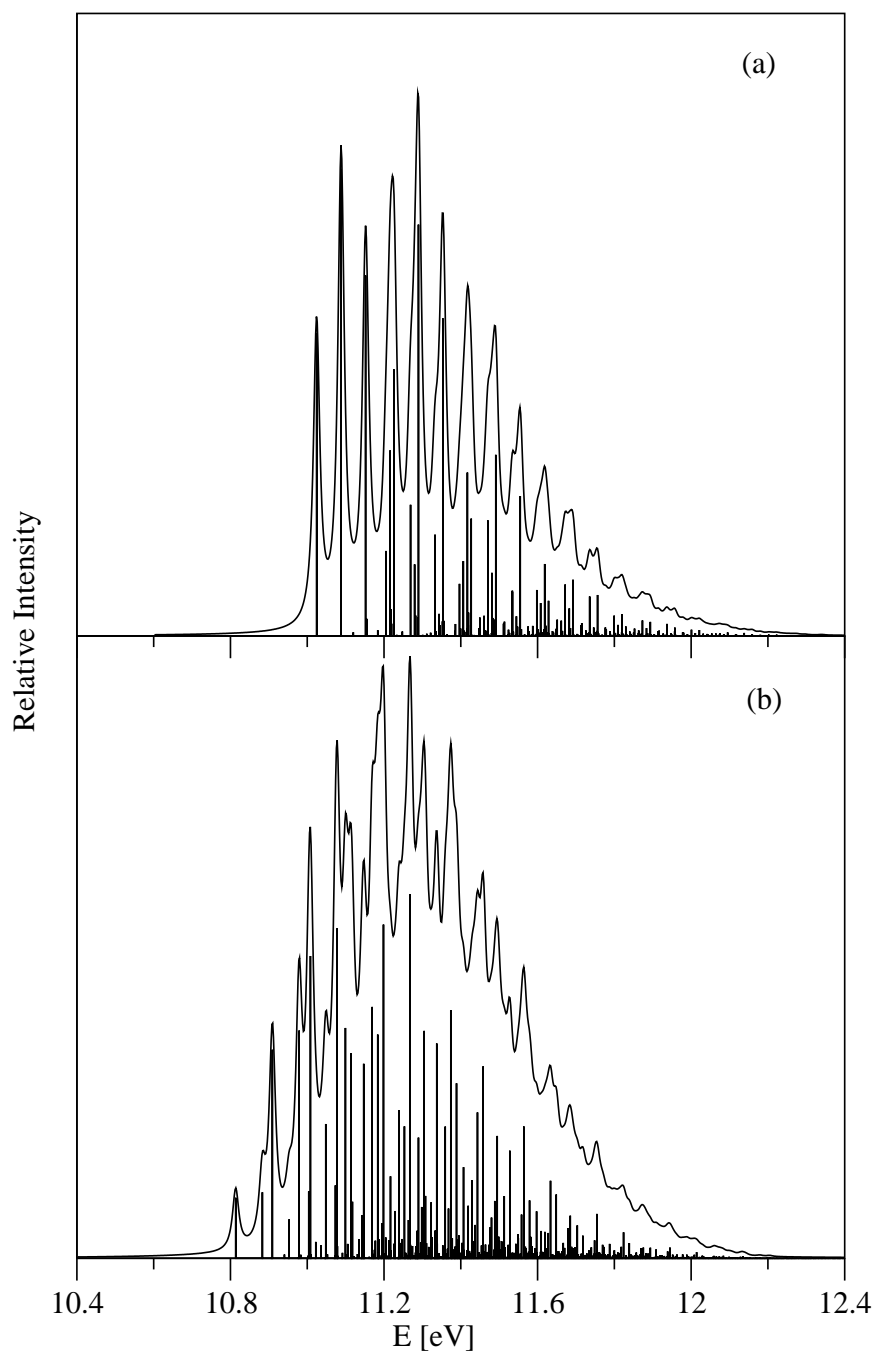
Figure 5.10: Same as in Fig. 5.6 shown for the uncoupled vibronic band of $\widetilde{D}$ state of Np^+.
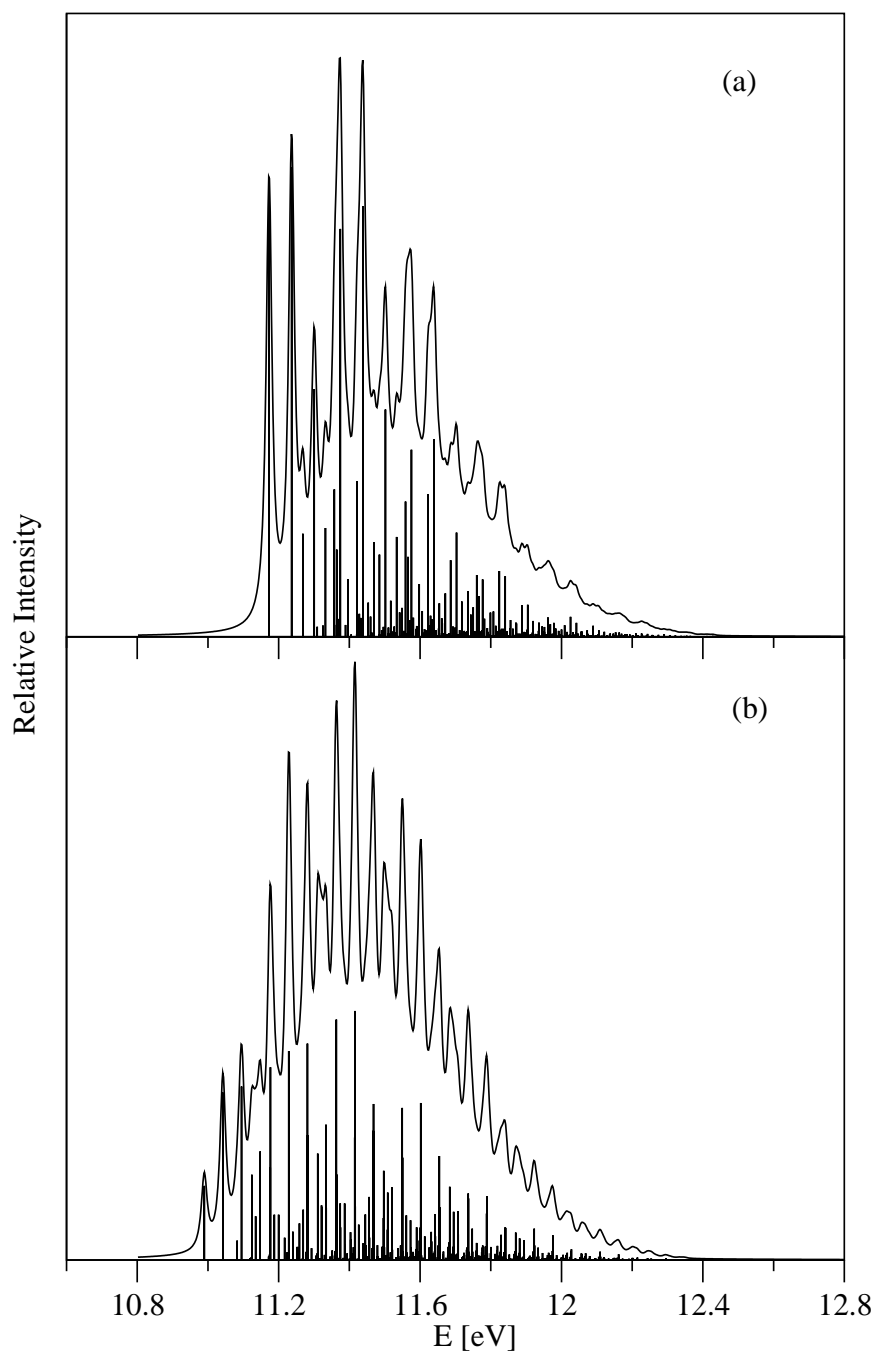
Figure 5.11: Same as in Fig. 5.6 shown for the uncoupled vibronic band of $\widetilde{E}$ state of Np^+.

Table 5.7

The number of harmonic oscillator (HO) basis functions along each vibrational mode, the dimension of the secular matrix and the number of Lanczos iterations used to calculate the converged theoretical stick spectrum shown in Figs. 5.6 - 5.11.

							Dimension of the secular matrix	No. of Lanczos iterations	Figure(s)
		No. of HO basis functions							
ν_1	ν_2	ν_3	ν_4	ν_5	ν_6	ν_7			
4	2	2	2	12	18	33	228096	5000	5.6
8	16	4	4	6	4	8	393216	5000	5.7
20	3	3	3	3	3	5	24300	5000	5.8
2	6	16	2	2	8	2	12288	5000	5.9
30	4	4	4	20	2	24	1843200	5000	5.10
32	17	2	2	2	16	17	1183744	5000	5.11

state reveals resolved vibrational structures whereas, it is found to be broad and structureless in the experiment [148,149]. The coupling of $\widetilde{A}$ particularly, with $\widetilde{X}$ appears to be extremely important in this case. Similarly, the vibrational structures of the uncoupled $\widetilde{C}$, $\widetilde{D}$ and $\widetilde{E}$ electronic states are well resolved whereas, complex and overlapping bands for these states found in the experimental measurements [148, 149]. This is due to the fact that these electronic states are very close in energy and their seam of CIs occur within the FC zone. This is expected to have profound effect on the vibrational structure of these states. In order to understand the observed experimental vibronic structures, possible interstate coupling parameters need be considered. Such a dynamical simulation using the matrix diagonalization approach can no longer be carried out because of a huge increase in the electronic and nuclear degrees of freedom. A WP propagation approach within the MCTDH framework [109] is undertaken below to accomplish the goal.

5.3.2.2 Vibronic spectrum of coupled $\widetilde{X}$-$\widetilde{A}$-$\widetilde{B}$-$\widetilde{C}$-$\widetilde{D}$-$\widetilde{E}$ electronic states

In this section the $\widetilde{X}$-$\widetilde{A}$-$\widetilde{B}$-$\widetilde{C}$-$\widetilde{D}$-$\widetilde{E}$ vibronic spectrum is calculated by including coupling among these states and considering 29 most relevant vibrational modes. The MCTDH WP propagation approach [109] is used to calculate the spectrum and to study the mechanistic details of internal conversion process. In this approach five, five dimensional and one, four dimensional particles are constructed by judiciously combining the vibrational modes. The details of the basis set and mode combinations employed in the WP propagations using the MCTDH algorithm are given Table 5.8. The resulting six states vibronic spectrum is presented in Fig. 5.12 (bottom panel) along with the experimental results (top panel) of Ref. [149]. The former represent a combined results of six separate WP propagations for six possible initial transitions to the $\widetilde{X}$, $\widetilde{A}$, $\widetilde{B}$, $\widetilde{C}$, $\widetilde{D}$ and $\widetilde{E}$ electronic states. In each calculation, the WP is propagated up to 200 fs and the resulting time autocorrelation function is damped with an exponential function [exp (-t/τ_r); with τ_r = 66 fs] before Fourier transformation. This damping corresponds to a Lorentzian line shape function with 20 meV FWHM. While the vibronic structures of the $\widetilde{X}$ and $\widetilde{B}$ states in Fig. 5.12 remain almost same as the uncoupled state results, the vibronic structure of the $\widetilde{A}$ state is severely affected by the nonadiabatic coupling. This is due to the fact that the minimum of the seam of $\widetilde{X}$-$\widetilde{A}$ CIs is located only ~ 0.1 eV above the minimum of the $\widetilde{A}$ state and therefore the low-lying vibronic levels of the latter state are strongly perturbed. It can be seen that the overall broadening and the detail fine structures of this band are in perfect accord with the experiment. The complex vibronic structures of the overlapping $\widetilde{C}$-$\widetilde{D}$-$\widetilde{E}$ electronic manifold are also in very good accord with the experiment [149]. The energetic minimum of these electronic states occurs in the vicinity of the minimum of the seam of various CIs within the $\widetilde{C}$-$\widetilde{D}$-$\widetilde{E}$ electronic states (cf., Table 5.6). The associated nonadiabatic coupling causes a strong mixing of their vibrational levels and as a result the vibronic bands become
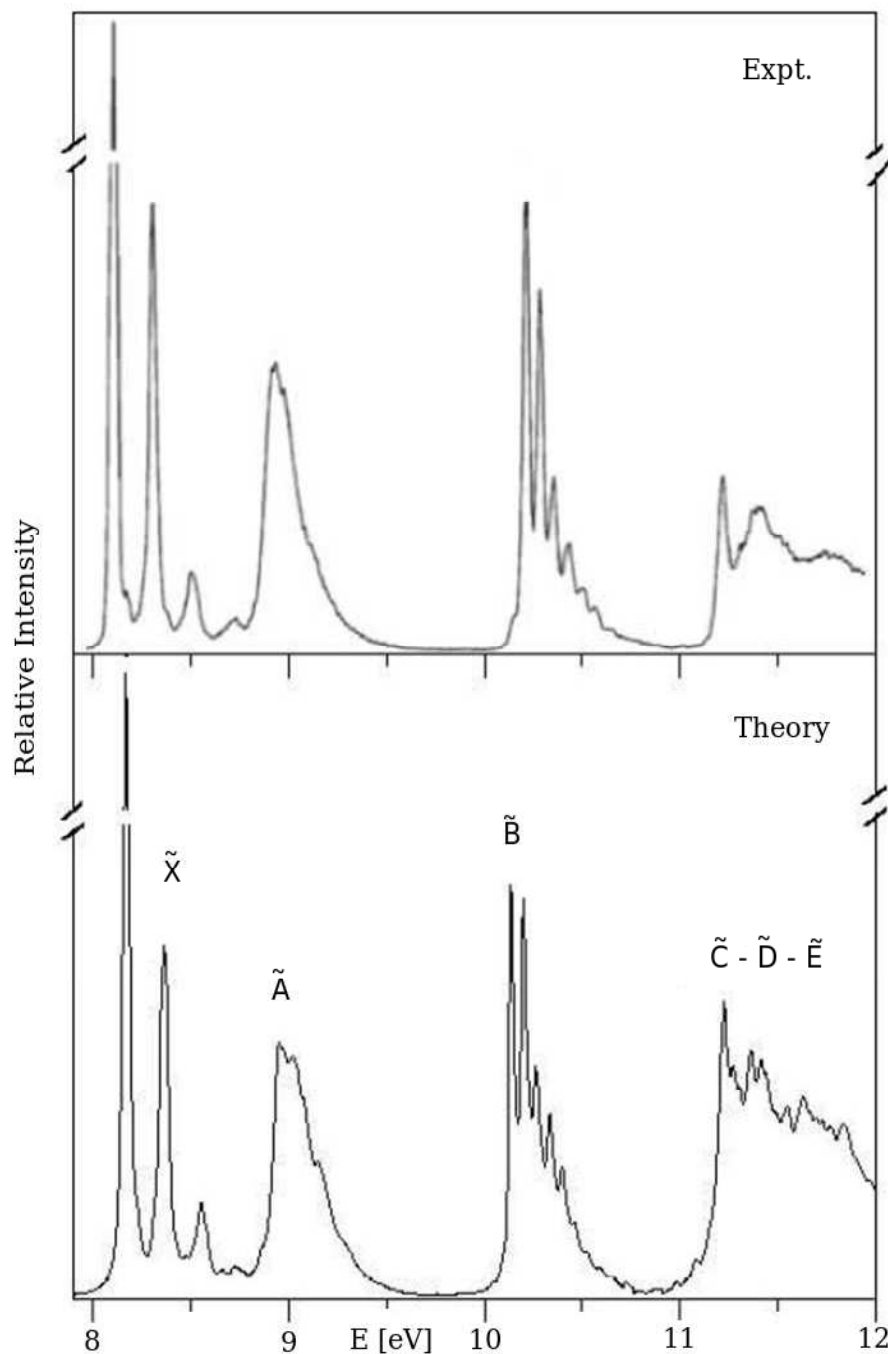
Figure 5.12: The photoelectron spectrum of the coupled $\widetilde{X}$-$\widetilde{A}$-$\widetilde{B}$-$\widetilde{C}$-$\widetilde{D}$-$\widetilde{E}$ electronic states of Np$^+$. The experimental (reproduced from Ref [149]) and the present theoretical results are shown in the top and bottom panels, respectively. The intensity (in arbitrary units) is plotted along the energy (measured relative to electronic ground state ($\widetilde{X}^1 A_g$) of Np) of the final vibronic states.

Table 5.8

Number of basis functions for the primitive as well as the single particle basis used in the MCTDH calculations.

Normal modes	Primitive basis[a]	SPF basis[b] $[\widetilde{X}, \widetilde{A}, \widetilde{B}, \widetilde{C}, \widetilde{D}, \widetilde{E}]$
$(\nu_1,\nu_{17},\nu_2,\nu_{14},\nu_{19})$	(10, 5, 5, 7, 6)	[6, 7, 5, 6, 5, 6]
$(\nu_5,\nu_{26},\nu_{18},\nu_{37},\nu_{45})$	(4, 6, 6, 5, 15)	[7, 5, 7, 5, 6, 6]
$(\nu_{11},\nu_{16},\nu_{32},\nu_4,\nu_{41})$	(6, 4, 7, 4, 6)	[6, 5, 6, 6, 7, 5]
$(\nu_{27},\nu_{28},\nu_{39},\nu_{34})$	(6, 5, 5, 5)	[5, 5, 6, 7, 5, 6]
$(\nu_6,\nu_{29},\nu_{22},\nu_{42},\nu_8)$	(5, 4, 6, 5, 8)	[6, 6, 7, 6, 5, 6]
$(\nu_7,\nu_3,\nu_{12},\nu_{25},\nu_{46})$	(5, 4, 5, 8, 6)	[7, 6, 5, 6, 5, 6]

[a]The primitive basis is the number of Harmonic oscillator DVR functions, in the dimensionless coordinate system required to represent the system dynamics along the relevant mode. The primitive basis for each particle is the product of the one-dimensional bases; e.g for particle 1 in the set given for Fig. 5.12 the primitive basis contains $10 \times 5 \times 5 \times 7 \times 6 = 10500$ functions and the full primitive basis consists of a total of 7.9009×10^{21} functions. [b] The SPF basis is the number of single-particle functions used.

highly overlapping and complex. The larger widths of the vibronic peaks reported in the gas phase electronic absorption spectra of $\widetilde{C}$ state can be attributed to the associated nonadiabatic effects in the $\widetilde{C}$-$\widetilde{D}$-$\widetilde{E}$ electronic manifold. It is difficult to decipher the vibrational progression in this situation as compared to the resolved vibronic structures of $\widetilde{B}$ state.

5.3.3 Time-dependent Dynamics

The time-dependent populations of the six diabatic electronic states of Np$^+$ in the coupled state dynamics of section 5.3.2.2 are shown in Figs 5.13. The results obtained by initially populating the $\widetilde{X}$, $\widetilde{A}$, $\widetilde{B}$, $\widetilde{C}$, $\widetilde{D}$ and $\widetilde{E}$ electronic states are shown in panels a-f, respectively. The six electronic populations are indicated

by six different line types in panel a. It can be seen from Fig. 5.13(a) that the populations of all the five excited states are very small when the dynamics is initially started in the $\widetilde{X}$ state. This is due to the fact that the CIs with the $\widetilde{X}$ state are located at higher energies which are not accessible to the WP during the short time dynamics of this state. This results into the observed sharp vibrational level structure of the $\widetilde{X}$ band .

A rapid transfer of $\widetilde{A}$ state population to the $\widetilde{X}$ state can be seen in panel (b). Within ~ 25 fs, 90% of the population transfers to the $\widetilde{X}$ state through the $\widetilde{X}$-$\widetilde{A}$ CIs. This is due to the fact that the minimum of the seam of $\widetilde{X}$-$\widetilde{A}$ CIs located only ≈ 0.02 eV above the equilibrium minimum of the $\widetilde{A}$ state. An initial decay of ~ 29 fs is estimated from an exponential fit to the diabatic population of the $\widetilde{A}$ state. The faster relaxation of the $\widetilde{A}$ state is in par with the observed broadening of this band. This supports the observed lack of fluorescence emission from this state [153] and photostability of Np$^+$. A very minor population transfer to the remaining electronic states ($\widetilde{B}$, $\widetilde{C}$, $\widetilde{D}$ and $\widetilde{E}$) indicate that the dynamics of $\widetilde{A}$ state is not affected by these excited states.

The diabatic populations of the six electronic states are shown in panel (c) by initially launching the WP in the $\widetilde{B}$ state. The population of $\widetilde{B}$ state decays to $\sim$ 0.5 within 100 fs and remains unchanged during the entire course of propagation time. A rise in the population of $\widetilde{A}$ and $\widetilde{X}$ state as time increases indicates that the population transfer occurs through $\widetilde{A}$-$\widetilde{B}$ and $\widetilde{X}$-$\widetilde{A}$ CIs. In this case also the remaining excited ($\widetilde{C}$, $\widetilde{D}$ and $\widetilde{E}$) states do not effect the dynamics of the $\widetilde{B}$ state. A decay rate of ≈ 217 fs is derived from an exponential fit to the population curve. This estimate is in excellent agreement with the experimental data [58, 153].

Quite unusual phenomenon can be seen when the initial WP propagated on $\widetilde{C}$ electronic state. The $\widetilde{C}$ state population rapidly decays to ~ 0.3 within ~ 25 fs. A major portion of population transfers to the $\widetilde{D}$ state and a minor portion transfers to the $\widetilde{B}$ state. As mentioned before, the minimum of $\widetilde{C}$-$\widetilde{D}$ CIs occur at ~ 0.06 eV above the minimum of $\widetilde{D}$ state and the $\widetilde{C}$ state population flows to the
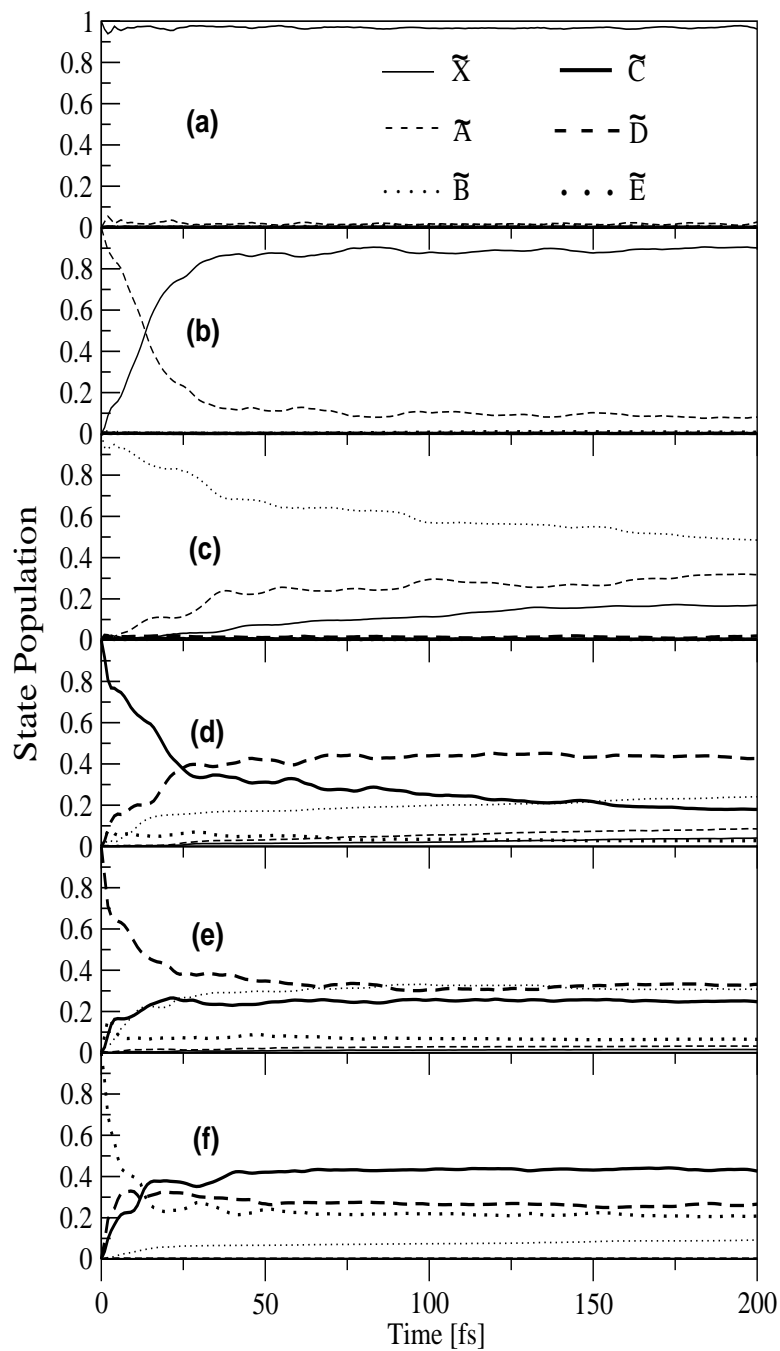
Figure 5.13: The populations (diabatic) in time of the $\widetilde{X}$ (thin lines), $\widetilde{A}$ (thin dashed lines), $\widetilde{B}$ (thin dotted lines), $\widetilde{C}$ (thick line), $\widetilde{D}$ (thick dashed lines) and $\widetilde{E}$ (thick dotted lines) states for an initial transition of the WP to the $\widetilde{A}$ (panel a), $\widetilde{B}$ (panel b), $\widetilde{C}$ (pane c), $\widetilde{D}$ (panel d) and $\widetilde{E}$ (panel e) in the coupled $\widetilde{X}$-$\widetilde{A}$-$\widetilde{B}$-$\widetilde{C}$-$\widetilde{D}$-$\widetilde{E}$ states dynamics of Np$^+$.
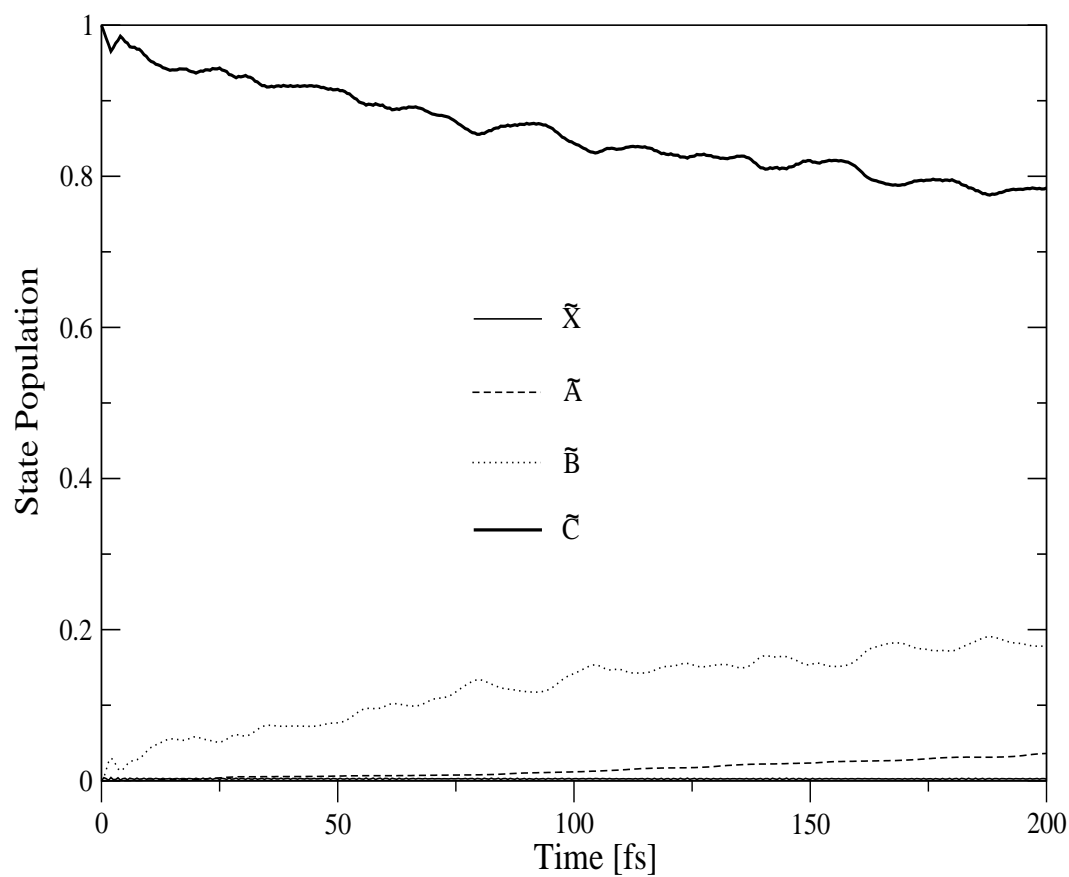
Figure 5.14: The diabatic electronic populations in time of the $\widetilde{X}$ (thin lines), $\widetilde{A}$ (thin dashed lines), $\widetilde{B}$ (thin dotted lines) and $\widetilde{C}$ (thick line) states for an initial transition of the WP to the $\widetilde{C}$ state in the coupled $\widetilde{X}$-$\widetilde{A}$-$\widetilde{B}$-$\widetilde{C}$ states dynamics of Np^+.

$\widetilde{D}$ state through these CIs. As propagation time increases the population of $\widetilde{D}$ state also increases and reaches to ~ 0.4 and remains unchanged for the rest of the propagation time. An estimated decay rate of ~ 60 fs is in excellent agreement with the value ~ 58 fs ($\sim 1.7\text{x}10^{13}$ s^{-1}) estimated from electronic absorption experiment [57]. Further calculations are performed to confirm the role of $\widetilde{D}$ state in the dynamics of $\widetilde{C}$ state. A coupled states dynamical calculation considering only $\widetilde{X}$, $\widetilde{A}$, $\widetilde{B}$ and $\widetilde{C}$ states is performed by launching the WP initially on the $\widetilde{C}$ state. The experimental vibronic structures of $\widetilde{X}$, $\widetilde{A}$ and $\widetilde{B}$ bands are reproduced accurately. The diabatic electronic populations obtained in this case are shown in Fig. 5.14. It is clear from the figure that the $\widetilde{C}$ state population decays very slowly (compared to that of $\widetilde{X}$-$\widetilde{A}$-$\widetilde{B}$-$\widetilde{C}$-$\widetilde{D}$-$\widetilde{E}$ coupled state dynamics) which relates to a much longer life time of this state. This indicates the importance of the $\widetilde{D}$ state in the intramolecular relaxation dynamics of the $\widetilde{C}$ state.

In the panel (e), we show the electronic populations of the six electronic states when the initial WP launched on the $\widetilde{D}$ state. Within ~ 25 fs the $\widetilde{D}$ state population sharply decays and the $\widetilde{C}$ state population rises simultaneously. As already mentioned above that the energetic minimum of the $\widetilde{C}$ state occurs at $\sim$ 0.06 above the minimum of the $\widetilde{C}$-$\widetilde{D}$ CIs, and the $\widetilde{D}$ state population flows to the $\widetilde{C}$ state via these CIs. Similarly the minimum of the $\widetilde{B}$-$\widetilde{D}$ CIs occurs at ~ 0.32 eV above the $\widetilde{D}$ state minimum. Due to this the population of $\widetilde{B}$ state increases to ~ 0.3 in ~ 25 fs and remains unchanged for the rest of the propagation time. A substantial portion of population also flows to the $\widetilde{E}$ state via the $\widetilde{D}$-$\widetilde{E}$ CIs. In case of dynamics of $\widetilde{E}$ state (panel f), half of the population transfers to the lower electronic states within ~ 15 fs via the $\widetilde{C}$-$\widetilde{D}$-$\widetilde{E}$ CIs. Nonradiative decay rates of ~ 29 and 15 fs are estimated for the $\widetilde{D}$ and $\widetilde{E}$ states, respectively.

5.3.4 Vibronic dynamics of $\widetilde{B}$ state: Astrophysical relevance

The vibrational energy level structures of the $\widetilde{B}$ band of Np^+ has been critically examined in laboratory measurements in relevance to the astrophysical DIBs [54, 56–58]. The vibrational progression of the D_2 $(\widetilde{B}) \leftarrow D_0$ $(\widetilde{X})$ electronic transition of Np^+ (reproduced from Ref. [58]) is shown in Fig. 5.3. The obtained four strong absorption peaks are attributed to the progression of two totally symmetric vibrational modes and a sub-picosecond life time (≈ 212 fs) is estimated from the observed broadening of the peaks [58]. The position and width of the peaks obtained from the laboratory measurements are utilized to assign the three new DIBs discovered by astronomers [59].

The simulation of vibronic structures of uncoupled $\widetilde{B}$ band is already presented in Sec. 5.3.2.1. Here, we performed several reduced dimensional calculations via a time-independent matrix diagonalization method [22] to examine the effects of $\widetilde{X}$-$\widetilde{B}$, $\widetilde{A}$-$\widetilde{B}$ and $\widetilde{B}$-$\widetilde{C}$ couplings on the broadening of the $\widetilde{B}$ band. The coupled state spectrum of $\widetilde{X}$-$\widetilde{B}$ (panel b), $\widetilde{A}$-$\widetilde{B}$ (panel c), $\widetilde{B}$-$\widetilde{C}$ (panel d) and $\widetilde{X}$-$\widetilde{A}$-$\widetilde{B}$-$\widetilde{C}$-$\widetilde{D}$-$\widetilde{E}$ (cf., Sec 5.3.2.2) (panel e) is shown in Fig. 5.15 along with the experimental photoelectron band [149]. While the $\widetilde{X}$-$\widetilde{B}$ and $\widetilde{B}$-$\widetilde{C}$ couplings do not have much effects, the $\widetilde{A}$-$\widetilde{B}$ coupling (cf., panel c) causes clustering of vibronic lines starting from the origin of the band.

The theoretical coupled $\widetilde{A}$-$\widetilde{B}$ state spectrum is obtained by including six totally symmetric (ν_1, ν_2, ν_4, ν_5, ν_6 and ν_7) and four nontotally symmetric (ν_{18}, ν_{20}, ν_{21} and ν_{22}) vibrational modes selected depending on their coupling strength (cf., Tables 5.1 and 5.2). A secular matrix of dimension 22,39,488 obtained by using 12, 6, 2, 3, 4, 4, 6, 3, 3 and 6 harmonic oscillator basis functions (in that order) is diagonalized employing 5000 Lanczos iterations. The spectral envelope is calculated by convoluting the stick spectrum by a Lorentzian function of 20 meV FWHM. The dominant progressions in the theoretical band are formed by
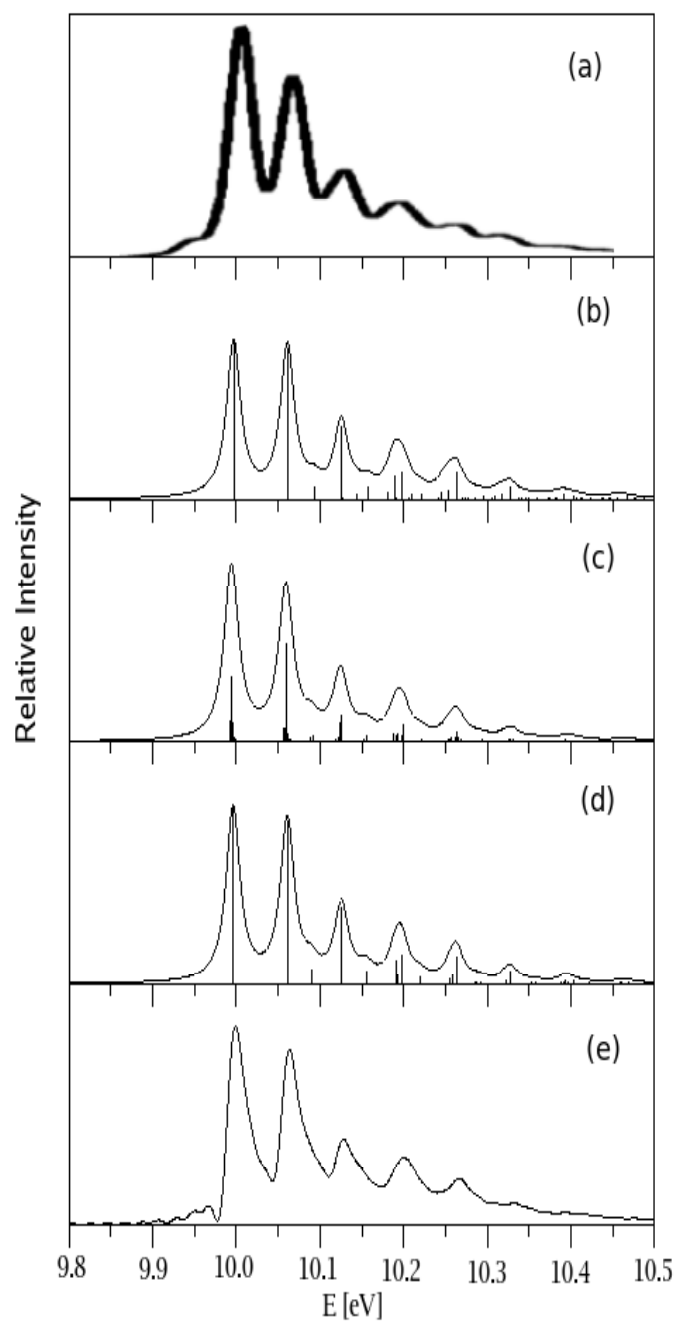
Figure 5.15: The photoelectron spectrum of the $\widetilde{B}$ state of Np^+. The experimental spectrum (reproduced from Ref. [149] is shown in panel (a). The coupled state spectrum of $\widetilde{X}$-$\widetilde{B}$ (b), $\widetilde{A}$-$\widetilde{B}$ (c), $\widetilde{B}$-$\widetilde{C}$ (d) and $\widetilde{X}$-$\widetilde{A}$-$\widetilde{B}$-$\widetilde{C}$-$\widetilde{D}$-$\widetilde{E}$ (e) is also shown.

Table II. Calculated vibronic energy levels of the $\widetilde{B}^2 B_{2g}$ state of Np^+ along with the various experimental results. Energies are given in nm.

Theory (present)	DIBs [59]	a	b	c	d
670.69 (0-0 peak)	670.74	670.69	670.70	670.65	674.1
648.15	648.87	648.93	648.89	648.84	652.0
637.49	-	638.57	-	-	-
-	-	634.72	-	-	-
627.07	-	628.50	-	-	-
617.09	-	617.34	-	-	-
609.87	611.80	612.48	612.52	-	615.1
607.55	-	609.27	-	-	-
-	-	597.33	-	-	-
591.17	-	593.40	593.35	-	596.5
588.78	-	591.36	-	-	-
582.29	-	585.27	-	-	-

a - Pino *et al.* [127]

b - Bienner *et al.* [58]

c - Romanini *et al.* [56]

d - Salama *et al.* [54]

the totally symmetric vibrational modes same as in the case of uncoupled $\widetilde{B}$ state spectrum. The excitation of nontotally symmetric vibrations is induced by $\widetilde{A}$-$\widetilde{B}$ coupling and results into a broadening of each peak. The energetic locations of vibronic lines of Fig. 15.15(c), compiled in Table 5.9, are in good accord with the data from laboratory and astronomical measurements [54, 56, 58, 59, 127]. In compiling the data the origin band is placed at 690.90 nm. It can be seen from Table 5.9 that the present theoretical data are in very good accord with the astronomical observations of the three new DIBs and also with the laboratory experiments. A decreasing intensity pattern with increasing energy as noted in the spectrum of star Cernis 52 also follows from Fig. 15.5. To this end, it is gratifying to state that the present theoretical results unambiguously support the assignments of the three new DIBs to the electronic transitions in Np^{+}. This also convincingly adds to the present consensus and hypothesis that the PAH radical cations are potential carriers of DIBs.

5.4 Summary and Outlook

The vibronic energy level spectrum and dynamics of six low-lying electronic states of Np^{+} are theoretically studied. A model vibronic Hamiltonian constructed in a diabatic electronic basis and the Hamiltonian parameters are computed *ab initio* . The nuclear dynamical simulations are carried out by time-independent and time-dependent approaches. The theoretical results are in excellent agreement with both experimental and astrophysical findings.

The $\widetilde{X}$, $\widetilde{A}$, $\widetilde{B}$, $\widetilde{C}$, $\widetilde{D}$ and $\widetilde{E}$ electronic states of Np^{+} are close in energy at the vertical configuration and possible low-energy CIs are established. The uncoupled state spectrum of these states is calculated by time-independent approach utilizing matrix diagonalization method and resolved band structures are obtained for all these states. The $\widetilde{X}$-$\widetilde{A}$-$\widetilde{B}$-$\widetilde{C}$-$\widetilde{D}$-$\widetilde{E}$ coupled state spectrum is calculated in-

cluding relevant 29 vibrational degrees of freedom by a WP propagation method. The theoretical results are excellent agreement with the experiment. The observed broadening of $\widetilde{A}$ band is attributed to the vibronic coupling of $\widetilde{A}$ state with $\widetilde{X}$ state. The vibronic structures of the $\widetilde{A}$ state are strongly affected by $\widetilde{X}$-$\widetilde{A}$ CIs leading to the broadening of the $\widetilde{A}$ band. The complex vibronic structures of the $\widetilde{C}$-$\widetilde{D}$-$\widetilde{E}$ electronic states are also accurately reproduced. Nonradiative decay rates of ~ 20, ~ 217, ~ 60, ~ 29 and ~ 15 fs are estimated for the $\widetilde{A}$, $\widetilde{B}$, $\widetilde{C}$, $\widetilde{D}$ and $\widetilde{E}$ electronic states, respectively.

Reduced dimensional calculations are also carried out on the vibronic spectrum of the $\widetilde{B}$ state including $\widetilde{X}$-$\widetilde{B}$, $\widetilde{A}$-$\widetilde{B}$ and $\widetilde{B}$-$\widetilde{C}$ coupling. The theoretical results revealed that the $\widetilde{X}$-$\widetilde{B}$ and $\widetilde{B}$-$\widetilde{C}$ coupling do not have much impact on the nuclear dynamics of $\widetilde{B}$, whereas the $\widetilde{A}$-$\widetilde{B}$ coupling induces the excitation of nontotally symmetric modes leading to the broadening of the vibrational peaks of the $\widetilde{B}$ state.

Finally, we have attempted to unravel some contentious issues of interstellar physics based on the dynamical results of the six-low lying electronic states of Np^+. The outcome unambiguously reveals the latter as potential DIB carriers and a nonradiative deactivation of its excited electronic states is mediated by numerous complex nonadiabatic paths which establishes the mechanism of its photostability. The theoretical results presented here complement for the first time the observations by the astronomers as well as laboratory experimentalists. The present study is hoped to trigger further experimental and theoretical research in this area in future.

Chapter 6

Summary and Outlook

A detailed description of the photoinduced dynamics of the low-lying electronic states of radical and radical cation of aromatic hydrocarbons is presented in this thesis. The intricate coupling of electronic states through nuclear vibrations is discussed in particular, and its consequence in spectroscopy and nonradiative decay of electronically excited molecular systems is delineated. The basic concept of vibronic coupling leading to the conical intersections of electronic states is discussed. The theoretical treatment of vibronic coupling employing state-of-the art quantum chemistry and first principles quantum dynamical methods is discussed at length.

The complexity in the assignment of electronic spectra of polyatomic molecules is addressed by showing recent results on three representative examples viz., $C_6H_5^{\bullet}$, PA^+ and Np^+. Dynamical observable like the rich vibronic spectrum is calculated and assigned. The mechanistic details of the ultrafast nonradiative dynamics of the excited states is studied. These observables are compared with the available experimental data to validate the established theoretical model. The discussions in this thesis reveal the need of understanding the complex vibronic coupling mechanisms while dealing with the electronically excited molecules in particular, and the recent advancements in the experimental and theoretical techniques to observe and treat them.

The main findings of the present work are given below.

1. (a) The vibronic structure of the photodetachment band of the $\widetilde{X}^2 A_1$ state of $C_6H_5^\bullet$ revealed resolved vibrational progressions observed in the experiment. Two totally symmetric vibrational modes of ring deformation type (ν_1 and ν_2) form the major progressions in this band. The existing ambiguity in the assignment of these progressions in the experimental data is resolved.

(b) Despite some differences in the intensity of the individual lines, the rich vibronic structure observed in the experimental absorption spectrum is very well reproduced in our theoretical nuclear dynamical simulations of the uncoupled $\widetilde{A}^2 B_1$ state. The vibrational modes ν_1, ν_2 ν_3 and ν_5 from most of the progressions in this photodetachment band.

(c) In the uncoupled state results for the $\widetilde{B}^2 A_2$ electronic state of $C_6H_5^\bullet$ distinct progressions due to ν_1, ν_2 ν_3 and ν_6 vibrational modes are found.

(d) The energetic minimum of the $\widetilde{A}$ - $\widetilde{B}$ CIs occurs at ~ 3.29 eV which is located very near to the equilibrium minimum of the $\widetilde{B}$ state. The $\widetilde{A}$-$\widetilde{B}$ coupled state calculations were carried out by propagating WP using the MCTDH algorithm. It is found that the vibronic structures of the high-energy tail of the $\widetilde{A}$ band and the entire $\widetilde{B}$ band are severely affected by the nonadiabatic coupling. As a result the $\widetilde{B}$ band transforms to a broad and structureless envelope.

(e) An ultrafast nonradiative decay rate of ~ 30 fs for the $\widetilde{B}$ state is estimated from the decay of the electronic population in the coupled electronic manifold.

2. (a) The vibronic spectrum of coupled $\widetilde{X}^2 B_1$-$\widetilde{A}^2 A_2$-$\widetilde{B}^2 B_2$-$\widetilde{C}^2 B_1$ electronic states of PA$^+$ is calculated including the relevant 24 vibrational modes by employing the MCTDH WP propagation algorithm. The resulting spectrum is found to be in excellent accord with the broad band photoelectron spectroscopy results attesting the reliability of the present theoretical model.

(b) The vibrational energy level spectrum of the $\widetilde{X}$ and $\widetilde{C}$ states of PA$^+$ is simulated by performing reduced dimensional calculations employing a matrix

diagonalization approach. The precise locations of the vibrational levels are compared with the MATI spectrum of the $\widetilde{X}$ state and PIRI and photodissociation spectrum of the $\widetilde{C}$ state. Except for ν_{13} in the PIRI spectrum, excitations of all other totally symmetric modes are found to be in accord with the experimental data.

(c) Strong coupling between the $\widetilde{X}$ and $\widetilde{A}$ electronic states of PA^+ triggers weak excitations of the fundamentals of the nontotally symmetric b_2 vibrational modes in the MATI spectrum of the $\widetilde{X}$ state. Because of very weak coupling between the $\widetilde{A}$ and $\widetilde{C}$ electronic states, the weak excitations of the nontotally symmetric modes assigned in the PIRI spectrum are not observed.

(d) The $\widetilde{A}$ band is particularly very diffuse and broad and a nonradiative decay time of ~ 20 fs has been estimated for this state.

(e) The Nonadiabatic effects on the $\widetilde{B}$ band are relatively mild and therefore its photoelectron spectrum reveals resolved structures. A nonradiative decay rate of ~ 88 fs is estimated for the $\widetilde{B}$ state from the theoretical data, although experimentally it is predicted to be a long-lived state of PA^+.

3. (a) The photoelectron spectrum of the coupled $\widetilde{X}^2 A_u$-$\widetilde{A}^2 B_{3u}$-$\widetilde{B}^2 B_{2g}$-$\widetilde{C}^2 B_{1g}$-$\widetilde{D}^2 A_g$-$\widetilde{E}^2 B_{3g}$ electronic manifold of Np^+ is calculated by including 6 electronic states and 29 relevant vibrational degrees of freedom employing WP propagation approach. The theoretical results are in excellent agreement with the available experimental data.

(b) The strong nonadiabatic coupling between the $\widetilde{X}$ and $\widetilde{A}$ states of Np^+ leads to a broadening of the $\widetilde{A}$ band. A lifetime of ~ 25 fs is estimated for this state which supports the observed lack of fluorescence emission from this state and photostability of Np^+.

(c) The $\widetilde{A}$-$\widetilde{B}$ coupling leads to a clustering of the vibronic lines starting from the origin of the $\widetilde{B}$ band and thereby causes a broadening of each peak. Distinct progressions of two totally symmetric vibrational modes (~ 514 cm^{-1} and $\sim$

1458 cm^{-1}) are found. The energetic locations and peak widths of the vibronic lines are in excellent accord with the data from laboratory and astronomical measurements.

(d) The $\widetilde{C}$, $\widetilde{D}$ and $\widetilde{E}$ electronic states of Np^{+} are very close in energy at the vertical configuration and lead to the formation of multiple CIs. Our theoretical analysis reveals that these CIs are responsible for the observed complex structure of $\widetilde{C}$-$\widetilde{D}$-$\widetilde{E}$ vibronic bands.

(e) The $\widetilde{C}$-$\widetilde{D}$ and $\widetilde{C}$-$\widetilde{E}$ CIs play crucial role in the nonradiative decay dynamics of the $\widetilde{C}$ state. A rapid population transfer occur via these CIs to the $\widetilde{D}$ and $\widetilde{E}$ electronic states during the initial WP propagating on the $\widetilde{C}$ state. A life time of ~ 60 fs of the $\widetilde{C}$ state, in excellent agreement with the experimental absorption spectroscopy results, is estimated from the theoretical results.

(f) Nonradiative decay rates of ~ 29 fs and ~ 15 fs are estimated for the $\widetilde{D}$ and $\widetilde{E}$ electronic states of Np^{+}, respectively.

(g) The present theoretical findings unambiguously qualify Np^{+} as potential DIB carrier and a nonradiative deactivation of the excited electronic states is mediated by numerous complex nonadiabatic paths, which establishes the mechanism of their photostability.

In conclusion, the role of intricate vibronic coupling in the photoinduced processes of radical and radical cations of aromatic hydrocarbons is examined by establishing model diabatic Hamiltonians. First principles nuclear dynamical simulations are carried out both within the time-independent and time-dependent frameworks. Our findings very accurately reproduce the vibronic structures of the low-lying electronic states and the time scale of their nonradiative decay. The results, therefore, clearly vindicate the utmost importance of electronic nonadiabatic interactions in the broad and diffuse nature of the observed vibronic bands, ultrafast nonradiative decay, low quantum yield of fluorescence and photostability of electronically excited aromatic hydrocarbons.

This study is further extended to the investigation of the photophysics of the radical cations of higher polyacenes of the PAH family. The laboratory electronic spectroscopy results revealed that the intramolecular dynamics of the low-lying electronic states of acenaphthylene ($C_{12}H_8$), acenaphthene ($C_{12}H_{10}$) and fluorene ($C_{13}H_{10}$) radical cations are dominated by the ultrafast internal conversion mechanism [148, 160–163]. The energy separation between the $\widetilde{X}$ and $\widetilde{B}$ states in these cations is similar to Np^+ (~ 1.9 eV). The magnitude of the relevant vibrational frequencies in these cations are also similar to those of Np^+. Therefore, electronic transitions in these cations might be responsible for some of the DIBs observed in the spectra of reddened stars. Investigation of the vibrational progression of the $\widetilde{B} \leftarrow \widetilde{X}$ electronic transition is of prime interest.

However, study of the dynamics of the systems with the large number of vibrational degrees of freedom (as in the present case) is a daunting task. Apparently not all the vibrational degrees of freedom contribute to the dynamics and the most relevant degrees of freedom are selected judiciously. The previous experience (in the case of PA^+ and Np^+) shows that the within the quadratic vibronic coupling model the dynamical observables are accurately reproduced. Within this implicit considerations, the dynamics of the larger system can be treated successfully. In case any heteroatom is involved, the quadratic vibronic coupling model is inadequate and further higher order couplings to be considered for better comparison with the experimental data [34, 35].

The findings of the present work also expected to initiate study in the experimental, observational and theoretical fields of interstellar chemistry and physics of aromatic hydrocarbons. As these molecules are the precursors of the important complex biological compounds i.e, amino acids, their photoinduced reactions are to be investigated in greater details to understand the origin and evolution of life in the universe. Evidence of prebiotic molecules present in the comets and meteorites suggest possible connection between life on earth and interstellar space. A study on origin of life in space provides insights into the life on earth.

Appendix A

Adiabatic potential energy surfaces and conical intersections

The concept of adiabatic potential energy surfaces (PESs) and CIs are important for the interpretation and understanding of the dynamical observable such as vibronic spectra and nonradiative decay rates of the electronic states. We shall consider a 2x2 diabatic Hamiltonian containing M tuning modes (totally symmetric, Q_{gi}) and N coupling (non-totally symmetric, Q_{uj}) vibrational modes and is given as

$$
\mathcal{H} \;=\; (\mathcal{T}_N + \mathcal{V}_0)\mathbf{1} + \begin{pmatrix} E_1 + \sum_{i=1}^{N} \kappa_i^{(1)} Q_{gi} & \sum_{i=1}^{M} \lambda_j Q_{uj} \\ \sum_{i=1}^{M} \lambda_j Q_{uj} & E_2 + \sum_{i=1}^{N} \kappa_i^{(2)} Q_{gi} \end{pmatrix}, \quad (A.1a)
$$

Where

$$
\mathcal{T}_N \;=\; -\frac{1}{2}\sum_{i=1}^{N} \omega_i \left(\frac{\partial^2}{\partial Q_{gi}^2} \right) - \frac{1}{2}\sum_{j=1}^{M} \omega_j \left(\frac{\partial^2}{\partial Q_{uj}^2} \right), \quad (A.1b)
$$

is the nuclear kinetic energy operator and

$$
\mathcal{V}_0 \;=\; \frac{1}{2}\sum_{i=1}^{N} \omega_i Q_{gi}^2 + \frac{1}{2}\sum_{j=1}^{M} \omega_j Q_{uj}^2, \quad (A.1c)
$$

126

is the potential energy operator. The quantities κ and λ represents the intrastate and interstate coupling parameters. Here E_1 and E_2 (assuming $E_1 < E_2$) are the ionization of the coupled electronic states at the reference geometry $\mathbf{Q}=0$, where $\mathbf{Q}$ represents collectively (Q_g, Q_u). The adibatic PESs are obtained by diagonalizing the above Hamiltonian in the fixed-nuclei limit, $T_N \rightarrow 0$, as follows.

$$\mathbf{S}^\dagger(\mathcal{H} - T_N \mathbf{1})\mathbf{S} \;=\; V \tag{A.1d}$$

$$V \;=\; \begin{pmatrix} V_1(\mathbf{Q}) & 0 \\ 0 & V_2(\mathbf{Q}) \end{pmatrix} \tag{A.1e}$$

where $\mathbf{S}$ is an orthogonal matrix which describes the adiabatic to diabatic transformation. Here $V_1(\mathbf{Q})$ and $V_2(\mathbf{Q})$ are the adiabatic PESs of Hamiltonian (A. 1a).

For analysis of adiabatic PESs, it is convenient to write $\mathcal{H}$ of Eq. (A. 1a) in the following form:

$$\mathcal{H} \;=\; \mathcal{H}_0 + \begin{pmatrix} -d & c \\ c & d \end{pmatrix} \tag{A.1f}$$

where

$$\mathcal{H}_0 \;=\; \mathcal{T}_N + \mathcal{V}_0 + \Sigma + \sigma Q_g \tag{A.1g}$$

$$\Sigma \;=\; (E_1 + E_2)/2 \tag{A.1h}$$

$$\Delta \;=\; (E_2 - E_1)/2 \tag{A.1i}$$

$$\sigma_i \;=\; (\kappa_i^{(1)} + \kappa_i^{(2)})/2 \tag{A.1j}$$

$$\delta_i \;=\; (\kappa_i^{(2)} - \kappa_i^{(1)})/2 \tag{A.1k}$$

$$d \;=\; \Delta + \sum_{i=1}^{N} \delta_i Q_{gi} \tag{A.1l}$$

$$c \;=\; \sum_{i=} \lambda_j Q_{uj} \tag{A.1m}$$

The adibatic potentials are given by the expression within the linear vibronic coupling (LVC) model

$$V_{1,2}(\mathbf{Q}) \;=\; V_0(\mathbf{Q}) + \Sigma + \sum_{i=1}^{N} \sigma_i Q_{gi} \mp W \tag{A.1n}$$

$$W \;=\; \sqrt{d^2 + c^2} \tag{A.1o}$$

The conditions for the occurance of CIs between $V_1(\mathbf{Q})$ and $V_2(\mathbf{Q})$ are simply $d = 0$ and $c = 0$. These conditions define a hypersurface of dimension $N + M - 2$ in the $N + M$ dimensional coordinate space i.e. in order to exhibit degeneracy of PESs, two independent set of nuclear coordinates are required.

The minimum of the seam of CIs is given by

$$V_{min}^{(c)} \;=\; \Sigma + \frac{(F - \Delta)^2}{2D} - \frac{1}{2} \sum_{i=1}^{N} \sigma_i^2 / w_{gi} \tag{A.2}$$

The position of the minimum in the space of the tuning mode is

$$(Q_{gi}^{(c)})_{min} \;=\; \frac{(\delta_i/\omega_{gi})(F-\Delta)}{D} - \frac{\sigma_i}{w_{gi}}, \quad i = 1, ..., N \tag{A.3}$$

The minimum of the seam of the CIs relative to the minimum of the upper adiabatic PES is given by

$$V_{min}^{(c)} - (V_2)_{min} \;=\; \frac{1}{2D}(\Delta - D - F)^2 \tag{A.4}$$

where

$$D \;=\; \sum_{i=1}^{N} \frac{\delta_i^2}{w_{gi}} \tag{A.5}$$

$$F \;=\; \sum_{i=1}^{N} \frac{\delta_i \sigma_i}{w_{gi}} \tag{A.6}$$

Bibliography

[1] M. Born and R. Oppenheimer, Ann. Phys. (Leipzig) **84**, 457 (1927).

[2] H. A. Jahn and E. Teller, Proc. Roy. Soc. London, Ser. A **161**, 220 (1937).

[3] E. Teller, J. Phys. Chem. **41**, 109 (1937).

[4] G. Herzberg and H. C. Longuet-Higgins, Discuss. Faraday. Soc. **35**, 77 (1963).

[5] J. von Neumann and E. P. Wigner, Physik. Z. **30**, 467 (1929).

[6] T. Carrington, Acc. Chem. Res. **7**, 20 (1974).

[7] S. Mahapatra, Acc. Chem. Res. **42**, 1004 (2009).

[8] R. Renner, Z. Phys. **92**, 172 (1934).

[9] *Conical Intersections: Electronic Structure, Dynamics and Spectroscopy*, edited by W. Domcke, D. R. Yarkony, and H. Köppel (WorldScientific, Singapore, 2004).

[10] S. Mahapatra, H. Köppel, L. S. Cederbaum, J. Chem. Phys. **110**, 5691 (1999).

[11] J. Michl and V. Bonacic-Koutecky, *Electronic Aspects of Organic Photochemistry* (Wiley, New York, 1990).

[12] M. A. Robb, F. Bernardi, and M. Olivucci, Pure and Appl. Chem. **67**, 783 (1995).

[13] F. Bernardi, M. Olivucci, and M. A. Robb, Chem. Soc. Rev. **25**, 321 (1996).

[14] *Conical intersections in photochemistry, spectroscopy and chemical dynamics*, Chem. Phys. **259**, 121-337 (2000).

[15] G. J. Atchity, S. S. Xantheas, K. Ruedenberg, J. Chem. Phys. **95**, 1862 (1991).

[16] A. Migani and M. Olivucci, Chapter 6, In; *Conical Intersections: Electronic Structure, Dynamics and Spectroscopy*, edited by W. Domcke, D. R. Yarkony, and H. Köppel (WorldScientific, Singapore, 2004).

[17] M. J. Paterson, M. A. Robb, L. Blancafort and A. D. DeBellis, J. Phys. Chem. A **109**, 7527 (2006).

[18] T. Carrington, Discuss. Faraday. Soc. **53**, 27 (1972).

[19] C. A. Mead and D. G. Truhlar, J. Chem. Phys. **70**, 2284 (1979).

[20] M. Desouter-Lecomte, C. Galloy, J. C. Lorquet, and M. Vaz Pires, J. Chem. Phys. **71**, 3661 (1979).

[21] I. B. Bersuker *The Jahn-Teller Effect and Vibronic Interactions in Modern Chemistry* (Plenum Press, New York, 1984).

[22] H. Köppel, W. Domcke, and L. S. Cederbaum, Adv. Chem. Phys. **57**, 59 (1984).

[23] G. Fischer, *Vibronic Coupling* (Academic Press, London, 1984).

[24] I. B. Bersuker and V. Z. Polinger, *Vibronic Interactions in Molecules and Crystals* (Springer-Verlag, Berlin, 1989).

[25] W. Domcke and G. Stock, Adv. Chem. Phys. **100**, 1 (1997).

[26] B. Jayachander Rao and S. Mahapatra, J. Chem. Phys. **127**, 244307 (2007).

[27] S. Ghosal and S. Mahapatra, J. Phys. Chem. A. **109**, 1530 (2005).

[28] R. Padmanaban and S. Mahapatra, J. Chem. Phys. **120**, 1746 (2004).

[29] B. Jayachander Rao, *Doctoral Thesis*, University of Hyderabad, Hyderabad, 2009.

[30] S. Mahapatra, G. A. Worth, H. -D. Meyer, L. S. Cederbaum and H. Köppel, J. Phys. Chem. A **105**, 5567 (2001).

[31] S. Mahapatra, V. Vallet, C. Woywod, H. Köppel and W. Domcke, J. Chem. Phys. **123**, 231103 (2005).

[32] T. S. Venkatesan and S. Mahapatra, J. Chem. Phys. **123**, 114308 (2005).

[33] T. S. Venkatesan, S. Mahapatra, H. Köppel and L. S. Cederbaum , J. Mol. Struct. **838**, 100 (2007).

[34] T. Mondal and S. Mahapatra, J. Phys. Chem. A, **112**, 8215 (2008).

[35] S. Faraji, H. Köppel, W. Eisfeld and S. Mahapatra, Chem. Phys. **347**, 110 (2008).

[36] Z. Lan, V. Vallet, A. L. Sobolewski, S. Mahapatra and W. Domcke, J. Chem. Phys. **122**, 224315(1-13) (2005).

[37] V. Vallet, Z. Lan, S. Mahapatra, A. L. Sobolewski and W. Domcke, Faraday. Discuss. **127**, 283 (2004).

[38] S. Perun, A. L. Sobolewski and W. Domcke, J. Phys. Chem. A **110**, 13238 (2006).

[39] S. Perun, A. L. Sobolewski and W. Domcke, Mol. Phys. **104**, 1113 (2006).

[40] A. L. Sobolewski, W. Domcke, Europhysics News. **37**, 20 (2006)

[41] H. Köppel, W. Domcke and L. S. Cederbaum, J. Chem. Phys. **74**, 2945 (1981).

[42] X. Gao, J. Essex-Lopresti, S. Munro, M. P. Hall, D. J. Smith, and R. Grice, J. Phys. Chem. A **102**, 1912 (1998).

[43] H. E. Sheng-Gui, E. J. Corey and C. J. Dennis, J. Chem. Phys. **119**, 2047 (2003).

[44] S. Mishra, W. Domcke, and L. V. Poluyanov, Chem. Phys. Lett. **446**, 256 (2007).

[45] I. Sioutis, S. Mishra, L. V. Poluyanov, and W. Domcke, J. Chem. Phys. **128**, 124318 (2008).

[46] A. Léger and J. L. Puget, Astron. Astrophys. **137**, L5 (1984).

[47] M. K. Craford, A. G. G. M. Tielesn and L. J. Allamandola, Astrophys. J. **293**, L45 (1985).

[48] A. Léger and L. d'Hendecourt, Astron. Astrophys. **146**, 76 (1985).

[49] W. H. Smith, T. P. Snow and D. G. York, Astrophys. J. **218**, 124 (1977).

[50] F. C. Gillett, W. J. forrest and K. M. Merril, Astrophys. J. **183**, 87 (1973).

[51] K. Sellgren, Astrophys. J. **277**, 623 (1984).

[52] L. J. Allamandola, A. G. G. M. Tielens and J. R. BarkerK, Astrophys. J. Suppl. **71**, 733 (1989).

[53] J. L. Puget and A. Léger, Annu. Rev. Astron. Astrophys. **27**, 161 (1989).

[54] F. Salama and L. J. Allamandola, J. Chem. Phys. **94**, 6964 (1991).

[55] P. Bréchignac and T. Pino, Astron. Astrophys. **343**, 49 (1999).

[56] D. Romanini, L. Biennier, F. Salama and L. J. Allamandola, and F. Stoeckel, Chem. Phys. Lett. **303**, 165 (1999).

[57] T. Pino, N. Boudin and P. Bréchignac, J. Chem. Phys. **111**, 7337 (1999).

[58] L. Biennier, F. Salama, L. J. Allamandola and J. J. Scherer, J. Chem. Phys. **118**, 7863 (2003).

[59] S. Iglesias-Groth, A. Manchado, D. A. García-Hernández, J. I. González Hernández and D. L. Lambert, Astrophys. J. **685**, L55 (2008).

[60] T. Allain, E. Sedlmayr and S. Leach, Astrophys. Space. Sci. **224**, 417 (1995).

[61] A. Goeres, Rev. Modern Astron. **6**, 165 (1993).

[62] K. Schroeter, D. Schröder and H. Schwarz, J. Phys. Chem. A. **103**, 4174 (1999).

[63] T. Allain, S. Leach and E. Sedlmayr, Astron. Astrophys. **305**, 602 (1996).

[64] W. J. van der Hart, Int. J. Mass Spectrom. **214**, 269 (2002).

[65] G. Granucci, Y. Ellinger and P. Boissel, Chem. Phys. **191**, 165 (1995).

[66] F. Jolibois, A. Klotz, F. X. Gadéa and C. Joblin, Astron. Astrophys. **444**, 629 (2005).

[67] D. K. Bohme, Chem. Rev. **92**, 1487 (1992).

[68] M. P. Bernstein, J. P. Dworkin, S. A. Sandford and L. J. Allamandola, Adv. Space Res. **30**, 1501 (2002).

[69] Y. -J. Chen, M. Nuevo, T. -S. Yih, W. -H, Ip, H. -S. Fung, C. -Y. Cheng, H. -R. Tsai and C. -Y. R. Wu, Mon. Not. R. Astron. Soc. **384**, 605 (2008).

[70] R. I. Kaiser, O. Asvanya and Y. T. Leea, Planet. Space Sci. **48**, 483 (2000).

[71] R. I. kaiser, L. Vereecken, J. Peeters, H. F. Bettinger, P. v. R. Schletyer and H. F. Schaefer III, Astron. Astrophys. **406**, 385 (2003).

[72] X. Gu, F. Zhang, Y. Guo and R. I. Kaiser, Angew. Chem. Int. Ed. **46**, 6866 (2007).

[73] X. Gu and R. I. kaiser, Acc. Chem. Res. **42**, 290 (2009).

[74] J. Cernicharo, A. M. Heras, A. G. G. M. Tielens, J. R. Pardo, F. Herpin, M. Guélin, and L. B. F. M. Waters, Astrophys. J. **546**, L123 (2001).

[75] E. Rüh1, S. D. Price and S. Leach, J. Phys. Chem. **93**, 6312 (1989).

[76] H. W. Jochims, H. Rasekh, E. Rüh1, H. Baumgärtel and S. Leach, Chem. Phys. **168**, 159 (1992).

[77] Y. Ling, J. M. L. Martin and C. Lifshitz, J. Phys. Chem. A **101**, 219 (1997).

[78] S. P. Ekern, A. G. Marshall, J. Szczepanski, and M. Vala, J. Phys. Chem. A **102**, 3498 (1998).

[79] N. Boudin, T. Pino and P. Bréchignac, J. Mol. Struct. **563**, 209 (2001).

[80] H. Xu, P. M. Johnson and T. J. Sears, J. Phys. Chem. A **110**, 7822 (2006).

[81] T. Pino, S. Douin, N. Boudin and P. Bréchignac, J. Phys. Chem. A **111**, 13358 (2007).

[82] R. Krishnamurthy, S. Epstein, J. Cronin, S. Pizzarello and G. Yuen, Geochim. Cosmochim. Acta. **56**, 4045 (1992).

[83] K. A. Kvenvolden, J. Lawless, K. Pering, E. Peterson, J. Flores, C. Ponnamperuma, I. R. Kaplan and C. Moore, Nature. **228**, 923 (1970).

[84] M. H. Engel and S. A. Macko, Nature. **389**, 265 (1997).

[85] J. R. Cronin and S. Pizzarello, Science. **275**, 951 (1997).

[86] J. R. Cronin and S. Pizzarello, Adv. Space Res. **23**, 293 (1999).

[87] M. Born and K. Haung: Dynamical Theory of Crystal Lattices. Oxford University Press, New York (1954).

[88] B. H. Lengsfield and D. R. Yarkony, Adv. Chem. Phys. **82**, 1 (1992).

[89] W. Lichten, Phys. Rev. **131**, 229 (1963).

[90] F. T. Smith, Phys. Rev. **179**, 111 (1969).

[91] T. F. O'Malley, Adv. At. Mol. Phys. **7**, 223 (1971).

[92] W. Domcke and G. Stock, Adv. Chem. Phys. **100**, 1 (1997).

[93] H. Köppel and W. Domcke: Encyclopedia of Computational Chemistry. In: Schleyer, P. v. R. (Ed.), Wiley, New York (1998).

[94] M. Baer, Chem. Phys. Lett. **35**, 112 (1975).

[95] C. A. Mead, D. G. Truhlar, J. Chem. Phys. **77**, 6090 (1982).

[96] M. Baer, Chem. Phys. **15**, 49 (1976).

[97] V. Sidis, Adv. Chem. Phys. **82**, 73 (1992).

[98] T. Pacher, L. S. Cederbaum and H. Köppel, Adv. Chem. Phys. **84**, 293 (1993).

[99] A. Thiel, H. Köppel, J. Chem. Phys. **110**, 9371 (1999).

[100] T. H. Dunning, Jr., J. Chem. Phys. **90**, 1007 (1989).

[101] M. J. Frisch, *et al.* Gaussian 03, Revision B. 05, Gaussian, Inc., Pittsburgh PA, 2003.

[102] L. S. Cederbaum and W. Domcke, Adv. Chem. Phys. **36**, 205 (1977).

[103] L. S. Cederbaum, J. Phys. B **8**, 290 (1975).

[104] J. Cullum and R. Willoughby, *Lanczos Algorithms for Large Symmetric Eigenvalue Problems* (Birkhäuser, Boston, 1985), Vols. I and II.

[105] W. Domcke, H. Köppel, and L. S. Cederbaum, Mol. Phys. **43**, 851 (1981).

[106] H. -D. Meyer, U. Manthe, L. S. Cederbaum, Chem. Phys. Lett. **165**, 73 (1990).

[107] U. Manthe, H. -D. Meyer, L. S. Cederbaum, J. Chem. Phys. **97**, 3199 (1992).

[108] B. H. Beck, A. Jäckle, G. A. Worth, H. -D. Meyer, Phys. Rep. **324**, 1 (2000).

[109] G. A. Worth, M. H. Beck, A. Jäckle, and H. -D. Meyer, The MCTDH Package, Version 8.2, (2000), University of Heidelberg, Germany. H. -D. Meyer, Version 8.3, (2002). See http://www.pci.uni-heidelberg.de/tc/usr/mctdh/

[110] R. F. Gunion, M. K. Gills, M. L. Polak and W.C.Lineberger, Int. J. Mass spectrom. Ion Processes. **117** 601 (1992).

[111] G. Porter and B. Ward, Proc. R. Soc. Lond. A **287**, 457 (1965).

[112] N. Ikeda, N. Nakashima, K. Yoshihara, J. Am. Chem. Soc. **97**, 3381 (1985).

[113] P. Hassanzadeh and J. H. Miller, J. Phys. Chem. **96**, 6570 (1992).

[114] J. H. Miller, L. Andrews, P. A. Lund and P. N. Schatz, J. Chem. Phys.**73**, 4932 (1980).

[115] W. G. Hatton, N. P. Hacker and P. H. Kaisa, J. Chem. Soc., Chem. Commun. 227 (1990).

[116] J. M. Engert and B. Dick, Appl. Phys. B. **63**, 5319 (1996).

[117] J. G. Radziszewski, Chem. Phys. Lett.. **301**, 565 (1999).

[118] B. Cercek and M. Kongshaug, J. Phys. Chem. **74**, 4319 (1970).

[119] J. Pacansky and D. W. Brown, J. Phys. Chem. **87**, 1553 (1983).

[120] R. P. Johnson, J. Org. Chem. **49**, 4857 (1984).

[121] M. Krauss and S. J. Roszak, J. Mol. Struct.(Theochem) **310**, 155 (1994).

[122] G. S. Kim, A. M. Mebel and S. H. Lin, Chem. Phys. Lett. **361**, 421 (2002).

[123] M. J. S. Dewar, W. C. Gardiner, Jr., M. Frenklach and I. Oref, J. Am. Chem. Soc. **109**, 4456 (1987).

[124] V. Engel, Chem. Phys. Lett. **189**, 76 (1992).

[125] J. W. Rabalais and R. J. Colton, J. Electron Spectrosc. Relat. Phenom. **1**, 83 (1972).

[126] D. L. Lichtenberger, S. K. Renshaw and R. M. Bullock, J. Am. Chem. Soc. **115**, 3276 (1993).

[127] P. Bréchignac, T. Pino and N. Boudin, Spectrochimica Acta Part A. **57**, 745 (2001).

[128] N. Boudin, T. Pino and P. Bréchignac, J. Mol. Struct. **563**, 209 (2001).

[129] Y. Y. Youn, C. H. Kwon, J. C. Choe and M. S. Kim, J. Chem. Phys. **117**, 2538 (2002).

[130] C. H. Kwon, H. L. Kim and M. S. Kim, J. Phys. Chem. A **107**, 10969 (2003).

[131] H. Xu, P. M. Johnson and T. J. Sears, J. Phys. Chem. A **110**, 7822 (2006).

[132] T. Pino, S. Douin, N. Boudin and P. Bréchignac, J. Phys. Chem. A **111**, 13358 (2007).

[133] E. B. Wilson Jr., J. C. Decius and P. C. Cross, *Molecular vibrations*, McGraw-Hill, New York, 1955.

[134] K. M. Singh, R. A. Singh and S. N. Thakur, Spectrochim. Acta **51A**, 269 (1995).

[135] J. M. Dyke, H. Ozeki, M. Takahashi, M. C. R. Cockett and K. Kimura, J. Chem. Phys. **97**, 8926 (1992).

[136] V. Sivaranjana Reddy and S. Mahapatra, J. Chem. Phys. **128**, 091104 (2008).

[137] E. Gindensperger, I. Bâldea, J. Franz and H. Köppel, Chem. Phys. **338**, 207 (2007).

[138] G. Bieri, L. Asbrink and W. von Niessen, J. Electron. Spectrosc. Relat. Phenom. **23**, 281 (1981).

[139] C. H. Kwon, H. L. Kim and M. S. Kim, J. Chem. Phys. **116**, 10361 (2002).

[140] M. Döscher, H. Köppel and P. G. Szalay, J. Chem. Phys. **117**, 2645 (2002).

[141] The Diffuse Interstellar Bands, eds. A. G. G. M. Tielens and T. P. Snow (Kluwer Academic, Dordrecht, 1995).

[142] F. Salama *et al.* , Astrophys. J. **526**, 265 (1999).

[143] J. H. D. Eland, C. J. Danby, Z. Naturforsch **23a**, 355 (1968).

[144] M. J. S. Dewar, S. D. Worley, J. Chem. Phys. **51**, 263 (1969).

[145] P. A. Clark, F. Brogli, E. Heilbronner, Helv. Chim. Acta **55**, 1415 (1972).

[146] E. Heilbronner, T. Hoshi, J. L. von Rosenberg, K. Hafner, Nouv. J. Chimie **1**, 105 (1976).

[147] E. Riihl, S. D. Price, S. Leach, J. Phys. Chem. **93**, 6312 (1989).

[148] T. Bally, C. Carra, M. P. Fülscher, Z. Zhu, J. Chem. Soc. Perkin Trans. **2**, 1759 (1998).

[149] D. A. da Silva Filho, R. Friedlein, V. Coropceanu, G. Öhrwall, W. Osikowicz, C. Suess, S. L. Sorensen, S. Svensson, W. R. Salaneck, J. Brédas, Chem. Commun. 1702-1703 (2004).

[150] R. S. Sánchez-Carrera, V. Coropceanu, D. A. da Silva Filho, R. Friedlein, W. Osikowicz, R. Murdey, C. Suess, W. R. Salaneck, J. Brédas, J. Chem .Phys. B. **110**, 18904 (2006).

[151] M. C. R. Cockett, H. Ozeki, K. Okuyama, K. Kimura, J. Chem. Phys. **98**, 7763 (1993).

[152] L. Andrews, B. J. Kelsall, T. A. Blankenship, J. Phys. Chem. **86**, 2916 (1982).

[153] L. Zhao, R. Lian, I. A. Shkrob, R. A. Crowell, S. Pommeret, E. L. Chronister, A. D. Liu, A. D. Trifunac, J. Phys. Chem. A. **108**, 25 (2004).

[154] J. Szczepanski, M. Vala, D. Talbi, O. Parisel and Y. Ellinger, J. Chem. Phys. **98**, 4494 (1993).

[155] F. Negri, M. Z. Zgierski, J. Chem. Phys. **100**, 1387 (1994).

[156] C. Neideralt, S. Grimme, S. D. Peyerimhoff, Chem. Phys. Lett. **245**, 455 (1995).

[157] T. Andruniow, M. Pawlikowski, Chem. Phys. **236**, 35 (1998).

[158] K. F. Hall, M. Boggio-Pasqua, M. J. Bearpark, M. A. Robb, J. Phys. Chem. A. **110**, 13591 (2006).

[159] L. Blancafort, F. Jolibois, M. Olivucci, M. A. Robb, J. Am. Chem. Soc. **123**, 722 (2001).

[160] T. Pino, Ph. Bréchignac, E. Dartois, K. Demyk, L. d'Hendecourt, Chem. Phys. Lett. **339**, 64 (2001).

[161] P. Bréchignac, T. Pino, N. Boudin, Spectrochim. Acta. Part A **57**, 745 (2001)

[162] J. Szczepanski, J. Banisaukas, M. Vala, S. Hirata, R. J. Bartlett, M. Head-Gordon, J. Phys. Chem. A **106**, 63 (2002).

[163] J. Banisaukas, J. Szczepanski, J. eyler, M. Vala, S. Hirata, M. Head-Gordon, J. Oomens, G. Meijer, G. von Helden, J. Phys. Chem. A **107**, 782 (2003).

List of Publications

1. **V. Sivaranjana Reddy**, T. S. Venkatesan, and S. Mahapatra, *"Vibronic interactions in the photodetachment spectroscopy of phenide anion"*,
J. Chem. Phys. **126**, 074306 (2007).

2. **V. Sivaranjana Reddy** and S. Mahapatra, *"Photostability of electronically excited polyacenes: a case study of vibronic coupling in the naphthalene radical cation "*,
J. Chem. Phys. **128**, 091104 (2008).

3. **V. Sivaranjana Reddy** and S. Mahapatra, *"Electronic nonadiabatic interactions and ultrafast internal conversion in phenylacetylene radical cation "*,
J. Chem. Phys. **129**, 124303 (2009).

4. **V. Sivaranjana Reddy** and S. Mahapatra, *"On the vibronic interactions in radical and radical cations of aromatic hydrocarbons "*, in: The Jahn-Teller Effect: Advances and Perspectives, Eds. H. Köppel, H. Barentzen and D. R. Yarkony, Springer Verlag GmBH, Heidelberg (2010), Vol. 97, p. no. 277.

5. **V. Sivaranjana Reddy**, S. Ghanta and S. Mahapatra, *"First principles quantum dynamical investigation provides evidence for the role of polycyclic aromatic hydrocarbon radical cations in interstellar space "*,
Phys. Rev. Lett. **104**, 111102(1-4) (2010).

6. R. R. Kumar,**V. Sivaranjana Reddy** and S. Mahapatra, *"(B + E⊗b)⊗e Jahn-Teller and pseudo-Jahn-Teller effects in spiropentane radical cation "*,
(Communicated to Chem. Phys).

7. **V. Sivaranjana Reddy** and S. Mahapatra, *"Strong nonadiabatic interactions in the low-lying electronic states of dibornae radical cation "*,

(Manuscript under preparation).

8. S. Ghanta, **V. Sivaranjana Reddy** and S. Mahapatra, *"Role of vibronic interactions in the photophysics of naphthalene and anthracene radical cations "*,

(Manuscript under preparation).

Posters/Paper/Oral Presentations in Symposia

1. Poster presented in "Spectroscopy and Dynamics of Molecules and Clusters (SDMC 2006) ",
   March 31 - April 1, 2006, International Centre, Goa.

2. Poster presented in "Theoretical Chemistry Symposium (TCS 2006)",
   December 11-13, 2006, Bharathidasan University, Thiruchirappalli.

3. Poster presented in "Asian Spectroscopy Conference (ASC 2007)",
   January 29 - February 2, 2007, Indian Institute of Science, Bangalore.

4. Poster presented in "Chemfest 2007",
   March 17, 2007, School of Chemistry, University of Hyderabad, Hyderabad.

5. Poster presented in "Spectroscopy and Dynamics of Molecules and Clusters (SDMC 2008)",
   February 22-24, 2008, Mahabalipuram. Tamil Nadu.

6. Poster presented in "Chemfest 2008",
   March 1-2, 2008, School of Chemistry, University of Hyderabad, Hyderabad.

7. Poster presented in "XIX Symposium on the Jahn-Teller Effects 2008",
   August 25-29, 2008, University of Heidelberg, Heidelberg.

8. Poster presented in "Chemfest 2009",
   March 7-8, 2009, School of Chemistry, University of Hyderabad, Hyderabad.

9. Oral presentation in "Chemfest 2009", School of Chemistry,
   University of Hyderabad, Hyderabad, March 7-8, 2009.

10. Poster presented in "Spectroscopy and Dynamics of Molecules and Clusters (SDMC 2010) ",
    February 18 - February 21, 2010, International Centre, Goa.